

Flexible Microimplants

for *In Vivo* Sensing

Thesis by

Yu Zhao

In Partial Fulfillment of the Requirements

for the Degree of

Doctor of Philosophy



California Institute of Technology

Pasadena, California

2014

(Defended on June 3, 2014)

© 2014

Yu Zhao

All Rights Reserved

Acknowledgements

To my advisor, Professor Tai: thank you for going through so many difficulties together with me in the past six years. It has not been an easy task. When I stepped onto this path of self-exploration, I hardly understood the academic, emotional and physical difficulties of doing long-term qualitative research over a prolonged period. You have tried every possible way you could think of to push me, lead me, guide me and inspire me. You have helped me to identify my research interest in microimplants. You have guided me to accumulate the building blocks for future research. You have shown me what it takes to become a top researcher. Twenty years ago, you graduated your first PhD student. Twenty years later, I am so honored to become your 42nd PhD student. In another twenty years, I will cordially invite you to celebrate my reaching of new heights.

To Dr. Hsiai (UCLA): You inspired the direction of this research. Your incisive intellect and clear-minded approach helped me at critical moments to think about this project in novel ways. I am extremely grateful for those many emails we exchanged discussing the logic flow of a paper manuscript, the drawing up of a proposal and a potential collaboration we might explore. I have learned from your unique perspective, the importance of logical progression and patterns in science. I am sure my future academic career will benefit a lot from those trainings.

To wonderful Dr. Fei Yu (USC) and Dr. Hung Cao (UCLA): I feel so lucky to work with you two in the past three and half years. The research we have been doing takes a lot of interdisciplinary effort. You have always been ready for testing whenever my devices got prepared, late night or holiday weekend. You have always been there for

II

me and gave a lot of suggestions whenever device didn't work well. You have always tried to take more responsibilities no matter preparing an experiment, a proposal or a paper manuscript. You have definitely exceeded my best expectation of collaborators. Thank you.

To amazing Mandheerej (Monty) Nandra, thank you for being a mentor and a friend. You are knowledgeable, friendly and helpful. I believe whoever talk to you will instantly love you and never forget you. You are one of the smartest people I know, the one I could always count on for advices and opinions on research-related issues. The little talks about life, the delicious in-n-out burgers, the secrets we shared, the Valentine's Day we celebrated, they all become my most beautiful memory.

I want to thank Prof. Mark Humayun (USC), Prof. James Weiland (USC), Prof. Wentai Liu (UCLA), Prof. Fangang Zeng (UCI), Dr. Bin Xia (Nurotron Biotechnology), Dr. Yang Fang (Advanced Bionics), Prof. Guoxing Wang (SJTU), Prof. Yao Chen (SJTU), Prof. Eberhart Zrenner (University of Tübingen), Prof. Wilfried Mokwa (University Aachen) for providing insightful discussions about my research projects and my career plan.

I want to thank my former college research advisor (PKU), Prof. Wei Wang. You have been providing advices many times during my graduate school career. I still think fondly of my time as an undergraduate student in your lab. You are the reason why I decided to go to pursue a career in MEMS research. Your enthusiasm and love for students is contagious.

III

I will forever be thankful to Prof. Zhihong Li (PKU). Thank you for the tremendous support and trust in the past many years. I have benefited greatly from our many conversations in person and over phone.

I would also like to say thanks to all previous and current group members in Caltech Micromachining Group, Dr. Wen Li, Dr. Siyang Zheng, Dr. Mike Liu, Dr. Quoc (Brandon) Quach, Dr. Ray Huang, Dr. Luca Giacchino, Dr. Jeffrey Lin, Dr. Bo Lu, Dr. Charles DeBoer, Dr. Wendian Shi, Dr. Justin Kim, Dr. Jay Chang, Dr. Jungwook (Jun) Park, Mandheerej (Monty) Nandra, Dongyang (Clark) Kang, Yang Liu, Nick Scianmarello, Xiaoxiao (Shell) Zhang, Aubrey Shapero and Jeff Han, for their assistance, encouragement, and tolerance.

Special thanks go to our lab technician Trevor Roper for his endless maintenance of all kinds of facilities in the group, and our lab administrator Christine Garske for her tremendous help in managing group's purchasing orders.

To my friends (too many to list here, but you know who you are): your unconditional trust and support are among the most precious things I have. You always bring out the best in me. The time we shared together has always been something that important for me, as no one can ever buy nor take back.

To my mother and father: thank you for almost three decades of love, support, inspiration, and encouragement. Your love, wisdom, and generosity have enriched my life and opened my heart in ways I would never have dreamed possible. I love you so much, and I would not have made it this far without you.

Abstract

Flexible Microimplants for In Vivo Sensing

Thesis by

Yu Zhao

Doctor of Philosophy in Electrical Engineering

California Institute of Technology

The work in this thesis develops two types of microimplants for the application of cardiovascular *in vivo* biomedical sensing, one for short-term diagnosis and the other for long-term monitoring.

Despite advances in diagnosis and therapy, atherosclerotic cardiovascular disease remains the leading cause of morbidity and mortality in the Western world. Predicting metabolically active atherosclerotic plaques has remained an unmet clinical need. A stretchable impedance sensor manifested as a pair of quasi-concentric microelectrodes was developed to detect unstable intravascular. By integrating the impedance sensor with a cardiac catheter, high-resolution Electrochemical Impedance Spectroscopy (EIS) measurements can be conducted during cardiac catheterization. An inflatable silicone balloon is added to the sensor to secure a well-controlled contact with the plaque under test *in vivo*. By deploying the device to the explants of NZW rabbit aorta and live animals, distinct EIS measurements were observed for unstable atherosclerotic plaques that harbored active lipids and inflammatory cells.

On the other hand, zebrafish (*Danio rerio*) is an emerging genetic model for heart regenerative medicine. In humans, myocardial infarction results in the irreversible loss of cardiomyocytes. Zebrafish hearts can fully regenerate after two months with 20% ventricular resection. Long-term electrocardiogram (ECG) recording during heart regeneration can characterize whether the structurally regenerated cardiomyocytes can display functionally normal conduction phenotype. A flexible microelectrode membrane was developed to be percutaneously implanted onto a zebrafish heart and record epicardial ECG signals from specific regions on it. Region-specific aberrant cardiac signals were obtained from injured and regenerated hearts. Following that, in order to achieve continuous and wireless recording from non-sedated and non-restricted small animal models, a wireless ECG recording system was designed for the microelectrode membrane, prototyped on a printed circuit board and demonstrated on a one-day-old neonatal mouse. Furthermore, a flexible and compact parylene C printed circuit membrane was used as the integration platform for the wireless ECG recording electronics. A substantially miniature wireless ECG recording system was achieved.

TABLE OF CONTENTS

LIST OF FIGURES	X
LIST OF TABLES	XV
Chapter 1 : Introduction	1
1.1 <i>In Vivo</i> Sensing.....	1
1.1.1 Significance of <i>In Vivo</i> Sensing.....	1
1.1.2 Challenges of <i>In Vivo</i> Sensing	2
1.1.3 Short-Term <i>In Vivo</i> Sensing.....	3
1.1.4 Long-Term <i>In Vivo</i> Sensing.....	5
1.2 Microimplants for <i>In Vivo</i> Sensing	6
1.2.1 Introduction to Microimplants	6
1.2.2 Hardware Implementation of Microimplants.....	7
1.2.3 Challenges of Microimplant Development.....	7
1.3 Parylene-based Flexible BioMEMS	10
1.3.1 Introduction to BioMEMS	10
1.3.2 Introduction to Parylene-based Flexible Technologies.....	11
1.3.3 Introduction to Parylene-Based Flexible Microimplants.....	13
1.4 Goal and Layout of the Dissertation.....	16

1.5 References	18
Chapter 2 Stretchable Balloon-Inflatable Impedance Sensor for Intravascular Plaque Detection	26
2.1 Introduction	27
2.1.1 Significance of Intravascular Plaque Detection.....	27
2.1.2 Current Technologies for Intravascular Plaque Detection.....	29
2.1.3 Introduction to Electrochemical Impedance Spectroscopy (EIS).....	30
2.1.4 Feasibility of Applying EIS to Intravascular Plaque Detection.....	31
2.1.5 Challenges of Implementing EIS in Intravascular Plaque Detection.....	32
2.2 Catheter-based Balloon-Inflatable Quasi-Concentric EIS Microelectrode Sensor	33
2.2.1 Design	33
2.2.2 Fabrication	35
2.2.3 Characterization	38
2.3 Experiments and Results	41
2.3.1 Sample Preparation	41
2.3.2 <i>Ex Vivo</i> EIS Measurements in Fat-Fed NZW Rabbits.....	42
2.3.3 <i>In Vivo</i> EIS Measurements in NZW Rabbit.....	44
2.4 Discussion	45
2.5 Conclusion.....	48

2.6 References	49
Chapter 3 Flexible Microelectrode Membrane for Epicardial ECG Recording.....	53
3.1 Introduction	54
3.1.1 Significance of ECG Recording in Heart Regeneration	54
3.1.2 Introduction to ECG Recording System	57
3.1.3 Overview of Current ECG Recording Systems	59
3.1.4 Challenges of Implementing ECG Recording System in Zebrafish for Heart Regeneration Monitoring	60
3.2 Wearable Microelectrode Membrane	62
3.2.1 Design	62
3.2.2 Fabrication	64
3.2.3 Characterization	66
3.2.4 ECG Recording from Zebra Fish.....	67
3.2.5 Results and Discussion	72
3.2.6 Conclusion	76
3.3 Wireless ECG Recording Backpack	78
3.3.1 Design	79
3.3.2 Implementation and Characterization	81
3.3.3 ECG Recording from Neonatal Mouse.....	87

3.3.4 Results and Discussion	88
3.3.5 Conclusion	90
3.4 Flexible ECG Printed Circuit Membrane.....	90
3.4.1 Design	91
3.4.2 Fabrication and Characterization	103
3.4.3 Discussion and Conclusion.....	108
3.5 Conclusion.....	109
3.6 References	110
Chapter 4 Conclusion	113
References	115

LIST OF FIGURES

Figure 1.1. An illustration of cardiac catheterization.	3
Figure 1.2. Ultra-miniature pressure sensor on catheter tip from Millar's Mikro-Tip ^R	5
Figure 1.3. Inductive coupling circuit schematic circuit.....	9
Figure 1.4. Modified stud ball technique used in "MicroFlex".	10
Figure 1.5. Parylene-based high-density microelectrode array.	14
Figure 1.6. Parylene-based interconnecting substrate with integrated circuit bare die.....	15
Figure 1.7. Parylene-based flexible MEMS coil for intraocular power transfer. .	16
Figure 2.1. Development of atherosclerosis by oxLDL filtration.....	28
Figure 2.2. Comparison of stable and unstable plaques.....	29
Figure 2.3. Simplified equivalent circuit model for impedance measurement in tissue.	31
Figure 2.4. Quasi-concentric microelectrode sensor design.	35
Figure 2.5. Fabrication process of the catheter-based balloon-inflatable microelectrode sensor.	36
Figure 2.6. (a) The impedance sensor was mounted on a balloon. (b) SEM photo of the finished impedance sensor, highlighting the stretchable sinusoidal cables in response to balloon inflation and the two gluing pads allowed for affixation on the surface of the balloon.....	38

Figure 2.7. Inflation pressure characterization <i>in vitro</i> (a) The balloon-inflatable impedance sensor was inserted into the <i>ex-vivo</i> rabbit aorta. (b) Demonstration of balloon inflation prior to impedance assessment. (c) Demonstration of intravascular balloon inflation.....	40
Figure 2.8. Characterization of balloon-inflatable impedance sensor in terms of frequency-dependent changes in impedance magnitude and phase.....	40
Figure 2.9. <i>Ex-vivo</i> EIS acquisition from explanted rabbit aorta and corresponding histology of the aorta wall.....	43
Figure 2.10. Deployment of balloon-inflatable EIS sensors via fluoroscopy guidance in NZW rabbits. The position of EIS sensor was visualized in the carotid artery.	44
Figure 2.11. <i>In-vivo</i> EIS acquisition in the rabbit carotid arteries.....	45
Figure 2.12. Equivalent circuit of the <i>in vivo</i> impedance sensing configuration..	47
Figure 3.1 Heart regeneration in zebrafish model.	55
Figure 3.2. A typical ECG waveform and the characteristics: the P wave, the QRS complex and the T wave.	56
Figure 3.3 Hardware implementation of typical ECG Recording Systems	59
Figure 3.4 Current ECG recording systems: wired, wearable and implantable....	60
Figure 3.5. Device design.	63
Figure 3.6. Fabrication process of the microelectrode membrane.....	65
Figure 3.7. Microelectrode membrane after annealing and assembling.	66
Figure 3.8. Microelectrode model and magnitude of electrode impedances with different dimensions.....	67

XII

Figure 3.9. Zebrafish with microelectrode membrane percutaneously implanted through an open-chest incision. The parylene C-based jacket was wrapped around the zebrafish and placed behind the pectoral fins.	68
Figure 3.10. Recording setup inside a faraday cage.	69
Figure 3.11. Simplified equivalent recording circuit when recording from electrode A and the ground electrode.	70
Figure 3.12 Data processing of recorded ECG signals.	71
Figure 3.13. Zebrafish ECG signals acquired via an implanted MEA membrane over 3 days.	73
Figure 3.14. ST depression in response to cryo-injury.	75
Figure 3.15. Simultaneous four-channel ECG recordings.	78
Figure 3.16. Block diagram of the wireless ECG system.	81
Figure 3.17. Fabricated device. (a) The manufactured microelectrode membrane with meshed parylene-C pad and meandrous strips. (b) The Scanning Electron Microscope (SEM) photo with four gold microelectrodes and the meshed parylene-C pad.	83
Figure 3.18. Circuit schematic of amplification, filtering and data transmission.	84
Figure 3.19. Frequency response of the wireless ECG system.	84
Figure 3.20. Inductive power transfer with hand-wound primary coil and secondary coil.	85
Figure 3.21. Overall power transfer efficiency of inductive coupling link.	86
Figure 3.22. Wireless ECG recording system including the insertable microelectrode membrane and printed circuit board prototype.	86

XIII

Figure 3.23. Wireless ECG recording from neonatal mouse. (a) The experiment setup of the wireless ECG recording. The neonatal mouse was positioned on the baseplate in enclosed by the transmitting coil. (b) The mouse with device on a baseplate (c) after insertion into the transmitter coil.	88
Figure 3.24. (a) A comparison of ECG signals between the sedated and non-sedated conditions. Heart rates are ~300 rpm and ~600 rpm for the sedated and non-sedated mice, respectively. (b) A representative signal-processed ECG tracing revealing the P wave, QRS complex and T wave.....	89
Figure 3.25. Off-the-shelf wirewound unshielded coil for general use in inductive coupling.....	92
Figure 3.26. Circuit routing with all the necessary interconnections and pads. ...	93
Figure 3.27. Printed circuit membrane design with debugging routings and tear-off debugging pads highlighted in red.	94
Figure 3.28. Schematic diagram of the print circuit membrane with all the components assembled.....	95
Figure 3.29. Comparison of one-piece circuit and three pieces of sub-circuits....	96
Figure 3.30. Design of three-level debugging pads, the connecting pads and the alignment assisting pads.	96
Figure 3.31. Cross-sectional view of the bare die assemble.	98
Figure 3.32. 3D drawing of the assembled bare die and discrete resistor.	98
Figure 3.33. Printed circuit membranes of three sub-circuits.	99
Figure 3.34. Three sub-circuits with discrete components assembled.....	99
Figure 3.35. Sub-circuit A and sub-circuit B with bare dies assembled.....	100

XIV

Figure 3.36. Sub-circuit A and sub-circuit B before and after removing primary debugging pads.	100
Figure 3.37. Sub-circuit A+B before and after secondary debugging pads are removed.....	101
Figure 3.38. Sub-circuit C with all the discrete components assembled.	102
Figure 3.39. Final look of the complete wireless ECG system with sensing electrodes and all the electronic modules.	102
Figure 3.40. Microfabrication and assembly flow of the three sub-circuits.	103
Figure 3.41. Assembled sub-circuit C and the power transfer efficiency testing.	104
Figure 3.42. Sub-circuit A and sub-circuit B connected to debugging printed circuit boards with primary debugging pads.....	105
Figure 3.43. Sub-circuit A and sub-circuit B connected through bread board for testing.....	105
Figure 3.44. Assembled sub-circuit A+B.	106
Figure 3.45. Testing platform of the wireless ECG recording system prototyped on parylene printed circuit membrane.	107
Figure 3.46. Recorded ECG signals from simulator on bench top	107
Figure 3.47. Comparison of the ECG wireless recording system prototyped on printed circuit board and on printed circuit membrane.....	108
Figure 3.48. Loading area of zebrafish.	109

LIST OF TABLES

Table 3.1 Signal strength distribution of a representative ECG across each frequency segment.	70
Table 3.2. Component list with length, width, height and weight.	92

Chapter 1 : Introduction

Bian Que was the most recognized physician in ancient China. He was once asked by a King, “The three brothers in your family are all skilled in medicine. Which one of you is the best? Bian Que modestly told the King that his eldest brother was the best, then his second brother, and he was the third. He further explained: My eldest brother gives medical treatment to patients before the onset of a disease. The patients would not even realize they were sick. So it is difficult for them to recognize his medical skills. Only my family members are able to appreciate him. As for my second brother, he treats a disease at its early stage when the symptoms are not very obvious. Thus, people tend to believe he is only capable of treating minor sickness. As for me, I treat a disease when it is already well developed. People are seriously ill. They watch me inject needles, let blood, apply poison drugs on wounds, do surgery... These things help patients by relieving pain and illness and make me well-known all over the country.

The wisdom behind this story is the significance of long-term monitoring, early detection and accurate diagnosis, which can be essentially achieved by *in vivo* sensing in the practice of modern medicine.

1.1 *In Vivo* Sensing

1.1.1 Significance of *In Vivo* Sensing

In vivo sensing can be referred to specifically as detecting and quantifying medically useful variables to assess body function [1]. *In vivo* sensors are developed to directly interrogate biological processes in living organisms. In contrast, *in vitro* sensors

are not able to continuously monitor biological events *in situ* and often fail to capture the complexity of intact organ systems [2]. Driven by the advancements of both biology and technologies, emerging *in vivo* sensors have begun to be applied in living systems to dynamically and continuously monitor biological processes. These *in vivo* sensors have great potentials in continuous, rapid monitoring of biological systems in the context of diseases, informing response to therapies, accelerating detection of diseases, and understanding of normal biology [3].

1.1.2 Challenges of *In Vivo* Sensing

The challenges of *in vivo* sensing lie in both the inaccessibility of *in vivo* tissues and fundamental difficulties in sensor design and application [2]. Normally, an *in vivo* sensor is simply composed of a detector (such as an electrode, antibody, aptamer, peptide or enzyme) paired with a detection method (which may be electrochemical, optical or magnetic, among others) [4-7]. Accordingly, sensing *in vivo* requires both the detector and detection method biocompatible, nontoxic, not perturbing the system being examined, capable of monitoring signals within a living system with necessary sensitivity and specificity [1, 3, 4].

The time scale of *in vivo* sensing could vary from hours or days to years, thus imposing different challenges and constraints on the hardware implementation [8, 9]. In this dissertation, *in vivo* sensing is generally classified into short-term *in vivo* sensing and long-term *in vivo* sensing. In both scenarios, minimal perturbation of normal biology is of utmost importance while developing *in vivo* sensors [2]. This includes minimizing the scar tissue formation and immunogenicity during implantation and around implantation sites.

1.1.3 Short-Term *In Vivo* Sensing

Short-term *in vivo* sensing commonly aims to accurately diagnose a disease in its early stage. It has been found to integrate well with available minimally invasive diagnosis and treatment such as cardiac catheterization [10].

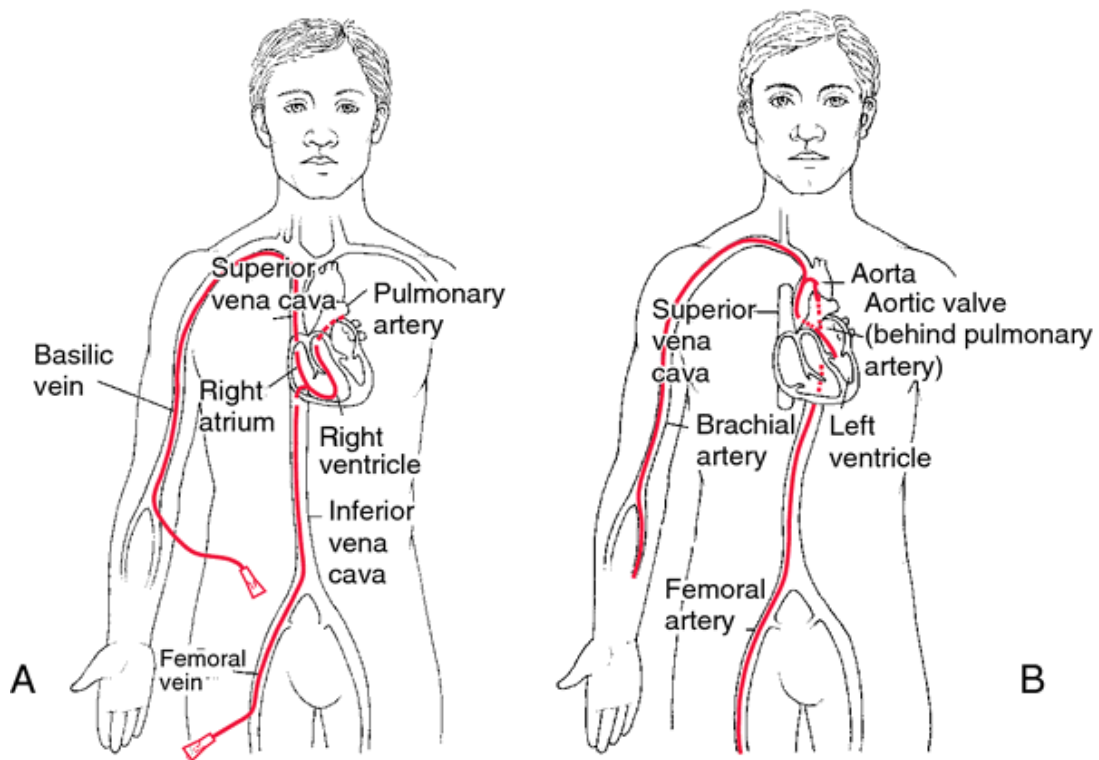


Figure 1.1. An illustration of cardiac catheterization. A: Right-sided heart catheterization. The catheter is inserted into the femoral vein and advanced through the inferior vena cava (or, if into an antecubital or basilic vein, through the superior vena cava), right atrium, right ventricle and into the pulmonary artery. B: Left-sided heart catheterization. The catheter is inserted into the femoral artery or the antecubital artery. The catheter is passed through the ascending aorta, through the aortic valve, and into the left ventricle. (From Ignatavicius and Workman, 2002)

Cardiac catheterization enables doctors to access diseased sites that need to be monitored and treated via the circulatory system [11]. Specialized tubes or catheters are threaded up through the blood vessels in the groin, arm, or neck to an area of the body that needs diagnosis and treatment (Fig. 1.1). The problem is then checked from the inside of the blood vessel. Depending on the blood vessel sizes, the catheters are approximately 0.3-3.0 mm in diameter and 1.5 m in length [11]. The merits of this approach include that catheterization does not require surgical incisions at the monitoring site, hospital stays are usually one night or less, and the discomfort and recovery times afterward are minimal. Therefore, cardiac catheterization is considered a minimally-invasive procedure.

During cardiac catheterization, short-term *in vivo* sensing can gather additional information for diagnosis, monitoring during operation and checking results after procedures [10].

MEMS pressure sensors are now commonly found on cardiac catheter devices [12]. For example, Millar's Mikro-Tip^R ultra-miniature pressure-volume catheters are coupled with an ultra-miniature pressure sensor with an outer diameter of 330 μm to 670 μm (Fig. 1.2). They are capable of measuring both left ventricular pressure and volume simultaneously from the intact, beating hearts of mice and rats. Many other types of MEMS sensors are being researched for placement on diagnostic catheters to measure blood flow, pressure, temperature, oxygen content, and chemical concentration [11, 13-15].

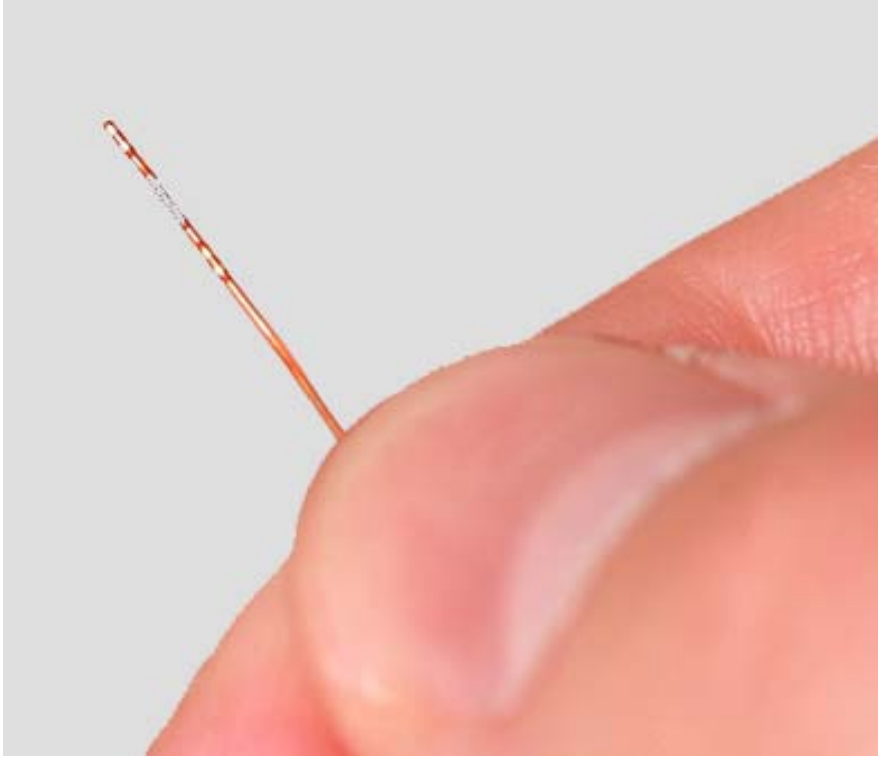


Figure 1.2. Ultra-miniature pressure sensor on catheter tip from Millar's Mikro-Tip^R.

1.1.4 Long-Term *In Vivo* Sensing

Long-term *in vivo* sensing can be a key component of an ideal monitoring system for early detection or a close-loop treatment for uncured disease. Two examples are discussed here.

The first example is the early detection of glaucoma, which highlights the significance of a high-accuracy monitoring system. Glaucoma is the leading cause of blindness in the world, according to the World Health Organization [16]. The majority of glaucoma patients have an intraocular pressure (IOP) larger than 20 mmHg (compared with a normal IOP of ~ 10 mmHg), which could damage the patients' optic nerve in the backside of the eye and causes irreversible blindness. Currently, there is no cure for

glaucoma, but the visual loss can be slowed or eliminated with early diagnosis and proper treatment to lower the high intraocular pressure. Thus, long-term implantable sensors that can continuously monitor intraocular pressure have been widely developed for an early detection and treatment [17, 18].

The second example is the implantable glucose sensor. Currently, the finger-prick sampling method of glucose monitoring is predominantly used in diabetes management. Nevertheless, there has always been a strong push for continuous glucose monitoring, which could form a close-loop control system and make real-time and optimal insulin delivery [19]. With a well-regulated blood glucose level, the short-term crises and long-term complications associated with diabetes could be minimized [9, 19]. A wide range of in-vivo glucose electrochemical sensors, presenting different needle designs, materials and membrane coatings, has been studied in both industry and research [20-22].

1.2 Microimplants for *In Vivo* Sensing

1.2.1 Introduction to Microimplants

The scale of microimplants in this dissertation has two folds. First, devices that are intended to function inside the body for some period (short-term or long-term) and secondly, devices that have at least one part made using integrated circuit-like fabrication technology with micron-sized features.

Microimplants have been found in a myriad of monitoring, diagnostic, therapeutic, and interventional applications. Well-known examples include cardiac pacemakers [23] and defibrillators [24]. There are also emerging applications such as the visual prosthesis

devices [25] and the embedded monitoring devices targeting a variety of physiological variables including oxygen, glucose, pH level, pressure, and temperature [9, 26, 27].

1.2.2 Hardware Implementation of Microimplants

For the application of *in vivo* sensing, the hardware implementation of microimplants usually shares a common set of four function modules including signal sensing, signal processing, data transmission and power transmission [1, 11]. Physiological signals are obtained by front-end sensors, processed and transmitted through a wired or wireless communication scheme to the exterior monitoring/diagnosing unit. Signals need to be transmitted through every medium in between the implant and the external unit. A wireless data transmission could be achieved by modulating different energy forms, such as electromagnetic waves, light and ultrasound [28, 29]. Power can be provided by wired connection, implantable battery, wireless energy transmission or energy harvesting.

1.2.3 Challenges of Microimplant Development

The requirements of microimplants are application specific, but there are several challenges commonly encountered in module implementation. Three of the major challenges as well as the previous research efforts conducted to tackle the challenges are reviewed in this section.

1.2.3.1 Sensor

For *in vivo* sensing, either long-term or short-term, one major challenge is how to make it minimally invasive. The sensor should be of a very tiny size and proper shape that minimizes surgical damage during implantation and reduces discomfort after

implantation. The front-end signal-sensing module forms the interface between the biological tissue and the engineering device. Careful consideration is given to the mechanical properties of the biological tissue, the anatomical structure of the implantation site, the relative mechanical movement between the implant and the surrounding tissue, when selecting implant materials and determining the mechanical design of the implant. For one example, the chemical composition of the implant should not increase or extend the presence of the implant [30]. For another example, sharp edges and corners should be avoided [31]. Furthermore, biocompatible coatings could be important to further minimize the body's immune response. Meanwhile, the surgical procedure performed to implant a device may also cause a series of foreign body reactions. Therefore, the device should have an optimal design to minimize surgical damage during implantation [32].

1.2.3.2 Power

For short-term *in vivo* sensing, it is practical to make wired connections to supply power to the sensor. For long-term *in vivo* sensing, wired powering connections can restrict the movement and increase the chances of infection. Using an implantable battery is an option, but the increased total size of the device limits the choice of implantation sites. Also, battery lifetime is usually limited, and even rechargeable batteries have a limited number of recharging cycles. Energy harvesting could be used in implants, but the amount of power collected from the body is usually too low for practical use.

Inductive coupling through a pair of coils appears to be one of the most promising approaches in wireless power transfer. In this scheme, one coil is placed outside of the implantation site and another one is implanted inside to form a loosely-coupled transformer.

The medium between the coils could include air, water, and biological tissue (Fig. 1.3). To obtain a higher power coupling efficiency, an external capacitor is added to form a tuned-in-series external resonator and a turned-in-parallel implanted resonator with the pair of coils, respectively. When the transmitter coil is driven by the sinusoidal signals at the resonating frequency, it creates a changing electromagnetic field. The implanted coil captures a portion of it and has current produced in the resonator. Considering the tissue absorption rate and power transfer efficiency, the operational frequency, which is the resonating frequency at the same time, should be in the range of 1 and 20 MHz and the power transmitted from the external unit should not exceed 10 mW/cm^2 in compliance with government safety standards.

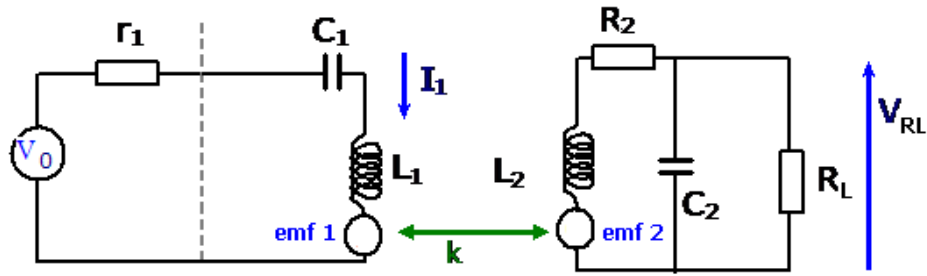


Figure 1.3. Inductive coupling circuit schematic circuit.

1.2.3.3 Integration

To build a complete implantable system that includes the function modules of sensing, processing, data transmission and power transmission, it is of great importance to use a flexible and miniaturized integration with small footprints, high functionality, high reliability and biocompatibility [33].

Application-specific integrated circuits (ASICs) can achieve high integration density of the electronic circuitry including single transmission, power management as well as signal processing. However, the major challenge lies in the hybrid integration of the whole system and how to further minimize it [33]. On the other hand, a flexible substrate is preferred considering the implantable systems could be in direct contact with delicate and soft tissue and biological structures.

For small volume production at the proof of concept stage, flip-chip bonding and a modified stud ball technique (“MicroFlex Technique”) have been developed for integration of standard integrated circuits (ICs) and discrete components onto the flexible interconnecting polyimide substrate [34] (Fig. 1.4).

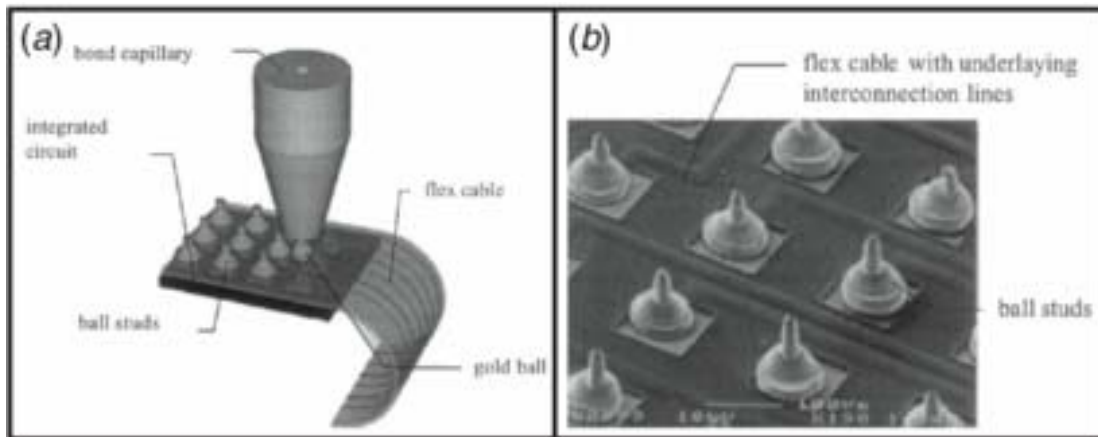


Figure 1.4. Modified stud ball technique used in “MicroFlex”.

1.3 Parylene-based Flexible BioMEMS

1.3.1 Introduction to BioMEMS

Microelectromechanical systems (MEMS) technologies generally refer to the processes of fabrication of miniaturized structures of micrometer scales. They originated

from the microfabrication processes used for integrated circuit fabrication and semiconductor manufacturing, then were later adapted and extended to include some other similar techniques. The major concepts and principles behind MEMS technologies are photolithography, thin films deposition and etching techniques. By repeating the sequences of deposition, photolithography patterning and etching, desired features can be produced in a layer-by-layer fashion.

BioMEMS is a sub-domain of MEMS and its emergency has given rise to a lot of interdisciplinary research in biomedical applications. A lot of bioMEMS devices for *in vitro* diagnostic use have been fabricated and tested in the laboratory stage, such as micro channels, micro valves, micro cantilevers, micro pumps and micro reservoirs [35-37]. There has long been interest in applying bioMEMS technologies for *in vivo* sensing because bioMEMS technologies offer great potential in making devices and components with small and well-controlled features, high reproducibility and uniformity, low weight and cost, superior functionality and performance [38]. In addition, in recent years, bioengineering technology and molecular technology have been combined with bioMEMS technology. Some biocompatible materials have been introduced and widely used in bioMEMS fabrication. Therefore, bioMEMS technologies have provided unique opportunities to make big impacts in the biomedical, surgical and pharmaceutical fields.

1.3.2 Introduction to Parylene-based Flexible Technologies

Parylene is the trade name for a family of semicrystalline thermoplastic polymers known as the poly-para-xylylene (PPX). The polymers were discovered in 1947 by Michael Szwarc in Manchester, England. There are over 20 types of parylene actually developed, but only three have been used on large scales: parylene N (no chlorine on the

benzene ring), parylene C (one chlorine on the benzene ring), and parylene D (with two chlorines on the benzene ring) (Fig. 5).

The advantages of using parylene, and more specially, parylene C for *in vivo* applications include high elongation (up to 200%), low Young's modulus (around 2.8-4 GPa), FDA approval for chronic human implant (USP class VI), conformal pinhole-free vapor deposition, ease of etching in oxygen plasmas, high resistivity, and low permeability against water, gasses and ions [39, 40].

1.3.2.1 Parylene Deposition

Parylene layers are deposited in a vapor deposition polymerization process [40]. As the starting substance, the dimer of a specific parylene type is heated up until it vaporizes and later on splits into a monomeric gas. When the gas reaches the deposition chamber, it cools down to room temperature and polymerizes on the target. The deposition process allows a conformal coating of the target from tall sides and even sharp edges. Typical layer thicknesses range from sub micrometers to tens of micrometers.

1.3.2.2 Parylene Dry Etching

Parylene is inert to most chemical reagents, so oxygen plasma dry etching is usually used to pattern parylene [41]. Photoresist is the most commonly used mask for parylene dry etching. The etching rate ratio between parylene and AZ-series photoresist is 1:1.6 for soft-baked photoresist. To etch thick parylene exceeding 10 μ m, aluminum can be used as an alternative long-lasting mask. Plasma etching and Reactive Ion Etching (RIE) are both used for parylene dry etching. Plasma etching gives an isotropic profile. For fine features or critical side-wall profile, RIE is recommended due to its increased anisotropy.

1.3.2.3 Parylene Adhesion

It is generally believed that parylene deposited on a hydrophobic surface shows good adhesion, and deposition on a hydrophilic surface leads to poor adhesion [42]. Poor adhesion is undesirable during device fabrication, because the parylene interface can be easily delaminated via chemical attack. For example delamination may occur due to hydrolysis if the device is placed in an aqueous environment. One exception is in a process step where the parylene membrane needs to be peeled off from the substrate. Here, the poor adhesion is clearly favored.

Parylene shows poor adhesion on oxidized silicon surfaces due to its surface hydrophilicity. Hexamethyldisiloxane (HMDS) is the most frequently used chemical to reduce the parylene-to-silicon adhesion. This technique is applied when making parylene-based devices that need to be peeled off from the carrier wafer.

There are several methods that can enhance the adhesion between parylene and silicon. Some chemicals, such as A-174 provided by Specialty Coating Systems (SCS), are aimed at enhancing the adhesion by chemical methods. It was also found that parylene shows better adhesion on rougher surfaces. Surface roughness and the anchoring designs both contribute to the enhanced adhesion.

1.3.3 Introduction to Parylene-Based Flexible Microimplants

Due to superior material properties, parylene C has been widely utilized as the structure and insulating materials in different implantable devices. A parylene-based retinal prosthetic device has been under development to treat age-related blindness caused by outer retinal degeneration [43]. It comprises a high-density epiretinal stimulating microelectrode array, radio-frequency coils for power and data telemetry, a

telemetry-recovery and driving ASIC and a flexible interconnecting substrate for integrating all the modules [44].

1.3.3.1 Parylene-Based Flexible Microelectrode Array

Flexible parylene-based microelectrode arrays have been microfabricated with thin-film platinum on parylene substrate (Fig. 1.5). A single-metal-layer process or a dual-metal-layer process could be used to meet the needs of extremely high-density stimulation applications. Some electrodes can survive for more than 430 million pulses without failing. A chronic implantation study of the mechanical effects of parylene-based microelectrode arrays on the retina over a six month follow-up period has shown excellent stability [45].

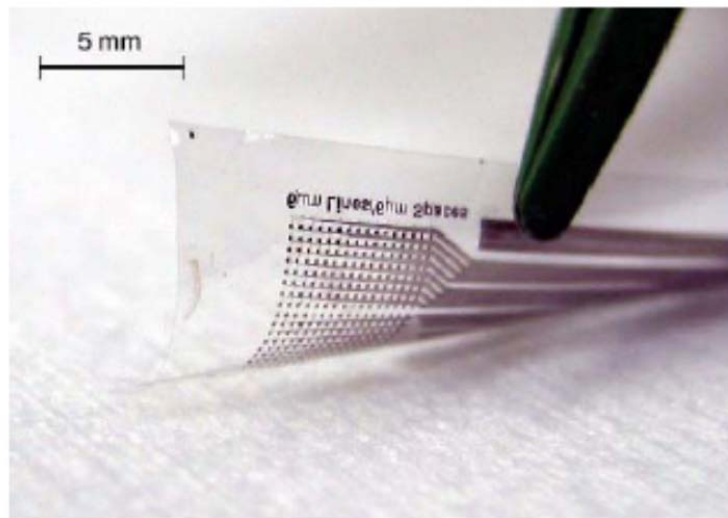


Figure 1.5. Parylene-based high-density microelectrode array.

1.3.3.2 Parylene-Based Flexible Assembly

Flexible parylene-based interconnecting substrate has been monotonically fabricated with the microelectrode array in the same microfabrication process [46] (Fig.

1.6). The substrate has a pocket designed for the ASIC to sit inside. High-lead electrical connections have been made by conductive epoxy through a high-yield “squeeze” technique.

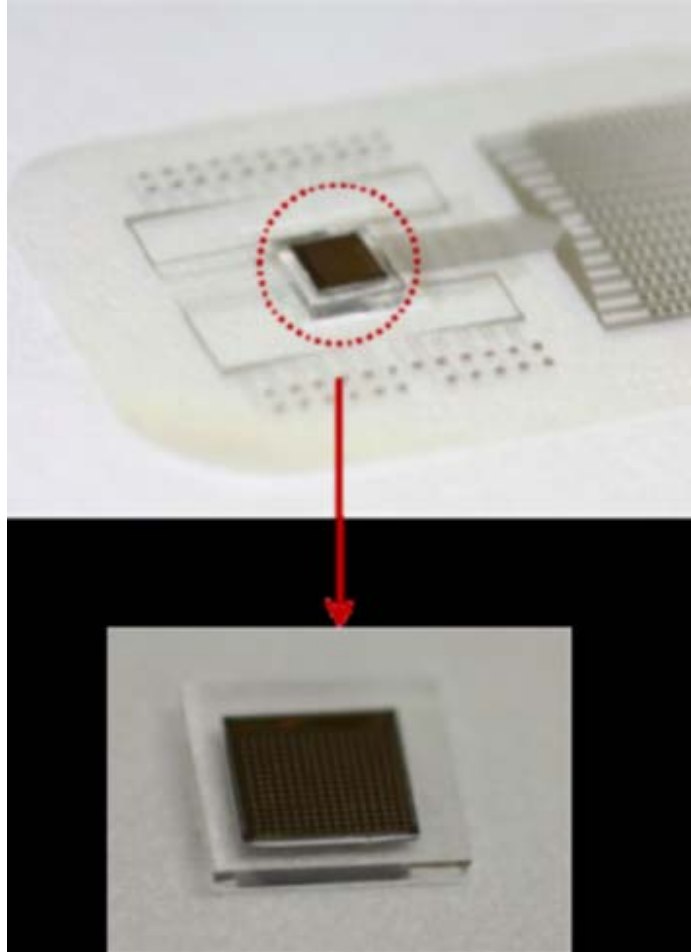


Figure 1.6. Parylene-based interconnecting substrate with integrated circuit bare die.

1.3.3.3 Parylene-Based Flexible Power Coil

Inductive coupling has been chosen as the wireless power transfer scheme for retinal prostheses. Given the power consumption of more than 100 mW needed for high-resolution implant (Fig. 1.7), a power receiver coil with high quality factor is required. Various types of MEMS coils have been designed and fabricated using the parylene-

metal-parylene skin technology. The fold-and-bond technology has been demonstrated to be an effective technique to obtain a high-Q coil. The coil has proven to be mechanically flexible with good electrical performance [47].

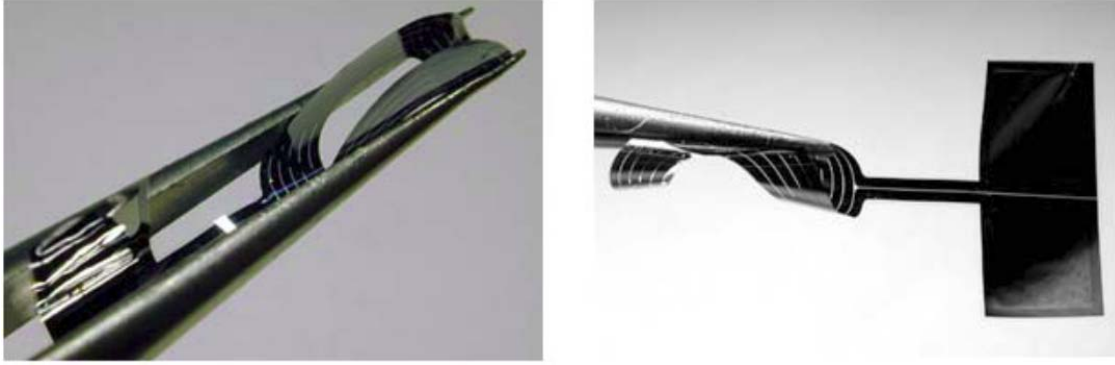


Figure 1.7. Parylene-based flexible MEMS coil for intraocular power transfer.

1.4 Goal and Layout of the Dissertation

The work of this thesis is to develop flexible microimplants for clinical and biological needs in *in vivo* sensing. In **Chapter 1**, the needs of *in vivo* sensing are classified into two types, long-term and short-term. Then, design strategies of microimplants for *in vivo* sensing in terms of hardware implementation are discussed. The hardware function modules and challenges of building these modules are identified and explored in the following chapters.

Chapter 2 reports a stretchable impedance sensor manifested as a pair of quasi-concentric microelectrodes that can be integrated with a cardiac catheter to detect unstable intravascular plaque during cardiac catheterization. It is intended to perform short-term *in vivo* sensing and ideally achieve high-accuracy diagnosis. An inflatable silicone balloon is added to the sensor to secure a well-controlled contact with the plaque *in vivo*. The stretchable impedance sensors were deployed to the explants of NZW rabbit

aorta for detection of lipid-rich atherosclerotic plaques, and to live animals for demonstration of balloon inflation and electrochemical impedance spectroscopy (EIS) measurements. This chapter formed the bulk of the publication in *Biosensors and Bioelectronics* [48].

Chapter 3 develops a flexible sensor membrane for multi-site epicardial ECG monitoring of heart regeneration in zebrafish. To meet the requirements of long-term *in vivo* sensing, the sensor membrane went through a series of design optimizations to enable long-term biocompatibility and reliable functionality. To further achieve continuous monitoring, the wireless operation of the sensor membrane was demonstrated by prototyping signal processing, wireless data transmission and wireless power management modules on a printed circuit board (PCB). The device was tested on neonatal mouse instead of zebrafish because of size and weight limitations. To further reduce the size and weight, a parylene-based printed circuit membrane was designed and fabricated to replace the PCB. The flexible, light-weight and compact parylene printed circuit membrane was monolithically fabricated with sensor electrodes and provided mechanical substrate and electrical interconnection for electronic components. The miniaturized wireless ECG recording implant can be potentially deployed on small animal models and achieve minimally invasive needle injection. The work provided the material for a conference proceeding [49] and two journal papers [50] [51]

Chapter 4 recapitulates the key outcomes of this body of work and how they contribute to the field of *in vivo* biomedical sensing and its hardware implementation. Future research initiatives that extend from the work within this thesis are also briefly discussed.

1.5 References

- [1] G. S. Wilson and R. Gifford, "Biosensors for real-time in vivo measurements," *Biosensors and Bioelectronics*, vol. 20, pp. 2388-2403, 6/15/ 2005.
- [2] M. A. Eckert, P. Q. Vu, K. X. Zhang, D. K. Kang, M. M. Ali, C. J. Xu, *et al.*, "Novel Molecular and Nanosensors for In Vivo Sensing," *Theranostics*, vol. 3, pp. 583-594, 2013.
- [3] M. A. Eckert and W. Zhao, "Opening windows on new biology and disease mechanisms: development of real-time in vivo sensors," *Interface Focus*, vol. 3, June 6, 2013 2013.
- [4] A. Ramesh, F. Ren, P. R. Berger, P. Casal, A. Theiss, S. Gupta, *et al.*, "Towards in vivo biosensors for low-cost protein sensing," *Electronics Letters*, vol. 49, pp. 450-451, Mar 2013.
- [5] M. L. James and S. S. Gambhir, "A MOLECULAR IMAGING PRIMER: MODALITIES, IMAGING AGENTS, AND APPLICATIONS," *Physiological Reviews*, vol. 92, pp. 897-965, Apr 2012.
- [6] K. W. Plaxco and H. T. Soh, "Switch-based biosensors: a new approach towards real-time, in vivo molecular detection," *Trends in Biotechnology*, vol. 29, pp. 1-5, Jan 2011.
- [7] N. J. Ronkainen, H. B. Halsall, and W. R. Heineman, "Electrochemical biosensors," *Chemical Society Reviews*, vol. 39, pp. 1747-1763, 2010.
- [8] M. A. Carvajal, I. M. P. de Vargas-Sansalvador, A. J. Palma, M. D. Fernandez-Ramos, and L. F. Capitan-Vallvey, "Hand-held optical instrument for CO₂ in gas

- phase based on sensing film coating optoelectronic elements," *Sensors and Actuators B-Chemical*, vol. 144, pp. 232-238, Jan 2010.
- [9] S. V. Edelman, D. J. Beatty, M. Bouvet, J. C. Fisher, and W. T. Cefalu, "Continuous glucose sensing with a long-term subcutaneous implant in patients with Type 1 diabetes," *Diabetologia*, vol. 45, pp. A27-A27, Aug 2002.
- [10] C. Tei, R. A. Nishimura, J. B. Seward, and A. J. Tajik, "Noninvasive Doppler-derived myocardial performance index: Correlation with simultaneous measurements of cardiac catheterization measurements," *Journal of the American Society of Echocardiography*, vol. 10, pp. 169-178, Mar 1997.
- [11] Y. Haga and M. Esashi, "Biomedical microsystems for minimally invasive diagnosis and treatment," *Proceedings of the Ieee*, vol. 92, pp. 98-114, Jan 2004.
- [12] J. F. L. Goosen, P. J. French, and P. M. Sarro, "Pressure and flow sensor for use in catheters," in *Micromachined Devices and Components V*. vol. 3876, P. J. French and E. Peeters, Eds., ed Bellingham: Spie-Int Soc Optical Engineering, 1999, pp. 38-45.
- [13] C. Y. Li, P. M. Wu, J. A. Hartings, Z. Z. Wu, C. H. Ahn, D. LeDoux, *et al.*, "Smart catheter flow sensor for real-time continuous regional cerebral blood flow monitoring," *Applied Physics Letters*, vol. 99, p. 4, Dec 2011.
- [14] K. Tsukada, S. Sakai, K. Hase, and H. Minamitani, "Development of catheter-type optical oxygen sensor and applications to bioinstrumentation," *Biosensors & Bioelectronics*, vol. 18, pp. 1439-1445, Oct 2003.
- [15] C. Y. Li, P. M. Wu, Z. Z. Wu, C. H. Ahn, D. LeDoux, L. A. Shutter, *et al.*, "Brain temperature measurement: A study of in vitro accuracy and stability of smart

- catheter temperature sensors," *Biomedical Microdevices*, vol. 14, pp. 109-118, Feb 2012.
- [16] K. Gungor, P. J. Hotez, V. Ozdemir, and S. Aynacioglu, "Glaucomics: A Call for Systems Diagnostics for 21(st) Century Ophthalmology and Personalized Visual Health," *Omics : a journal of integrative biology*, vol. 18, pp. 275-9, 2014 May (Epub 2014 Apr 2014).
- [17] N. Xue, S. P. Chang, and J. B. Lee, "A SU-8-Based Microfabricated Implantable Inductively Coupled Passive RF Wireless Intraocular Pressure Sensor," *Journal of Microelectromechanical Systems*, vol. 21, pp. 1338-1346, Dec 2012.
- [18] F. Piffaretti, D. Barrettino, P. Orsatti, L. Leoni, and P. Stegmaier, "Rollable and implantable intraocular pressure sensor for the continuous adaptive management of glaucoma," *Conference proceedings : ... Annual International Conference of the IEEE Engineering in Medicine and Biology Society. IEEE Engineering in Medicine and Biology Society. Conference*, vol. 2013, pp. 3198-201, 2013 2013.
- [19] D. C. Klonoff, "Continuous glucose monitoring - Roadmap for 21st century diabetes therapy," *Diabetes Care*, vol. 28, pp. 1231-1239, May 2005.
- [20] S. Q. Gu, Y. L. Lu, Y. P. Ding, L. Li, H. S. Song, J. H. Wang, *et al.*, "A droplet-based microfluidic electrochemical sensor using platinum-black microelectrode and its application in high sensitive glucose sensing," *Biosensors & Bioelectronics*, vol. 55, pp. 106-112, May 2014.
- [21] Y. Yoon, G. S. Lee, K. Yoo, and J. B. Lee, "Fabrication of a Microneedle/CNT Hierarchical Micro/Nano Surface Electrochemical Sensor and Its In-Vitro Glucose Sensing Characterization," *Sensors*, vol. 13, pp. 16672-16681, Dec 2013.

- [22] A. Heller and B. Feldman, "Electrochemical glucose sensors and their applications in diabetes management," *Chemical Reviews*, vol. 108, pp. 2482-2505, Jul 2008.
- [23] D. DiFrancesco, "PACEMAKER MECHANISMS IN CARDIAC TISSUE," *Annual Review of Physiology*, vol. 55, pp. 455-472, 1993.
- [24] M. Mirowski, "THE AUTOMATIC IMPLANTABLE CARDIOVERTER-DEFIBRILLATOR - AN OVERVIEW," *Journal of the American College of Cardiology*, vol. 6, pp. 461-466, 1985.
- [25] M. S. Humayun, J. D. Weiland, G. Y. Fujii, R. Greenberg, R. Williamson, J. Little, *et al.*, "Visual perception in a blind subject with a chronic microelectronic retinal prosthesis," *Vision Research*, vol. 43, pp. 2573-2581, Nov 2003.
- [26] G. Koley, J. Liu, M. W. Nomani, M. B. Yim, X. J. Wen, and T. Y. Hsia, "Miniaturized implantable pressure and oxygen sensors based on polydimethylsiloxane thin films," *Materials Science & Engineering C-Biomimetic and Supramolecular Systems*, vol. 29, pp. 685-690, Apr 2009.
- [27] A. Khairi, C. Y. Wu, Y. Rabin, G. Fedder, J. Paramesh, D. Schwartzman, *et al.*, "Ultra-Low Power Frequency and Duty-cycle Modulated Implantable Pressure-Temperature Sensor," in *2013 Ieee Biomedical Circuits and Systems Conference*, ed New York: Ieee, 2013, pp. 226-229.
- [28] D. C. Jeutter, "Overview of Biomedical Telemetry Techniques," *Engineering in Medicine and Biology Magazine, IEEE*, vol. 2, pp. 17-24, 1983.

- [29] A. Kiourti and K. S. Nikita, "A Review of Implantable Patch Antennas for Biomedical Telemetry: Challenges and Solutions [Wireless Corner]," *Antennas and Propagation Magazine, IEEE*, vol. 54, pp. 210-228, 2012.
- [30] U. Dapunt, T. Giese, F. Lasitschka, J. Reinders, B. Lehner, J. P. Kretzer, *et al.*, "On the inflammatory response in metal-on-metal implants," *Journal of translational medicine*, vol. 12, p. 74, 2014 2014.
- [31] S. Barkam, S. Saraf, and S. Seal, "Fabricated Micro-Nano Devices for In vivo and In vitro Biomedical Applications," *Wiley Interdisciplinary Reviews-Nanomedicine and Nanobiotechnology*, vol. 5, pp. 544-568, Nov 2013.
- [32] M. W. Ashraf, S. Tayyaba, and N. Afzulpurkar, "Micro Electromechanical Systems (MEMS) Based Microfluidic Devices for Biomedical Applications," *International Journal of Molecular Sciences*, vol. 12, pp. 3648-3704, Jun 2011.
- [33] W. Mokwa, "Medical implants based on microsystems," *Measurement Science & Technology*, vol. 18, pp. R47-R57, May 2007.
- [34] T. Stieglitz, H. Beutel, and J. U. Meyer, ""Microflex" - A new assembling technique for interconnects," *Journal of Intelligent Material Systems and Structures*, vol. 11, pp. 417-425, Jun 2000.
- [35] E. Nuxoll, "BioMEMS in drug delivery," *Advanced Drug Delivery Reviews*, vol. 65, pp. 1611-1625, Nov 2013.
- [36] A. K. Au, H. Y. Lai, B. R. Utela, and A. Folch, "Microvalves and Micropumps for BioMEMS," *Micromachines*, vol. 2, pp. 179-220, Jun 2011.

- [37] A. C. R. Grayson, R. S. Shawgo, A. M. Johnson, N. T. Flynn, Y. W. Li, M. J. Cima, *et al.*, "A BioMEMS review: MEMS technology for physiologically integrated devices," *Proceedings of the Ieee*, vol. 92, pp. 6-21, Jan 2004.
- [38] T. James, M. S. Mannoor, and D. V. Ivanov, "BioMEMS - Advancing the frontiers of medicine," *Sensors*, vol. 8, pp. 6077-6107, Sep 2008.
- [39] J. Noordegraaf, "Conformal coating using parylene polymers," *Medical device technology*, vol. 8, pp. 14-20, 1997 1997.
- [40] G. E. Loeb, M. J. Bak, M. Salcman, and E. M. Schmidt, "PARYLENE AS A CHRONICALLY STABLE, REPRODUCIBLE MICROELECTRODE INSULATOR," *Ieee Transactions on Biomedical Engineering*, vol. 24, pp. 121-128, 1977.
- [41] C. P. Tan and H. G. Craighead, "Surface Engineering and Patterning Using Parylene for Biological Applications," *Materials*, vol. 3, pp. 1803-1832, Mar 2010.
- [42] J. M. Hsu, L. Rieth, S. Kammer, M. Orthner, and F. Solzbacher, "Effect of thermal and deposition processes on surface morphology, crystallinity, and adhesion of Parylene-C," *Sensors and Materials*, vol. 20, pp. 87-102, 2008.
- [43] W. Li, D. C. Rodger, E. Meng, J. D. Weiland, M. S. Humayun, and Y. C. Tai, "Wafer-Level Parylene Packaging With Integrated RF Electronics for Wireless Retinal Prostheses," *Journal of Microelectromechanical Systems*, vol. 19, pp. 735-742, Aug 2010.

- [44] D. C. Rodger, A. J. Fong, W. Li, H. Ameri, I. Lavrov, H. Zhong, *et al.*, *High-density flexible parylene-based multielectrode arrays for retinal and spinal cord stimulation*. New York: Ieee, 2007.
- [45] D. C. Rodger, A. J. Fong, W. Li, H. Ameri, A. K. Ahuja, C. Gutierrez, *et al.*, "Flexible parylene-based multielectrode array technology for high-density neural stimulation and recording," *Sensors and Actuators B: Chemical*, vol. 132, pp. 449-460, 6/16/ 2008.
- [46] J. H. Chang, R. Huang, and T. Yu-Chong, "High density 256-channel chip integration with flexible parylene pocket," in *Solid-State Sensors, Actuators and Microsystems Conference (TRANSDUCERS), 2011 16th International*, 2011, pp. 378-381.
- [47] C. Po-Jui, K. Wen-Cheng, L. Wen, Y. Yao-Joe, and T. Yu-Chong, "Q-enhanced fold-and-bond MEMS inductors," in *Nano/Micro Engineered and Molecular Systems, 2008. NEMS 2008. 3rd IEEE International Conference on*, 2008, pp. 869-872.
- [48] H. Cao, F. Yu, Y. Zhao, N. Scianmarello, J. Lee, W. D. Dai, *et al.*, "Stretchable electrochemical impedance sensors for intravascular detection of lipid-rich lesions in New Zealand White rabbits," *Biosensors & Bioelectronics*, vol. 54, pp. 610-616, Apr 2014.
- [49] Z. Yu, Y. Fei, C. Hung, C. Honglong, Z. Xiaoxiao, T. K. Hsiai, *et al.*, "A wearable percutaneous implant for long term zebrafish epicardial ECG recording," in *Solid-State Sensors, Actuators and Microsystems (TRANSDUCERS*

& *EUROSENSORS XXVII*), *2013 Transducers & Eurosensors XXVII: The 17th International Conference on*, 2013, pp. 756-759.

- [50] F. Yu, Y. Zhao, J. Gu, K. Quigley, N. Chi, Y.-C. Tai, *et al.*, "Flexible microelectrode arrays to interface epicardial electrical signals with intracardial calcium transients in zebrafish hearts," *Biomedical Microdevices*, vol. 14, pp. 357-366, 2012/04/01 2012.
- [51] H. Cao, Y. Zhao, F. Yu, X. Zhang, J. Tai, J. Lee, *et al.*, "Wearable Multi-Channel Microelectrode Membranes to Reveal Injured Cardiac Electrical Signals of Small Vertebral Animals," *Integrative Biology*, vol. Accepted, May 2014.

Chapter 2 Stretchable Balloon-Inflatable Impedance Sensor for Intravascular Plaque Detection

This chapter develops a balloon-inflatable impedance sensor for intravascular plaque detection during cardiac catheterization. The significance of this clinical need for diagnosis is described first. After introducing the sensing strategy of electrochemical impedance spectroscopy (EIS), the feasibility and challenges of implementing this strategy to intravascular plaque detection are discussed respectively (**Section 2.1**). A novel catheter-based EIS sensor manifested as a pair of quasi-concentric microelectrodes was designed, fabricated and characterized (**Section 2.2**). An inflatable balloon design was additionally added to the sensor for a better *in vivo* contact. In the experiment section (**Section 2.3**), the procedures of sample preparation, *ex vivo* measurement and *in vivo* measurement are presented in detail and the experimental results showed the capability of the sensor to distinguish impedance magnitude and phase differences between different types of plaques. Finally, **Section 2.4** summarizes the work and compares with other state-of-the-art technologies.

As one type of short-term *in vivo* sensing, the impedance sensor was initially designed with a cardiac catheterization to be minimally invasive. The sensor features a novel quasi-concentric microelectrode design which achieved an accurate diagnosis of early-stage unstable plaque. Moreover, the inflatable balloon facilitated a well-controlled *in vivo* contact which provides insight to the common challenge for an *in vivo* sensor. On

top of that, the sensor has also presented adequate expandability and stretchability to accommodate balloon inflation.

2.1 Introduction

2.1.1 Significance of Intravascular Plaque Detection

Atherosclerosis (also known as arteriosclerotic vascular disease or ASVD) refers to the thickening of an artery wall as a result of invasion and accumulation of fatty materials [1]. Its development starts with the low-density lipoprotein molecules present in the blood stream which get oxidized by free radicals. Once oxidized, LDL (oxLDL) molecules in contact with artery endothelium can cause damage to endothelial cells and result in increased permeability of the endothelium. Then oxLDL molecules can easily migrate into the artery wall. As a result of the damage caused to the blood vessel, an inflammatory response is triggered. White blood cells enter the artery wall to ingest oxLDL but are not able to process it, and instead they will turn into large foam cells with high lipid content. Foam cells die and rupture, further propagating the inflammatory response. Eventually, fatty substances, cholesterol, waste products, calcium and other substances build up and form a plaque [2]. Fibrous tissue can form a hard cover over the affected area known as the fibrous cap (**Fig. 2.1**).

Atherosclerotic plaques can narrow the artery, reduce the blood flow and increase the blood pressure. But most of the damage is caused when the fibrous cap gets ruptured. The formation of a thrombus will slow or stop the blood flow rapidly, leading to tissue death in approximately 5 minutes. The two most commonly recognized scenarios are

heart attack and stroke which are caused by artery thrombosis to the heart and brain respectively [2].

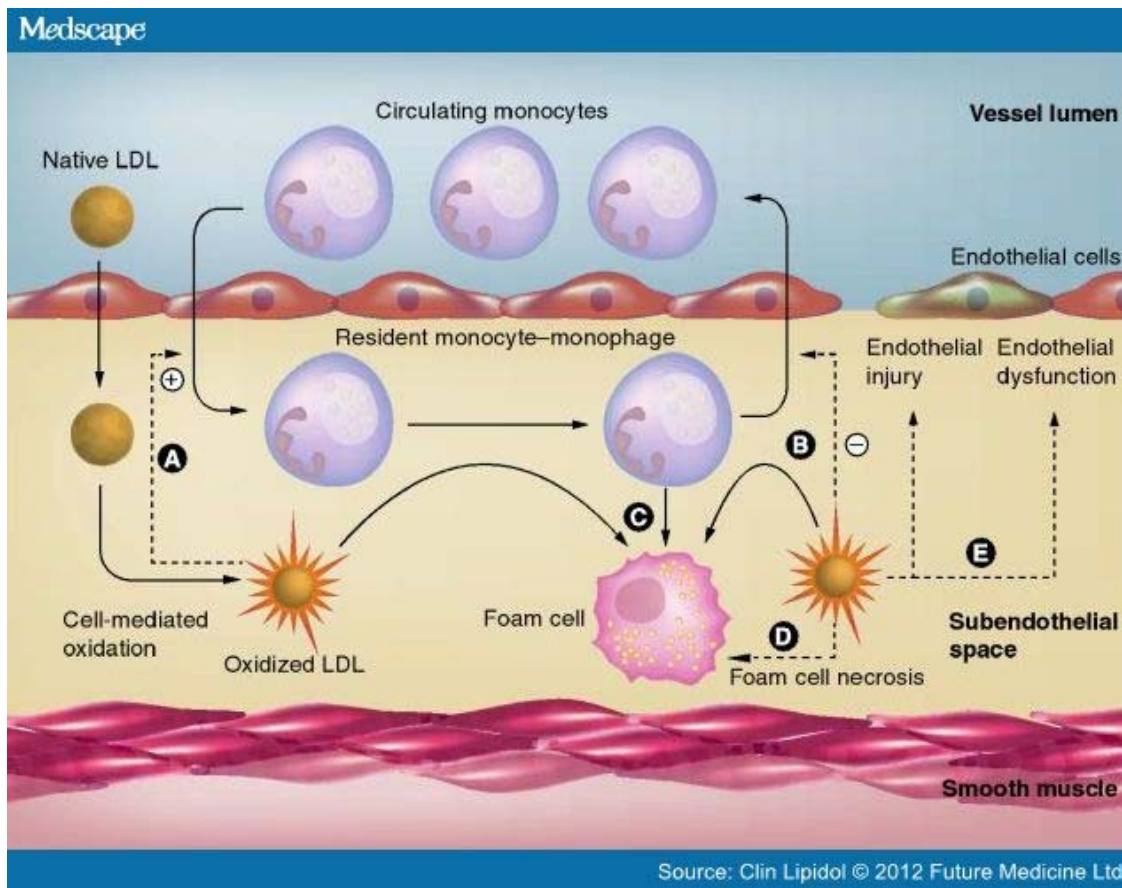


Figure 2.1. Development of atherosclerosis by oxLDL filtration.

Atherosclerotic plaques can be classified into stable and unstable ones (**Fig. 2.2**). There are three main differences: (1) the fibrous cap is thicker in stable plaque and thinner in unstable plaque. (2) The lipid pool underneath the fibrous cap is comparably smaller in stable plaque and larger in unstable plaque. (3) The stable plaques are rich in extracellular matrix and smooth muscle cells, while the unstable plaques are rich in inflammatory cells such as macrophages and oxLDL-filled foam cells. Therefore, the unstable plaque with a thinner fibrous cap over a larger fatty core is more vulnerable. At

the same time, the macrophages within the plaque can release enzymes that break down collagen in the cap, thus the cap gets weaker and more prone to rupture. Therefore, the detection of unstable plaques is of utmost importance and holds the potential to identify patients for selective intervention.

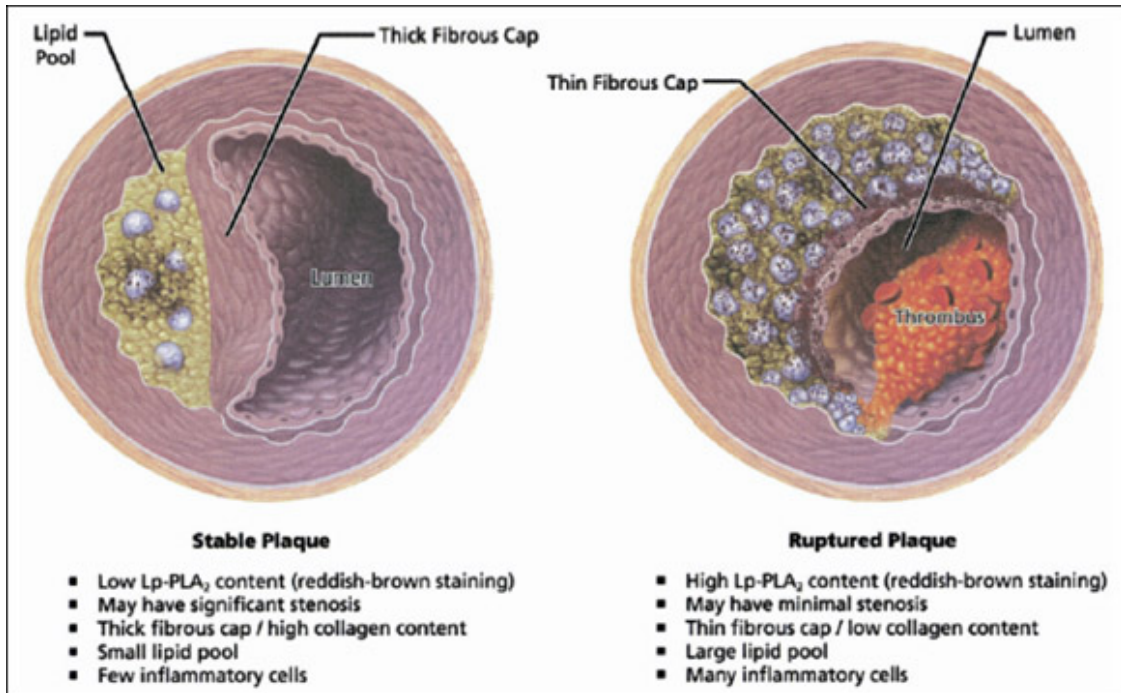


Figure 2.2. Comparison of stable and unstable plaques.

2.1.2 Current Technologies for Intravascular Plaque Detection

Greyscale (GS) intravascular ultrasound (IVUS) has been widely employed as a diagnostic technique for the evaluation of atherosclerotic plaques [3]. However, its specificity and sensitivity for tissue identification are limited. In the last few years, in order to achieve a more reliable analysis of plaque composition, a spectral analysis of IVUS radiofrequency data (RFD) has been developed [4]. Another technique, optical coherence tomography (OCT), is a high-resolution imaging modality that uses reflected

near-infrared light to visualize vascular microstructures and it has been successfully applied for the characterization of coronary atherosclerotic plaques *in vivo* [5]. Intravascular magnetic resonance spectroscopy (IVMR) is a new technique developed to identify specifically the lipid component of plaques based on the self-diffusion of water molecules that is translated into a lipid fraction index (LFI) [6]. These four imaging modalities have in common the ability to give a detailed assessment of the composition of atherosclerotic plaques but do differ in the means of achieving this.

2.1.3 Introduction to Electrochemical Impedance Spectroscopy (EIS)

The impedance Z of a system actually measures the dielectric properties of a medium as a function of frequency [7]. The impedance depends on the interaction between the medium electric dipole and externally applied field. Therefore, it can be determined by applying a sinusoidal voltage perturbation with a small amplitude and detecting the current response. Based on this definition, it can be calculated as:

$$Z = \frac{V(t)}{I(t)} = \frac{V_0 \sin(2\pi f t)}{I_0 \sin(2\pi f t + \phi)}$$

where $V(t)$ is a voltage-time function and $I(t)$ is the responding current-time function, V_0 and I_0 are maximum voltage and current signals, f is the frequency, t is the time, and ϕ is the phase shift.

Z is a complex value representing how the current can differ from voltage in terms of amplitude and phase as well. The complex Z can be expressed by the modulus $|Z|$ and the phase shift ϕ , or alternatively by the real part R and the imaginary part X . Accordingly, the impedance measurement can be illustrated in two different ways, a Bode plot which plots $\log|Z|$ and ϕ as a function of $\log f$, or a Nyquist plot which plots R and X .

The impedance is measured at different frequencies, so called “spectroscopy”. The electrochemical impedance spectroscopy (EIS) is widely used to analyze the complex electrical resistance of a system. It can respond to surface phenomena and bulk properties. For example, as a biosensor, it can detect the binding events on the transducer surface. With the development of instrumentation, EIS has found more applications in characterizing surfaces, layers, membranes, and exchange and diffuse processes in recent years [8].

In order to characterize biological tissue, metallic electrodes must be introduced into the system. By applying a sinusoidal stimulating voltage, the current flows through all the components of a system, including the working electrode, the biological tissue and the counter electrodes. The measured impedance is contributed to by all the individual impedances.

Various equivalent circuit models have been proposed to interpret the impedance spectrum. A simple yet efficient model for the electrochemical impedance in tissue is represented as a parallel capacitance, C_p , shunted by a charge transfer resistance R_p , in series with the tissue resistance R_s (**Fig. 2.3**).

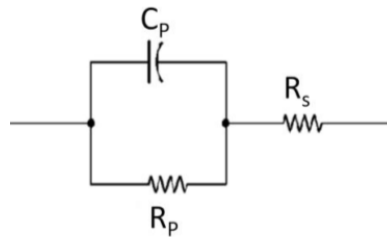


Figure 2.3. Simplified equivalent circuit model for impedance measurement in tissue.

2.1.4 Feasibility of Applying EIS to Intravascular Plaque Detection

Biological tissue such as blood vessels harbor resistance and store charges, exhibiting complex electric impedances as a function of frequency. Atherosclerotic plaques harbor pro-

inflammatory substrates; namely, oxLDL and macrophage-derived foam cells which infiltrate and engender distinct electrochemical properties [9]. Hence, it is feasible to determine the plaques' frequency-dependent electrical and dielectrical behavior by recording the electric impedance of a tissue over a frequency range. Since the electrical properties of biological tissues are related to their physiological and morphological properties, EIS is suitable for the detection of tissue composition and could potentially identify plaques that are prone to rupture.

2.1.5 Challenges of Implementing EIS in Intravascular Plaque Detection

There are several challenges to the implementation of EIS for intravascular plaque detection.

First, for *in vitro* sensing applications, a large surface area provided by the inert platinum or carbon electrode is commonly used as the counter electrode, providing both high charge transfer resistance and double-layer capacitance. The overall impedance contributed by counter electrode is considered negligible. For intravascular EIS applications, where a high spatial resolution is necessary, the confined space in the catheters warrants close packaging of both the counter and working electrodes. For this reason, EIS measurements must account for the electrochemical interference at both the counter and working electrode interfaces.

Secondly, because of the non-homogeneous tissue composition and uneven endoluminal topography, the current distribution generated from applying voltage to the impedance electrodes will be uneven. This is different from *ex vivo* impedance measurement, where the plaques under test and the placement of impedance sensors could be visually adjusted and aligned to compensate. Therefore, a modified electrodes

design and an improved arrangement of the working electrode and counter electrode are needed.

Thirdly, a stable and proper contact of the electrodes with the plaque under test is very important to enhance the qualities of the recorded signal. An external force that can push the electrodes towards the plaque and keep the electrodes in contact is ideal. Considering the plaques tendency to rupture, the applied force needs to be small and gentle. An additional sensor feature was considered here to provide this well-controlled pushing force *in vivo*.

2.2 Catheter-based Balloon-Inflatable Quasi-Concentric EIS Microelectrode Sensor

2.2.1 Design

To facilitate the detection and diagnosis of the non-obstructive and pro-inflammatory atherosclerotic plaque, a pair of quasi-concentric microelectrodes, integrated onto an inflatable silicone balloon, was designed to adhere to a catheter tip to perform the EIS *in vivo* sensing during catheterization.

For the impedance sensing, the central and outer microelectrodes are arranged in a concentric configuration (**Fig. 2.4**). The diameter of the solid central microelectrode is 70 μm and the inner and outer diameters of the annulus outer microelectrode are 100 μm and 300 μm respectively. To achieve this concentric configuration on a single metal layer, a small gap is opened on the outer microelectrode for the routing out of central microelectrode. Although the tiny gap breaks the perfect symmetry of the concentric electrodes, it allows single-layer metal deposition and one-side electrode openings in the fabrication of the device. This can greatly reduce the cost, simplify the process and

increase the yield. More importantly, the central and outer microelectrodes, i.e., the working and counter electrodes, are fabricated monolithically and have exactly same surface properties.

The quasi-concentric microelectrodes are connected to the contact pads through sinusoidal lines for an improved expandability and stretchability during balloon inflation. The contact pads establish electrical connections with the external energy source through medical-grade coaxial wire, and supply the excitation voltage across the central and outer microelectrodes.

There are four major advantages to this design: (1) The quasi-concentric configuration can provide constant and symmetric displacement currents between working and counter electrodes. (2) The quasi-concentric electrodes may allow for EIS measurement independent of the surrounding solutions or blood and the orientation of the tissues. (3) The fabrication process and post connecting process for making the quasi-concentric electrodes are simple and reliable. (4) The small dimensions of the microelectrodes can achieve a higher spatial resolution in the regions of pro-inflammatory states. (5) The small separation between the working and counter electrodes make the measured impedance mainly sensitive to tissue in close proximity and independent of the lumen diameters, blood volumes and flow rates when the *in vivo* contact is made.

An inflatable silicone balloon is designed to inflate *in vivo* and push the electrodes towards the plaque. To integrate the impedance sensor onto the silicone balloon, two meshed anchoring pads with nine through holes on each side are designed to be monolithically fabricated with the sensor. A small amount of additional epoxy applied on

the anchor pads permeates the through holes and bonds together with the silicone balloon body. Because the balloon mainly expands in the radial direction, the sinusoidal cables mostly extend in the longitudinal direction.

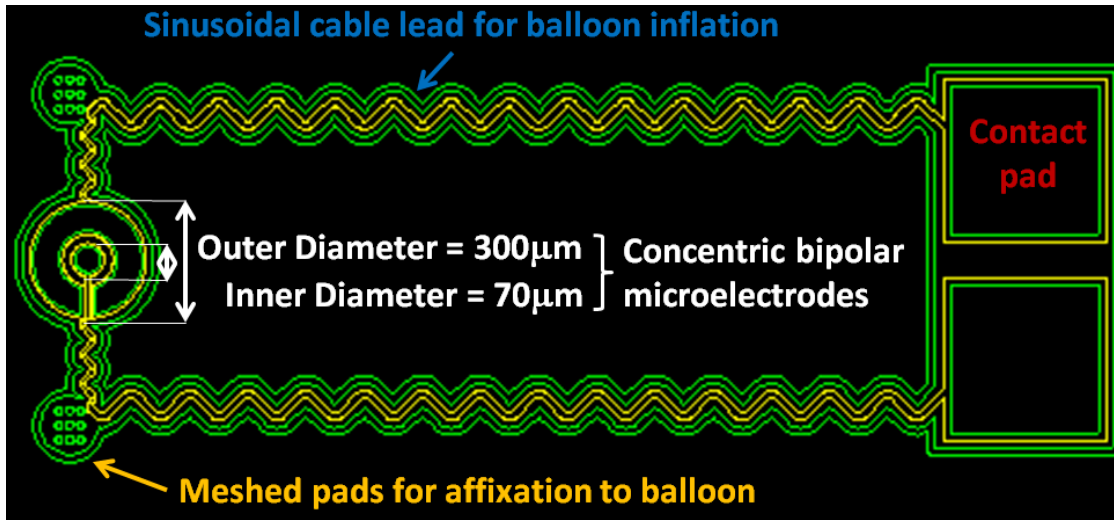


Figure 2.4. Quasi-concentric microelectrode sensor design.

2.2.2 Fabrication

The fabrication process required four main steps: (1) Fabrication of the silicone balloon. (2) Assembly of the sealed tubing connecting the balloon to a syringe. (3) Microfabrication of the impedance sensor. (4) Securing the impedance sensor to the balloon (**Fig. 2.5**).

First, steel tubing with a tip outer diameter (OD) of 0.008 200 μm (McMaster-Carr, Santa Fe Springs, CA) was immersed in AZ9260 photoresist (AZ Electronic Materials, Branchburg, NJ), followed by a baking process for 10 minutes at 100°C. A second coating was then applied and baked for 10 minutes to form the inner layer of the balloon. Nusil 6820 silicone (Nusil Technology LLC, Carpinteria, CA) was used for its low Young's modulus (4.4 MPa) and high elongation (175%). The silicone was

thoroughly mixed in a 1:1 ratio of part A and part B, and then painted onto the surface of PR and the capillary tubing. An opening was intentionally created for the subsequent PR release. Ensuring an even coverage of the balloon is important for symmetrical inflation. The modulus of elasticity increased with increased curing duration and temperature. Afterwards, it was fully submerged into a beaker of acetone to dissolve the PR, thereby forming the cavity and allowing for the removal of the inner steel tube. The hole on the top was further sealed with silicone paint. The balloon was set over a parylene-coated silicon wafer and baked for 10 minutes at 100 °C. Parylene C facilitated peeling of the balloon, and resting of the sensor on a wafer created a planar surface on the balloon for securing the impedance sensor.

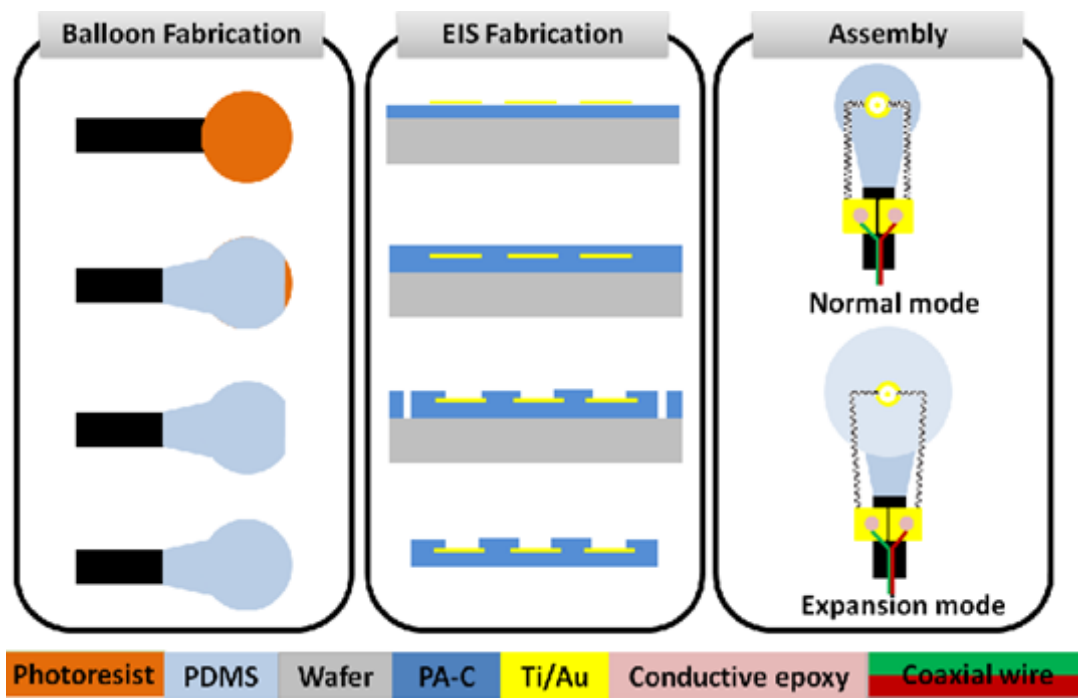


Figure 2.5. Fabrication process of the catheter-based balloon-inflatable microelectrode sensor.

In parallel, a 30 gauge Luer-lok needle was epoxied into a 5 cm section of similar capillary tubing. The free end of the tubing was then epoxied over a 30 cm section of 200 μm steel tubing. The steel tubing was more flexible and less brittle than the capillary tubing, rendering the overall device more robust for intravascular interrogation. This assembly was cured in an oven at 100 °C, and checked for blockage by pushing air into a beaker of water via a syringe. The entire device was then dried in an oven. The open end was inserted into that of the balloon's capillary tubing and secured into place. The epoxy was spread over the silicone in contact with the capillary tubing to prevent balloon delamination.

To fabricate the impedance sensor, a 5- μm -thick bottom parylene C was deposited onto a hexamethyldisilazane-treated (HMDS) silicon wafer. Then a metal layer of Titanium/Gold (Ti/Au) (0.02 μm / 0.2 μm) was deposited by thermal evaporation and patterned by chemical wet etching. After the deposition of another 5- μm -thick parylene C layer, the impedance-sensing microelectrodes and contact pads were patterned by oxygen plasma etching. The overall device outlines were finally defined by etching through the parylene C layer. The device was then peeled off from the silicon substrate.

To assemble the impedance sensor to the balloon, the quasi-concentric impedance sensor was attached by applying biocompatible epoxy to the flat side of the balloon with the sensor openings facing up. Next, the two contact pads were connected to a coaxial wire using biocompatible conductive epoxy, and then fully encapsulated and fixed onto the tubing by silicone (PDMS) (Fig. 2.6). The sinusoidal-line connecting the sensing electrodes and the pads allowed a stretchable sensor in response to bubble inflation.

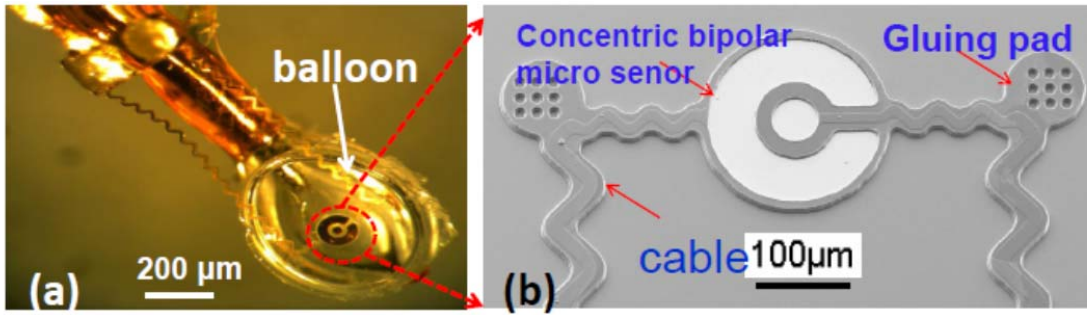


Figure 2.6. (a) The impedance sensor was mounted on a balloon. (b) SEM photo of the finished impedance sensor, highlighting the stretchable sinusoidal cables in response to balloon inflation and the two gluing pads allowed for affixation on the surface of the balloon.

2.2.3 Characterization

2.2.2.1 Impedance Characterization

The impedance sensor with inflatable balloon was placed inside electrolyte-rich blood for impedance characterization and for determining the EIS measurements' baseline. An input of 10 mV peak-to-peak AC voltage and frequency sweeping from 300 kHz to 100 Hz were delivered to the microelectrodes. The magnitudes and phases of the impedance were acquired at 20 data points per frequency decade. The baseline measurement is shown in comparison to the following *ex vivo* and *in vivo* measurements.

2.2.2.2 Inflation Pressure Characterization

The catheter-based impedance sensor with inflatable balloon was deployed into the phosphate saline buffer-filled explants of aorta in which EIS measurements were performed to determine the optimal inflation pressures (Fig. 2.7). At pressures below 6 psi, the balloon was not fully inflated, and sensor was not in contact with the endoluminal

surface. The EIS measurements revealed a baseline impedance of 70 k Ω at low frequency and more resistive behavior at a higher frequency, accompanied by -40 to -45 degrees of phase. At 7 psi, the inflated balloon enabled the microelectrodes to make contact with the vessel wall, resulting in a significant change in the impedance spectrum. At low frequencies, the magnitude of the impedance increased to 300 k Ω . At higher frequencies, the magnitude of the impedance decreased, as the vessel wall was more capacitive compared to saline, accompanied by a decrease in phase to -60 degrees at 100 kHz. At 9 psi, a slight decrease in magnitude and phase were observed, implicating a higher pressure applied by the balloon to the vessel wall, causing local deformation. Hence, our observations suggest that 7 psi is an optimal inflation pressure for EIS measurements with full surface contact and minimum applied force to the endoluminal surface. It is recognized that intravascular blood pressure is considerably higher than atmospheric pressure or the pressure in saline, so that the balloon *in vivo* may not be able to be inflated to the same level *in vitro*.

However, it has been demonstrated that EIS is a powerful tool which can detect when the sensor becomes in contact with the vessel wall. The impedance of blood is significantly lower than that of vascular tissue due to its electrolyte-rich fluid nature, thus the contact between sensor and vascular wall can be detected by observing the significant impedance increase as balloon inflates. This feature allows us to fine tune the balloon inflation *in vivo*.

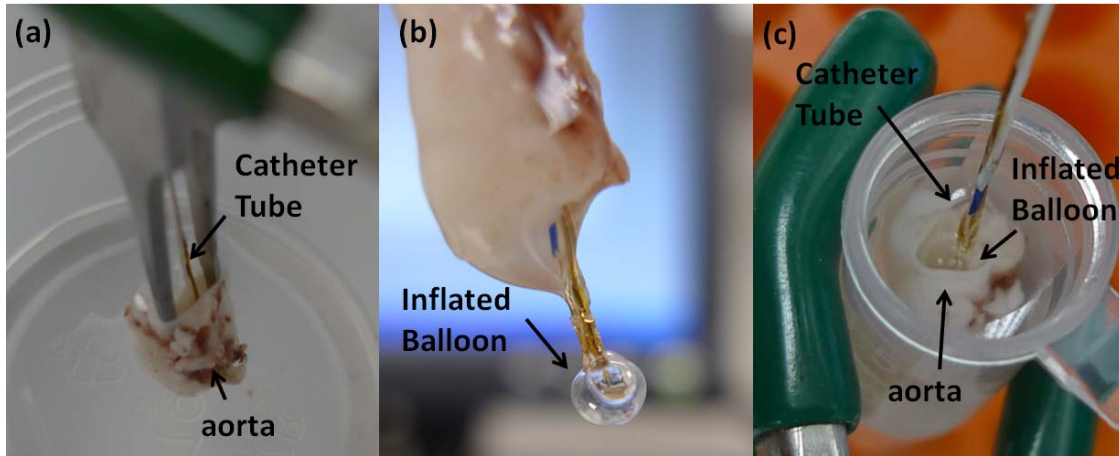


Figure 2.7. Inflation pressure characterization *in vitro* (a) The balloon-inflatable impedance sensor was inserted into the *ex-vivo* rabbit aorta. (b) Demonstration of balloon inflation prior to impedance assessment. (c) Demonstration of intravascular balloon inflation.

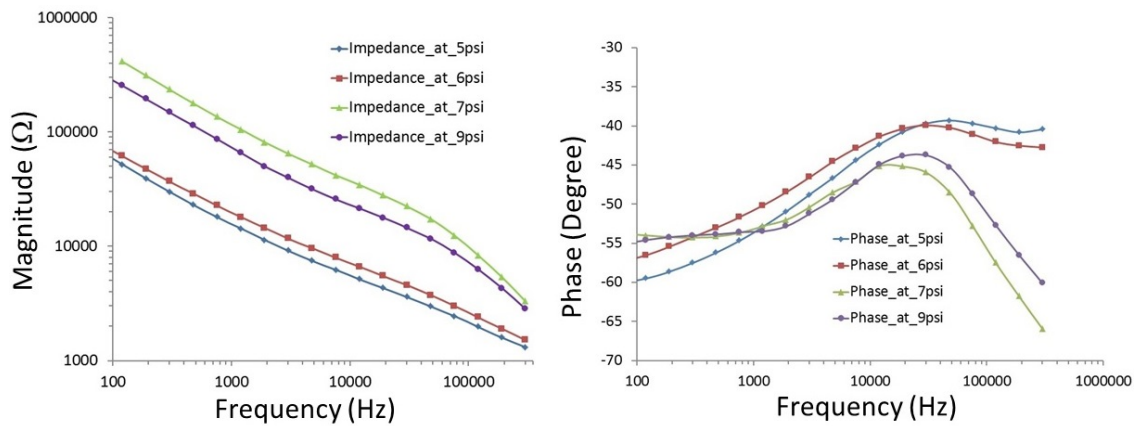


Figure 2.8. Characterization of balloon-inflatable impedance sensor in terms of frequency-dependent changes in impedance magnitude and phase. Data were collected in response to balloon inflation at 5, 6, 7 and 9 psi, respectively. The data revealed that 7 psi was sufficient for adequate contact between the sensor and vessel wall as it showed a significant change in the values at the whole frequency band with magnitude and at

frequencies above 30 kHz with phase. At 9 psi, the balloon was over-inflated representing a slight decrease.

2.3 Experiments and Results

2.3.1 Sample Preparation

In compliance with the Institutional Animal Care and Use Committee (IACUC) at the University of Southern California, four male New Zealand White (NZW) rabbits (10-week-old: mean body weight ~ 2 kg) were purchased from a local breeder (Irish Farms, Norco, CA). NZW rabbits are established as a model of atherosclerotic biology with plaques accessible to catheter interrogation. Two animals were fed a high-fat, high cholesterol diet (Newco® 1.5% cholesterol & 6% peanut oil). After 8 weeks, explants of aortas were interrogated for intravascular electrochemical impedance spectroscopy (EIS). Another two animals were used for feasibility of *in vivo* EIS measurements.

The rabbits were anesthetized for percutaneous access. Intravascular ultrasound (IVUS) probe and microelectrode sensor were sterilized by Electron Beam technology (Titans SureBeam™) and heparinized to prevent thrombosis. A femoral cut-down was performed and a 2-French (distal O.D.) Tracker-10, 80/15 guide catheter (Target Therapeutic) was inserted under binocular magnification and heparin administered (150 units/kg). The catheter and a Dasher-14 Steerable Guide wire (Target Therapeutic) were then advanced under fluoroscopic guidance (Phillips BV-22HQ C-arm) into the aortic arch. The catheter was withdrawn to the thoracic aorta, and lastly, abdominal aorta, for similar interrogations.

2.3.2 *Ex Vivo* EIS Measurements in Fat-Fed NZW Rabbits

EIS measurements were performed in explants of fat-fed rabbit aorta via the balloon-inflatable quasi-concentric microelectrodes. Similar to the previous inflation pressure characterization (Fig. 2.7), inflation of the balloon enables the sensor to be in contact with the endoluminal surface, and significant changes in both impedance and phase spectra were observed (Fig. 2.9). Immunohistochemistry revealed plaque versus plaque-free sites in the insets, respectively (Fig. 2.9a and 2.9b). Balloon inflation-mediated endoluminal contact induced an approximately 20% increase in impedance from 1 kHz to 100 kHz, and a decrease in phase at a frequency above 50 kHz (n=4). EIS sensor contact with the atherosclerotic plaques further resulted in a greater than 50% increase in the impedance spectrum over the entire frequency range (n=4), accompanied by a decrease in phase at the lower frequency range (1 kHz – 10 kHz), reflecting a capacitive property of the tissue. Histological analysis confirmed the presence of foam cell-rich fatty deposition in the endoluminal vessel wall at the plaque sites in contrast to the plaque-free site with an intact tunica intima layer (inset in Fig. 2.9b). Hence, the feasibility of the balloon-inflatable concentric microelectrodes for intravascular interrogation of atherosclerotic plaques was demonstrated.

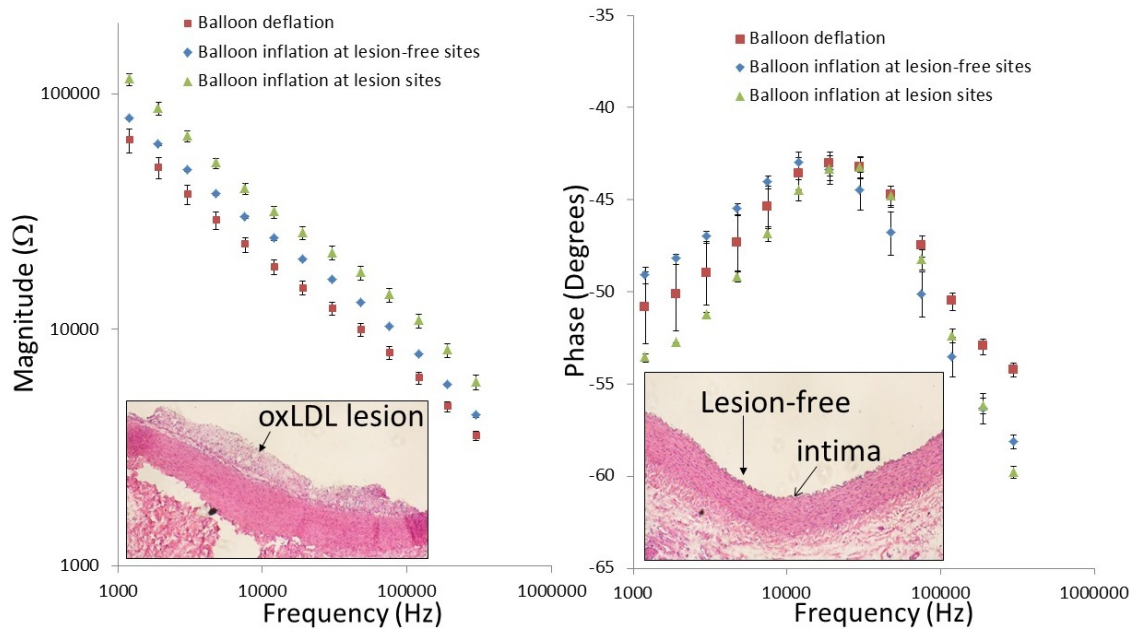


Figure 2.9. *Ex-vivo* EIS acquisition from explanted rabbit aorta and corresponding histology of the aorta wall. After 8 weeks of high-fat diet, rabbits were sacrificed and aortas were extracted and fixed in 15% paraformal aldehyde (PFA). The individual aortas were sectioned into 2-3cm segments and immersed in PBS for deployment of the balloon-inflatable EIS sensor. Endoluminal lipid deposition or atherosclerotic plaques were visible for EIS interrogation and comparison with the disease-free sites. (a) After the balloon inflation, the impedance magnitude increased over the entire frequency range from 1 kHz to 1,000 kHz. EIS measurement further increased significantly at the plaque sites. (b) Corresponding histology revealed intact tunica intima and media layer at plaque-free sites, and accumulation of foam cells at plaque sites.

2.3.3 *In Vivo* EIS Measurements in NZW Rabbit

The deployment of the catheter-based balloon EIS sensor to interrogate carotid arteries of NZW rabbits has been further demonstrated (Fig. 2.10). The angiogram revealed the position of the catheter in relation of the EIS sensor. The impedance of *in vivo* measurements displayed a distinct phase spectrum compared to those of the *ex vivo* findings (Fig. 2.9b) towards the lower frequency range. Both blood serum and vessel wall were more resistive, as reflected in a higher phase changes at -34.1 ± 1.6 and -30.4 ± 0.3 degrees, respectively ($n = 6$). However, the impedance spectra in the frequency range of 10 kHz to 300 kHz displayed a similar pattern to those of *ex vivo* (Fig. 2.9a). Balloon inflation induced an increase in impedance and a decrease in phase towards the higher frequency range.

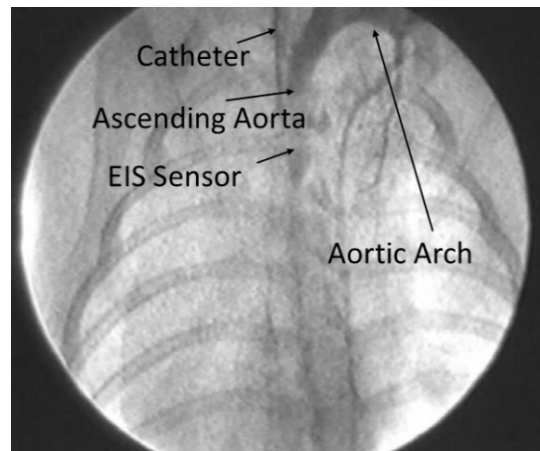


Figure 2.10. Deployment of balloon-inflatable EIS sensors via fluoroscopy guidance in NZW rabbits. The position of EIS sensor was visualized in the carotid artery.

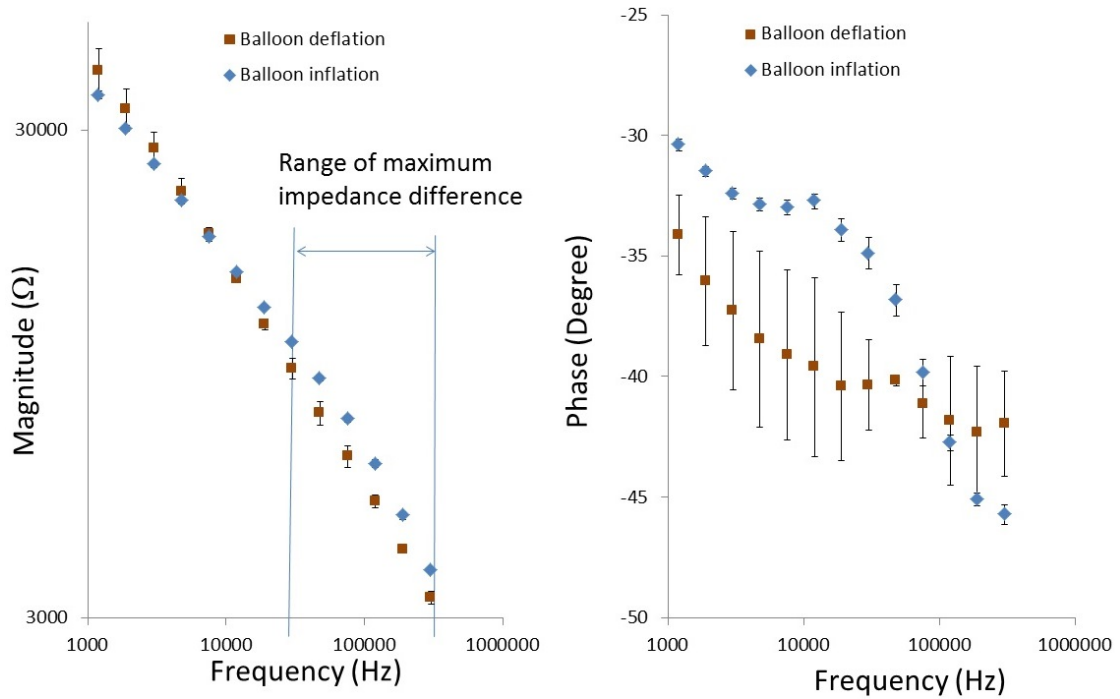


Figure 2.11. *In-vivo* EIS acquisition in the rabbit carotid arteries. Balloon-inflatable EIS sensor packaged onto an in-house-built balloon catheter. The catheter was deployed through right carotid artery cut-down and the sensor made endoluminal contact under the fluoroscopic guidance. Inflation of the balloon resulted in a significant increase in the frequency-dependent impedance magnitude, from 10 kHz to 300 kHz, along with distinct phase characteristics.

2.4 Discussion

The novelty of the study lies in the intravascular deployment of flexible and stretchable intravascular EIS technology to assess oxLDL-rich atherosclerotic plaques. Biological tissues possess energy storing and dissipation properties, thus could be detected and classified by endoluminal EIS measurement. The use of a linear array of

electrodes has been utilized, but showed limits in size as well as capability to detect small and non-homogenous plaques [10-12]. The concentric microelectrodes enabled highly sensitive EIS measurement of the electrochemical tissue properties at close proximity without interference from the surroundings.

The features of flexible and stretchable electronics have made real-time endoluminal assessment of lipid-rich plaques possible. Here, stretchable sensors have been characterized in terms of distinct changes in impedance and phase spectra in response to various pressures of balloon inflation (Fig. 2.9). Baseline EIS measurements before and after balloon inflation were established, followed by the comparison of EIS magnitudes in the presence or absence of lipid-rich plaques. The inflation of the balloon at 7 psi enabled the EIS sensors, in minimal contact with the endoluminal surface, providing significant differences in both impedance magnitude and phase changes at frequencies above 30 kHz (Fig. 2.9 and 2.11). Thus, the first intravascular impedance sensor that is both flexible and stretchable for *in-vivo* applications was demonstrated.

Oxidized low density lipoprotein (oxLDL) induces transformation of macrophages to lipid-laden foam cells [13]. Activated macrophages secrete matrix metalloproteinase (MMPs) to mechanically destabilize plaques [14, 15]. Growing evidence suggests that oxLDL and thin-cap fibroatheromas (TCFA), rich in macrophage/foam cells, are prone to mechanical stress and destabilization [16-18]. Using the novel concentric microelectrode sensor, it was demonstrated that oxLDL-laden foam cells in the subendothelial layer of plaque significantly increased the frequency-dependent EIS magnitude in New Zealand White (NZW) rabbits on diet-induced

hyperlipidemia. Elevated EIS signals were reproduced in the oxLDL-rich, but not oxLDL-free, plaques [19].

An equivalent circuit model was provided here to illustrate the EIS measurement in intravascular tissue. Briefly, EIS measures intrinsic electrochemical properties of the tissue which depend on the chemical composition of the local tissue at the vicinity of the sensor. In particular, water content, electrolyte concentration and lipid content are a few of the most important factors affecting tissue impedance. Accumulation of oxLDL at the measurement site would significantly reduce water content, which is essentially the electrical conduction pathway, resulting in higher tissue impedance to electrical input signals, as well as more capacitive effect at high frequency. As demonstrated previously, it is feasible to establish a correlation between the status of the plaque and the resulting impedance in a certain frequency range, thus allowing accurate detection of the oxLDL-rich, mechanically unstable plaques.

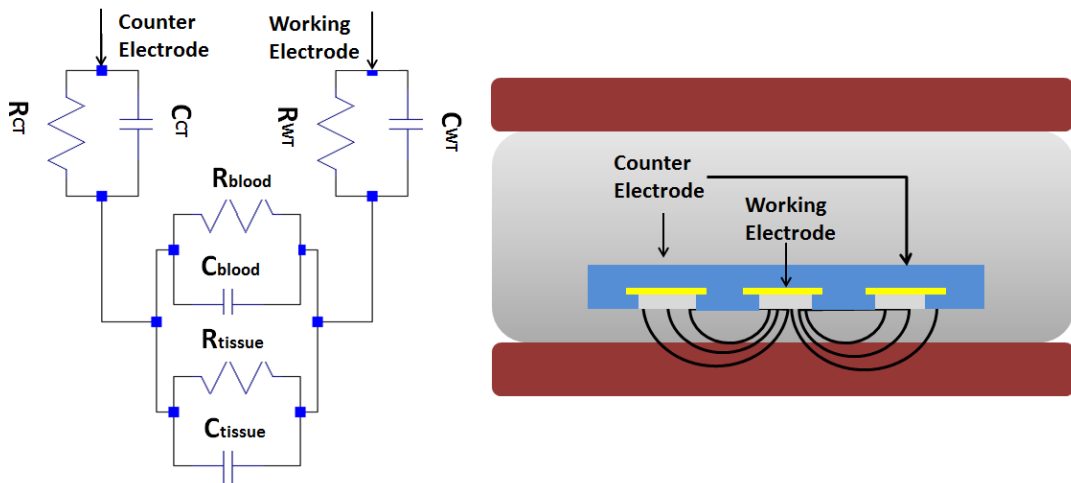


Figure 2.12. Equivalent circuit of the *in vivo* impedance sensing configuration.

In summary, this current study presents the use of a robust and innovatively designed balloon-inflatable catheter-based concentric EIS sensor that could be used for the detection of endoluminal electrochemical properties. The demonstrations on explants from fat-fed NZW rabbit aortas and carotid arteries via *in-situ* and *in-vivo* trials further confirmed the link between endoluminal properties with pre-atherosclerotic plaques. The new features of real-time measurement as well as the stretching capability offer potential for clinical monitoring and integration with emerging flexible electronics for diagnosis and prognosis.

2.5 Conclusion

This work demonstrated the feasibility of stretchable electrochemical impedance spectroscopy (EIS) sensors for endoluminal investigations in New Zealand White (NZW) rabbits. The parylene C-based impedance sensor was mounted on the surface of an inflatable silicone balloon affixed to the tip of an interrogating catheter. The stretchable EIS sensors were deployed to the explants of NZW rabbit aorta for detection of lipid-rich atherosclerotic plaques, and to the live animals for demonstration of balloon inflation and EIS measurements. An input peak-to-peak AC voltage of 10 mV and sweeping-frequency from 300 kHz to 100 Hz were delivered to the endoluminal sites. Balloon inflation allowed EIS sensors to be in contact with the endoluminal surface. Impedance magnitude increased in the entire frequency band by 1.5-fold and the phase dropped by ~5 degrees at frequencies below 10 kHz in the oxLDL-rich plaques in response to balloon inflation in the explants of aortas from fat-fed rabbits. In the plaque-free sites of the normal diet-fed rabbits, impedance magnitude increased by 1.2-fold at frequencies above 30 kHz and phase shifted by ~5 degrees. The feasibility of stretchable EIS sensors for endoluminal

interrogation was demonstrated; providing a new intravascular strategy to identify high-risk plaques.

2.6 References

- [1] Y. C. Fung, *Biomechanics: Circulation*, second edition ed.: Springer, 1997.
- [2] J. Bamford, P. Sandercock, M. Dennis, J. Burn, and C. Warlow, "Classification and natural history of clinically identifiable subtypes of cerebral infarction," *Lancet*, vol. 337, pp. 1521-1526, 1991.
- [3] Q. Rasheed, P. J. Dhawale, J. Anderson, and J. M. Hodgson, "INTRACORONARY ULTRASOUND-DEFINED PLAQUE COMPOSITION - COMPUTER-AIDED PLAQUE CHARACTERIZATION AND CORRELATION WITH HISTOLOGIC SAMPLES OBTAINED DURING DIRECTIONAL CORONARY ATHERECTOMY," *American Heart Journal*, vol. 129, pp. 631-637, Apr 1995.
- [4] G. A. Rodriguez-Granillo, H. M. Garcia-Garcia, E. P. Mc Fadden, M. Valgimigli, J. Aoki, P. de Feyter, *et al.*, "In vivo intravascular ultrasound-derived thin-cap fibroatheroma detection using ultrasound radiofrequency data analysis," *Journal of the American College of Cardiology*, vol. 46, pp. 2038-2042, Dec 2005.
- [5] H. Yabushita, B. E. Borna, S. L. Houser, T. Aretz, I. K. Jang, K. H. Schlendorf, *et al.*, "Characterization of human atherosclerosis by optical coherence tomography," *Circulation*, vol. 106, pp. 1640-1645, Sep 2002.
- [6] E. Regar, B. Hennen, E. Grube, D. Halon, R. L. Wilensky, J. Schneiderman, *et al.*, "First in men application of a miniature self-contained intracoronary magnetic

- resonance imaging probe. A multi-center safety and feasibility trial," *European Heart Journal*, vol. 27, pp. 515-515, Aug 2006.
- [7] K. R. Aroom, M. T. Harting, C. S. Cox, R. S. Radharkrishnan, C. Smith, and B. S. Gill, "Bioimpedance Analysis: A Guide to Simple Design and Implementation," *Journal of Surgical Research*, vol. 153, pp. 23-30, 2009.
- [8] K. R. Foster and H. P. Schwan, "Dielectric properties of tissues," *Handbook of biological effects of electromagnetic fields*, pp. 25-102, 1996.
- [9] L. Marcu, M. C. Fishbein, J. M. I. Maarek, and W. S. Grundfest, "Discrimination of human coronary artery atherosclerotic lipid-rich lesions by time-resolved laser-induced fluorescence spectroscopy," *Arteriosclerosis, Thrombosis, and Vascular Biology*, vol. 21, pp. 1244-1250, 2001.
- [10] T. Süsselbeck, H. Thielecke, J. Köchlin, S. Cho, I. Weinschenk, J. Metz, *et al.*, "Intravascular electric impedance spectroscopy of atherosclerotic lesions using a new impedance catheter system," *Basic Research in Cardiology*, vol. 100, pp. 446-452, 2005/09/01 2005.
- [11] I. Streitner, M. Goldhofer, S. Cho, H. Thielecke, R. Kinscherf, F. Streitner, *et al.*, "Electric impedance spectroscopy of human atherosclerotic lesions," *Atherosclerosis*, vol. 206, pp. 464-468, 2009.
- [12] M. K. Konings, W. Mali, and M. A. Viergever, "Development of an intravascular impedance catheter for detection of fatty lesions in arteries," *IEEE transactions on medical imaging*, vol. 16, pp. 439-446, 1997.

- [13] M. S. Brown and J. L. Goldstein, "Lipoprotein metabolism in the macrophage: implications for cholesterol deposition in atherosclerosis," *Annual Review of Biochemistry*, vol. 52, pp. 223-261, 1983.
- [14] G. C. Cheng, W. H. Briggs, D. S. Gerson, P. Libby, A. J. Grodzinsky, M. L. Gray, *et al.*, "Mechanical strain tightly controls fibroblast growth factor-2 release from cultured human vascular smooth muscle cells," *Circulation Research*, vol. 80, pp. 28-36, 1997.
- [15] Y. S. Kim, Z. S. Galis, A. Rachev, H. C. Han, and R. P. Vito, "Matrix metalloproteinase-2 and-9 are associated with high stresses predicted using a nonlinear heterogeneous model of arteries," *Journal of Biomechanical Engineering*, vol. 131, pp. 011009-011018, 2009.
- [16] S. Ehara, M. Ueda, T. Naruko, K. Haze, A. Itoh, M. Otsuka, *et al.*, "Elevated levels of oxidized low density lipoprotein show a positive relationship with the severity of acute coronary syndromes," *Circulation*, vol. 103, pp. 1955-60, Apr 17 2001.
- [17] S. Zeibig, Z. Li, S. Wagner, H. P. Holthoff, M. Ungerer, A. Bultmann, *et al.*, "Effect of the oxLDL Binding Protein Fc-CD68 on Plaque Extension and Vulnerability in Atherosclerosis," *Circulation research*, vol. 108, pp. 695-703, 2011.
- [18] G. Chinetti-Gbaguidi, M. Baron, M. A. Bouhlef, J. Vanhoutte, C. Copin, Y. Sebti, *et al.*, "Human Atherosclerotic Plaque Alternative Macrophages Display Low Cholesterol Handling but High Phagocytosis Because of Distinct Activities of the

- PPAR {gamma} and LXR {alpha} Pathways," *Circulation Research*, vol. 108, pp. 985-995, 2011.
- [19] F. Yu, X. Dai, T. Beebe, and T. Hsiai, "Electrochemical impedance spectroscopy to characterize inflammatory atherosclerotic plaques," *Biosensors and Bioelectronics*, vol. 30, pp. 165-173, 2011.

Chapter 3 Flexible Microelectrode Membrane for Epicardial ECG Recording

Chapter 3 describes a flexible microimplant for long-term epicardial electrocardiogram (ECG) signals recording to assess heart regeneration in small animal models, which remains one of the most challenging scenarios in *in vivo* sensing.

Section 3.1 introduces the significance of long-term ECG recording in heart regeneration processes, discusses the hardware implementation of a typical ECG recording system, lists various wired, wearable and implantable ECG recording systems, and identifies specific challenges associated with a long-term ECG recording system for heart regeneration monitoring. Following that, **section 3.2** develops a long-term wearable parylene C membrane containing multiple microelectrodes. The microelectrode membrane can be percutaneously implanted and can record epicardial ECG signals from specific regions of zebrafish heart. However, with this passive microelectrode membrane, animals need to be sedated and external connections need to be made for each measurement. Therefore, **section 3.3** further demonstrates the wireless operation of the microelectrode membrane with a wireless ECG recording system prototyped on a printed circuit board (PCB). ECG signals were continuously recorded and wirelessly transmitted from a non-sedated neonatal mouse model of heart regeneration. To accomplish a substantial miniaturization of the PCB prototype, a parylene C printed circuit membrane platform for flexible circuit integration is presented in **section 3.4**. The circuit membrane layout design and assembly techniques of different small components were formulated

individually and configured collectively. The same wireless ECG recording system was demonstrated on a flexible, light-weight and compact parylene C printed circuit membrane with the ECG recording microelectrodes monolithically manufactured on the same membrane. Conclusions are summarized in **section 3.5**. The presented flexible, light-weight and compact wireless ECG recording implant could potentially be injected by needle and achieve minimally invasive long-term *in vivo* monitoring.

3.1 Introduction

In human, myocardial infarction results in irreversible loss of heart tissues or cardiomyocytes [1]. The limited capacity of the heart to regenerate injured tissue often leads to heart failure which afflicts nearly five million people in the US with an additional half million diagnosed each year. Despite current diagnosis and therapy regimens, heart failure remains the leading cause of morbidity and mortality in the US and developed world [2].

In contrast, certain fish and amphibians maintain a regenerative capacity throughout the adult life. Zebrafish possess a remarkable capacity to regenerate a significant amount of myocardium in injured hearts [3]. Due to the relatively ease of maintenance and breeding, they present a genetically tractable model system for high throughput regenerative medicine and cardiovascular research [4].

3.1.1 Significance of ECG Recording in Heart Regeneration

Zebrafish heart regeneration has been characterized using molecular, genetic and immunohistochemical approaches; however, the cardiac conduction phenotype in the injured and regenerated cardiomyocytes remains unknown [5]. Zebrafish myocardium

can fully regenerate after 20% ventricular resection over a period of 60 days, as evidenced by histology (**Fig. 3.1**), while whether the structurally regenerated myocardium displays functionally normal conduction phenotype remains undefined [3].

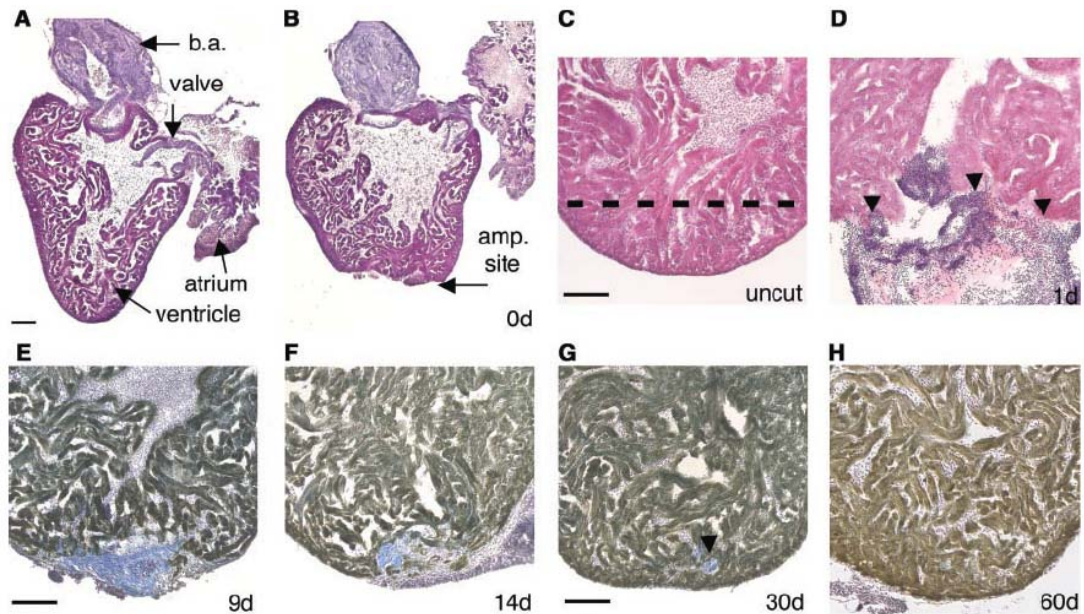


Figure 3.1 Heart regeneration in zebrafish model. In response to ventricular amputation, thrombosis immediately develops to achieve homeostasis in the ventricle. The thrombus is replaced by a fibrin clot 2-4 days post amputation (dpa). Nascent cardiomyocytes replace the vast majority of the lost ventricular tissue by 30 dpa, and the structure of the ventricle is fully restored on 60 dpa without scar tissue. The scale bars are measured 100 μm .

ECG records the action potential of heart muscle cells and shows their electrical activities in the functional dimension. Myocardium cells are like little batteries. They have different ion concentrations inside and outside their membranes, which create small electric potentials. A disturbance in this electric potential can give rise to an action

potential which is the depolarization and repolarization of the cell. Essentially, ECG signals are composed of the superposition of the different action potentials from heart muscle cells.

A typical ECG waveform consists of three primary characteristics: the P wave, the QRS complex, and the T wave (**Fig.3.2**). Each wave corresponds to the electrical activity of a specific region of the heart. The P wave comes first and represents the depolarization of the atria. The QRS complex represents depolarization of the ventricles, and is usually the strongest wave in an ECG. The last wave is the T wave and it represents the repolarization of the ventricles. The repolarization of the atria is usually hidden in the QRS complex and becomes the most challenging characteristic to be detected.

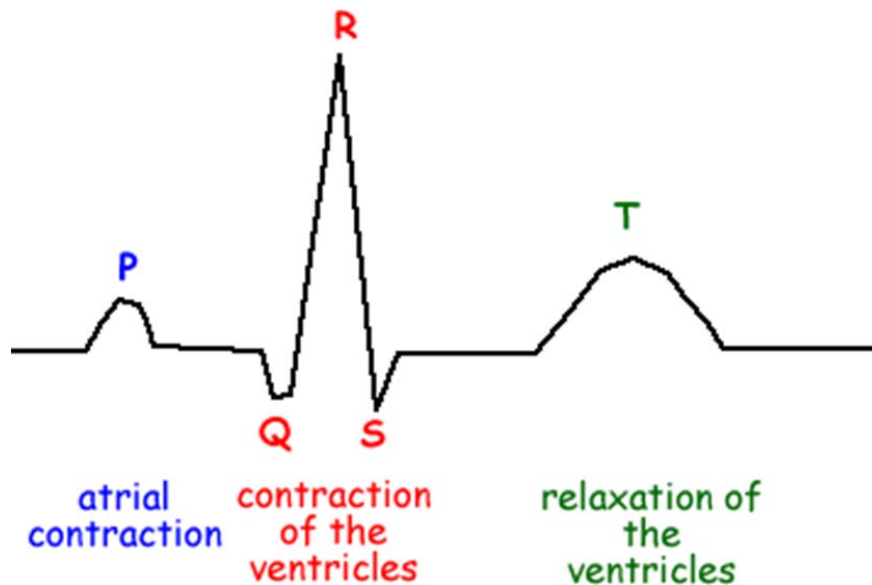


Figure 3.2. A typical ECG waveform and the characteristics: the P wave, the QRS complex and the T wave.

ECG recording during the heart regeneration process can be used to assess the cardiac conduction in response to induced heart injury and to analyze the dynamic signal evolution during regeneration, thus providing a tool for the study of the mechanistic information for the regeneration process and the functional integration of the regenerated cells and host tissue [6].

Despite having a two-chambered heart, the zebrafish heart ECG is fundamentally similar to that of humans in terms of P waves, QRS complexes, and T waves [7]. The critical conduction pathways of the zebrafish in cardiovascular development also parallel that of higher vertebrates. Because cardiac development, structure, and function are relatively conserved between lower vertebrates and mammals, further mechanistic investigations may yield future insights into cellular therapies for human heart failure and myocardial infarctions [8].

3.1.2 Introduction to ECG Recording System

ECG has been long used as a diagnostic tool for medical evaluation. The ECG waveform allows cardiologists to infer information about the electrical activity associated with different aspects of a heart beat and is of particular value for assessing an individual's cardiac rhythm and heart health [9].

The heart pumps blood around the body using a carefully controlled order of contractions of its chambers. The contraction of a muscle cell is a result of a depolarization and repolarization cycle called an action potential during which the potential difference between the inside and outside of the cell changes. Considering all the cardiac cells together, the heart can be viewed as an electrical generator which drives current into a passive resistive medium around the heart [10]. By taking the voltage

differences at different points in the surrounding medium, the electrical activity of the heart can be observed. The ECG signals represent the electrical activity of an ensemble of cells in the myocardium.

To record the ECG, a sensor that can convert the ionic potentials generated by the heart into electronic potentials which can be measured by the conventional electrical circuitry is needed. Following that, due to weak signals, amplification and filtering are required to provide high-quality signals for further transmission, display and analysis.

A completely ECG recording system should have all of the four function modules described in Chapter 1, including signal sensing, signal processing, data transmission and power transmission [14, 15, 16]. With particular relevance to ECG recording, some general design references for each individual module are discussed here.

(1) Signal Sensing:

ECG recording sensors are transducers that convert ionic potential to electrical potential. They typically consist of a pair of electrodes. Electrodes, based on the materials used, can be classified into polarizable, in which case they are modeled as capacitors, or non-polarizable, in which case they behave like resistors [11]. Current flow across the electrode-electrolyte interface is minimal for recording electrodes, so there are no high-rate electrochemical challenges to the electrodes.

(2) Signal Processing:

The strength of ECG signals can vary from the microvolt to millivolt range [12]. Signals picked up by the sensors need to be amplified before being interpreted. On the other hand, ECG signals are subject to many different kinds of noise, internally and externally, during recording, which depend on the data and power transmission schemes,

including the 50/60 Hz pick-up signal, baseline drift, baseline instability, and muscle mechanical movement. These artifacts can be filtered digitally on the software side as well as through analog practices on the hardware side.

(3) The power and data transmissions:

The power and data can be transmitted through wires or wirelessly. For a completely wireless system, signals need to be transmitted through multiple media between the transmitter and receiver side, air, water and biological tissue, by modulating different energy forms like electromagnetic waves, light and ultrasound [13]. Recording usually consumes relatively less power. The power source of a wireless ECG recording system could be a battery, biomechanical and biochemical energy harvester, or inductive link [14].

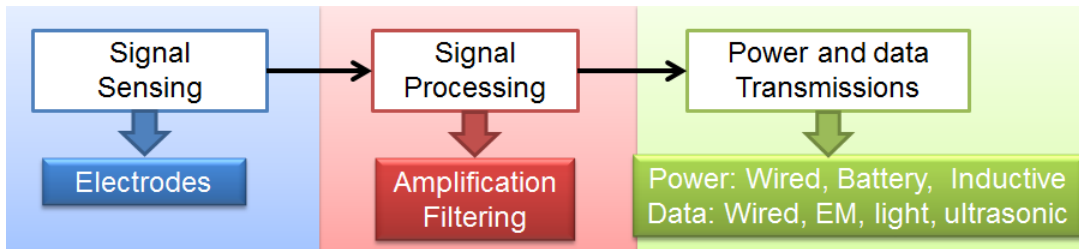


Figure 3.3 Hardware implementation of typical ECG Recording Systems

3.1.3 Overview of Current ECG Recording Systems

Current ECG recording systems can be classified into three categories: wired, wearable and implantable (Fig. 3.4). 12-lead ECG taking a differential measurement of the electrical potential on the body surface at different locations generates different ECG vectors. Six of these leads are in the plane parallel to the body and are known as “frontal” ECG leads. The other six ECG leads are views of the heart in the plane perpendicular to

the body and are known as “pre-cordial” leads. The wearable ECG patch from WIN Human Recorder forms single lead and achieves long-term ECG monitoring during normal activity. The implantable ECG is from Medtronic which can be implanted for 3 years and staying functional *in vivo*. It is fully encapsulated inside a metal case and measures 62 mm in length.

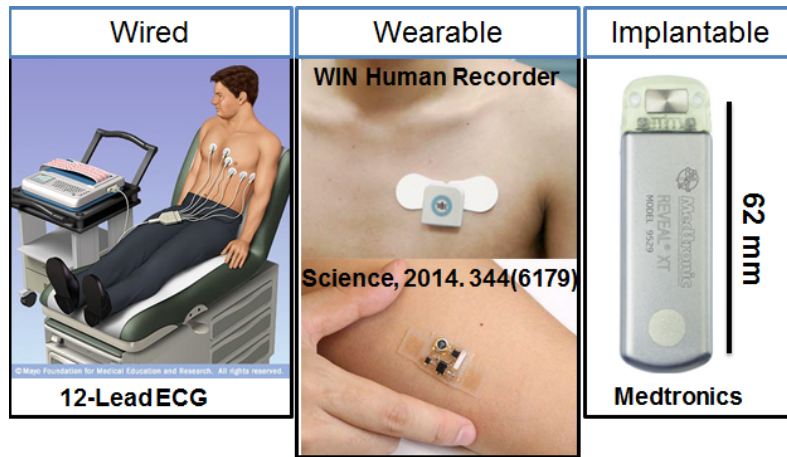


Figure 3.4 Current ECG recording systems: wired, wearable and implantable.

3.1.4 Challenges of Implementing ECG Recording System in Zebrafish for Heart Regeneration Monitoring

The application of heart injury and regeneration monitoring poses unique challenges on the design and implementation of ECG recording systems, especially for small animal models such as zebrafish.

First of all, animal models of heart regeneration are typically induced with different heart injuries to different extents, mechanically or genetically [15]. So it is desirable to implement multi-channel ECG recording corresponding to specific regions on heart. ECG signals of zebrafish were previously recorded using a pair of needle electrodes [16]. A long QT interval was experimentally observed during heart

regeneration. Compared to this global ECG signal recording, region-specific recordings can potentially uncover the aberrant cardiac currents of the injured and regenerating heart. In order to record from a little tiny heart with high spatial resolution, electrodes with small dimensions and proper mechanical fixtures to keep the electrode in close proximity to heart surface are needed. To tackle this challenge, **section 3.2** demonstrates a long-term wearable membrane with the four embedded microelectrodes percutaneously implanted into zebrafish heart for epicardial ECG recording. It is also demonstrated here the feasibility of using ECG signals as a functional characterization of heart injury and heart regeneration.

Secondly, heart regeneration can take up to two months [17]. A wireless and continuous recording would be ideal, otherwise animals need to be sedated and electrical connections have to be made for every ECG measurement. **Section 3.3** describes the continuous and wireless operation of the wearable microelectrode membrane. The signal processing, data transmission and power management modules were prototyped on a printed circuit board. Wireless recording was demonstrated on a non-sedated neonatal mouse.

Thirdly, the wireless recording system for long-term ECG monitoring can be useful only under the condition that the wireless ECG recording system does not cause any burden or stress on the animal models. Otherwise, the ECG signals can be influenced. Given the small dimensions of zebrafish and zebrafish hearts, only an extremely flexible and miniaturized wireless ECG system is applicable for zebrafish. **Section 3.4** presents the same wireless ECG recording system implemented on a flexible, lightweight and compact parylene C printed circuit membrane.

3.2 Wearable Microelectrode Membrane

In this section, a wearable microelectrode membrane was developed to achieve multi-channel region-specific ECG recording over a prolonged period. The membrane was percutaneously implanted into zebrafish through open chest surgery and carried by the fish during normal swimming. ECG signals were obtained periodically in air with the zebrafish sedated. Aberrant cardiac ECG signals were observed with injured and regenerating hearts.

3.2.1 Design

The microelectrode membrane, with titanium/gold recording electrodes embedded in parylene C and selectively exposed at recording sites, was designed. In consideration of the long-term recording requirement, parylene C was chosen as the substrate and insulating material due to the well-suited combination of good biocompatibility (FDA approved, USP class VI) and low permeability against water, gases, and ions. Titanium/gold was chosen as the electrode material because of good biocompatibility.

The zebrafish measures about 3-4 cm in length and the fish heart has a diameter of only 1 mm [3]. Therefore, the total length of the microelectrode membrane is only 12.8 mm and all the recording electrodes stay within a circle of 1 mm diameter (Fig. 3.3). Four recording electrodes with different diameters of 300 μm , 200 μm , and 100 μm were arranged in a diamond shape to access the atrium, apical ventricle, and left and right edges of the ventricle.

The membrane has a five-layered stack structure: an underlying ground layer exposed to bias the fish body to the circuit ground, a patterned signal layer including the

recording electrodes, cables and connecting pads, and three insulating parylene C layers on the top and the bottom and in the middle.

The membrane has a central strip with one end composed of four percutaneous electrodes implanted onto the chest epicardially and the other end connected to a flexible flat cable (FFC) end for external circuitry connection. The two side wings with three suture holes on each side form a length-adjustable belt wrapping around the fish body posterior to the pectoral fin to fixate the device.

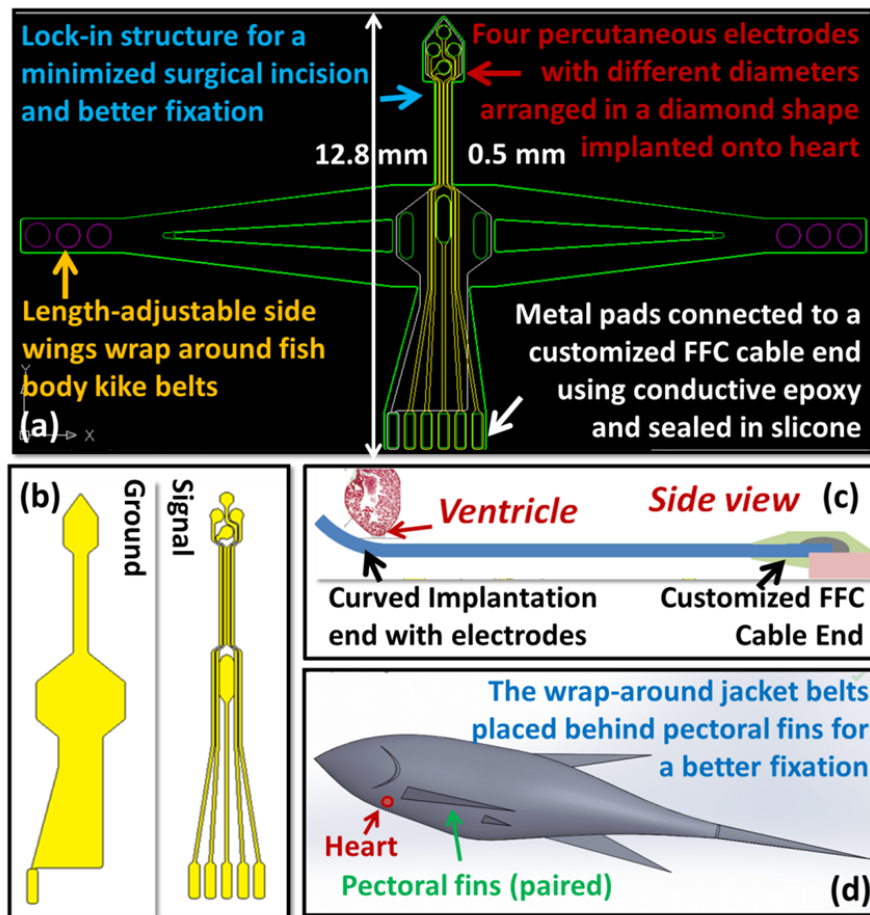


Figure 3.5. Device design. (a) Top-view of the overall device geometry; (b) ground and signal metal layouts; (c) the side-view of device placement after implantation; (d) the 3D view of device fixation.

3.2.2 Fabrication

A 5- μm -thick bottom parylene C layer was first deposited onto a hexamethyldisilazane-treated (HMDS) silicon wafer. Next, the ground metal layer of Ti/Au (0.02 μm /0.2 μm) was deposited by thermal evaporation and patterned by chemical etching. After a 5- μm -thick middle PA-C layer was deposited, the signal metal layer was deposited and patterned and a subsequent 5- μm -thick top PA-C layer was deposited in the same way. Then, the recording electrodes and connecting pads on the signal metal layer, and the biasing electrodes and connecting pads on the ground metal layer were opened by oxygen plasma etching. The overall device outlines were finally defined by etching through the structural parylene layers. The membrane was then dry-peeled off from silicon substrate.

Thermal treatment was applied to generate the specific curvature for the electrode array end to better capture the ventricle contour after implantation. The post assembly with the customized FFC cable end resulted in the pluggable connection, with external circuit and light implant, for fish to carry.

After thermal annealing, an upward warp matching the ventricle contour was produced at the electrode array end. The connecting pads were electrically connected to a customized FFC cable end via conductive epoxy, and the biocompatible polydimethylsiloxane (PDMS) was applied to establish the electrical insulation and enhance the mechanical strength.

The geometry design for the implantation end and the upward curvature provided a lock-in mechanism, hence a good epicardial contact with the heart ventricle after

insertion (Fig. 3.5). The device has a total weight of less than 50mg, and a thickness of less than 0.5mm with FFC cable attached. It was demonstrated to have no observable impact on zebrafish's posture or swimming capabilities.

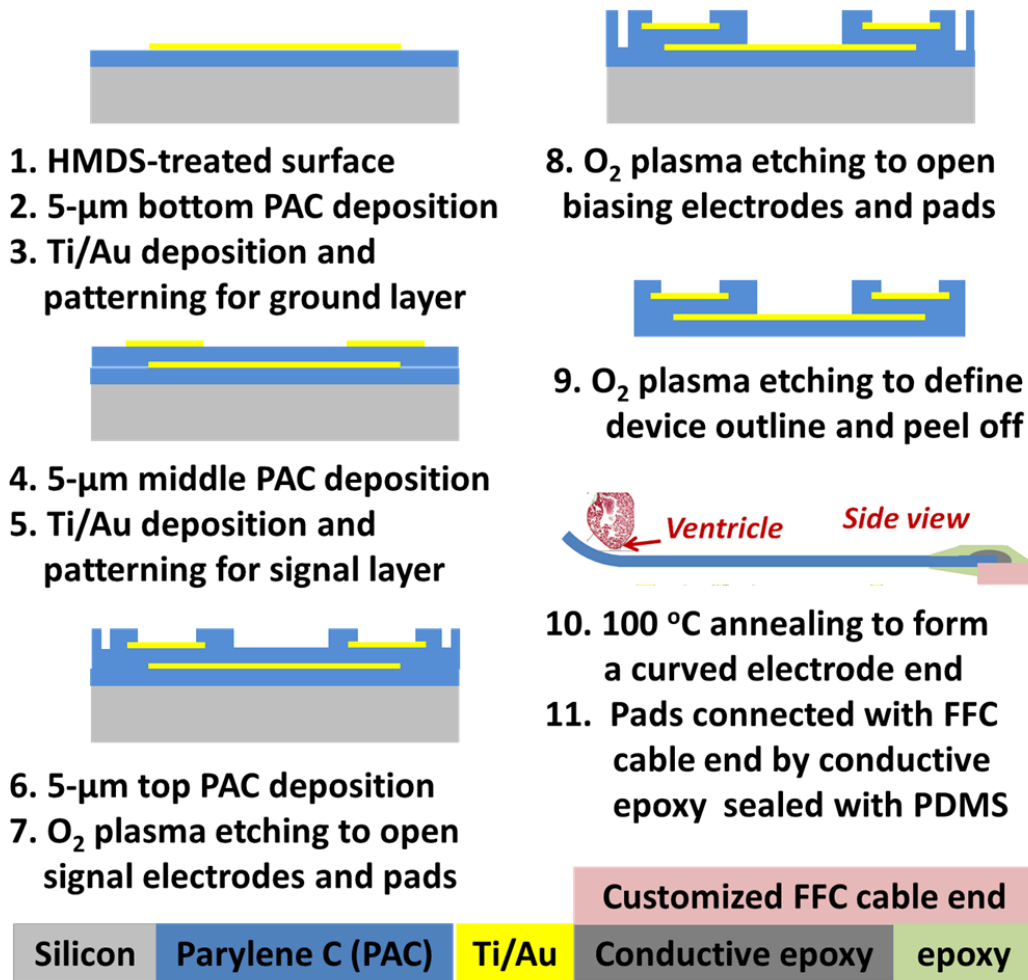


Figure 3.6. Fabrication process of the microelectrode membrane.

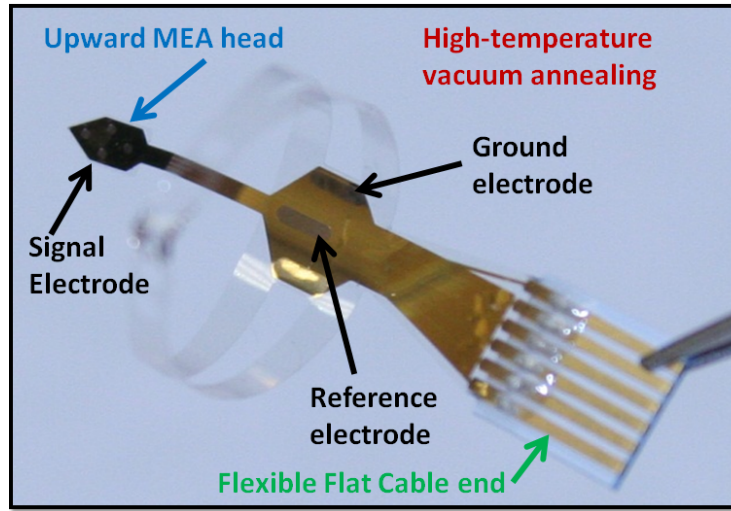


Figure 3.7. Microelectrode membrane after annealing and assembling.

3.2.3 Characterization

The impedance model of the electrode-electrolyte interface and magnitude of the impedance are important for designing a recording system. The interface formed by the planar metal electrode and conductive fish body fluid can be modeled as a capacitor in parallel with a resistor. In the low frequency range (up to 100 Hz) where zebrafish ECG signal concentrates, the capacitor dominates and the value is proportional to the interface area, i.e. the electrode opening. Smaller electrodes will result in higher spatial resolution, while the higher interface impedance may cause significant voltage drop across the interface. The zebrafish heart measures 1 mm in diameter. To accommodate four electrodes as designed in this extremely limited area, the maximum diameter of each electrode is about 300 μm . Therefore, electrodes with diameters of 50 μm , 100 μm , 200 μm and 300 μm were compared in terms of the impedance modulations up to 300 KHz (Fig. 3.6). Microelectrodes with diameter of 300 μm showed best signal strength compared to smaller microelectrodes.

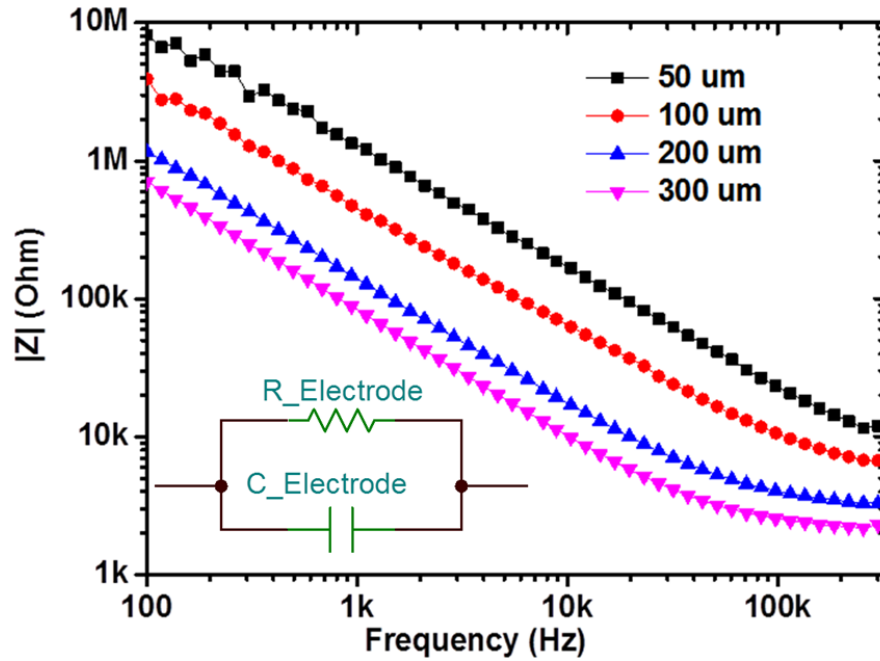


Figure 3.8. Microelectrode model and magnitude of electrode impedances with different dimensions.

3.2.4 ECG Recording from Zebra Fish

3.2.4.1 Animal Preparation

Sedated adult zebrafish (in 0.04% Tricaine methane sulfonate - Tricaine) were placed on a damp sponge for a stereo microscope operation of an open-chest procedure. Ventricular injury was induced by applying a liquid-nitrogen-chilled metal probe (diameter 0.8 mm) for 24 seconds. The fish was returned to the fresh water for recovery.

After 3-7 days, the fish underwent MEA implantation. A 2-mm-long horizontal incision was created at 0.5 mm caudal to the heart. The membrane can be percutaneously implanted through a 0.5-mm-long incision on the zebrafish chest. Then the parylene-encapsulated central strip was fixed along the abdomen by wrapping the side wings around the zebrafish like a belt (Fig. 3.7). The MEA head containing four working

electrodes (WE) was inserted into the epicardium while the reference electrode (RE) was anchored towards the fish tail.. The fish were allowed to recover in water free of Tricaine.

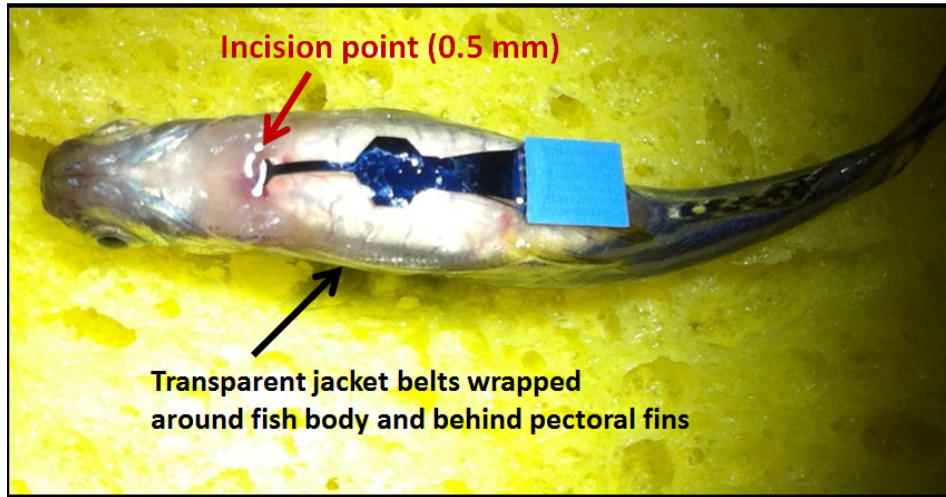


Figure 3.9. Zebrafish with microelectrode membrane percutaneously implanted through an open-chest incision. The parylene C-based jacket was wrapped around the zebrafish and placed behind the pectoral fins.

3.2.4.2 Recording Setup

During each electrical signal acquisition, the sedated fish with the implant was placed on a damped sponge upside down. The FFC cable end was then inserted to a zero insertion force (ZIF) connector and connected to the recording circuitry. The whole setup was in a Faraday cage (Fig. 3.8).

The signals were amplified by 10,000-fold (A-M Systems Inc. 1700 Differential Amplifier, Carlsborg, WA), and filtered with a bandpass filter between 0.1 and 500 Hz as well as a notch filter of 60 Hz. The filtered signals were digitized at a sampling rate of 1,000 Hz (National Instruments USB-6251 DAQ device, Austin TX, and LabVIEW 8.2).

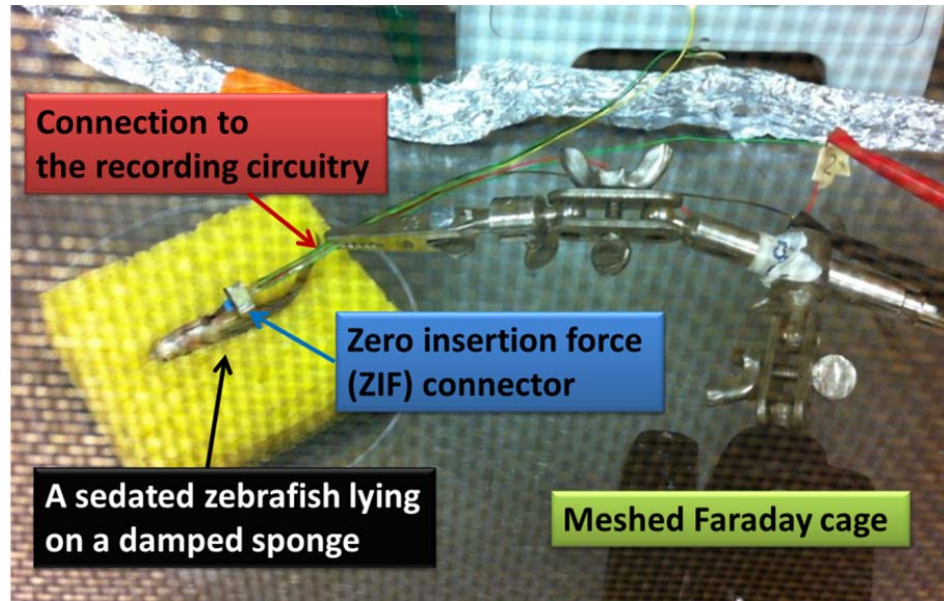


Figure 3.10. Recording setup inside a Faraday cage.

3.2.4.3 The Equivalent Recording Circuit

The simplified equivalent recording circuit is composed of the front-end metal/electrolyte interface model, the parasitic shunt capacitor and the back-end instrumentation amplifier with high input impedance. The conductive fish body was modeled as a resistor network. A particular recording electrode (A, B, C, or D) and the reference electrode were probed into two different points of this resistor network, one proximally to the heart and the other towards the tail. The shunt capacitors between the recording cables and decoupled to the fish body remained small and negligible as compared to the electrode interface impedances and instrumentation amplifier input impedance. The input impedance of the instrumentation amplifier stayed high as a parallel 1000 GΩ resistor with a 5 pF capacitor. The impedances of a working electrode with a diameter of 300 μm versus the reference electrode remained below 1 MΩ at 100 Hz, ensuring a significant voltage drop across the instrumentation amplifier.

To minimize decoupling through the low-impedance path formed by fish body, the recording electrode should be positioned proximal to the source of cardiac conduction.

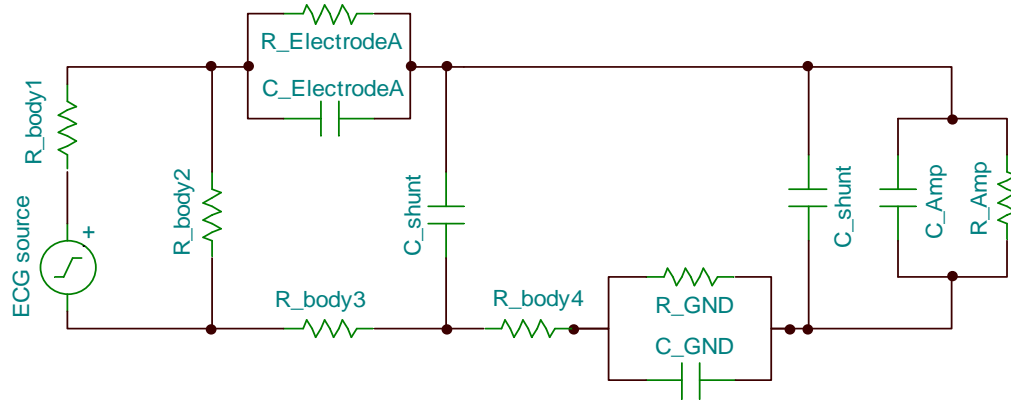


Figure 3.11. Simplified equivalent recording circuit when recording from electrode A and the ground electrode.

3.2.4.4 Data Processing of Recorded ECG Signal

The signal-to-noise ratio (SNR) was enhanced by using both wavelet analysis and noise-reduction techniques. Initial ECG signals were recorded at 1,000 Hz. A wavelet transform was performed by breaking down the signals into 10 frequency segments ranging from 0Hz to the Nyquist frequency (i.e. 500 Hz). A pre-selected threshold value was applied to each individual frequency segment to suppress noise while retaining signal components. Table 3.1 shows the signal strength distribution of a representative ECG across each frequency segment.

Table 3.1 Signal strength distribution of a representative ECG across each frequency segment.

Frequency Range (Hz)	P wave	QRS complex	T wave	Noise	Baseline drift	Threshold setting
125 – 500	0	0	0	1	0	1
62.5 – 125	0.7	1	0	0.7	0	0.7
31.3 – 62.5	0.4	1	0	0.1	0	0.1
15.6 – 31.3	0.4	1	0	0.1	0	0.1
7.8 – 15.6	0.4	1	0.3	0.1	0	0.1
3.9 – 7.8	0.1	0.1	1	0.1	0	0
2.0 – 3.9	0.1	0.1	1	0.1	0	0
0 – 2.0	0	0	0	0	1	1

High frequency signals were completely filtered out due to high level of noise; a small threshold value was set in the frequency range 7.8-62.5 Hz to remove the residual noise. Signals in the frequency range between 2.0 Hz and 7.8 Hz were kept intact to preserve T waves. The baseline drifting was eliminated by removing signals below 2 Hz. The processed ECG signals were reconstructed by inverse wavelet transform. The P waves, QRS complexes and T waves were retained, allowing significantly improved SNRs from approximately 2 dB for the raw data to 7.1 dB after processing.

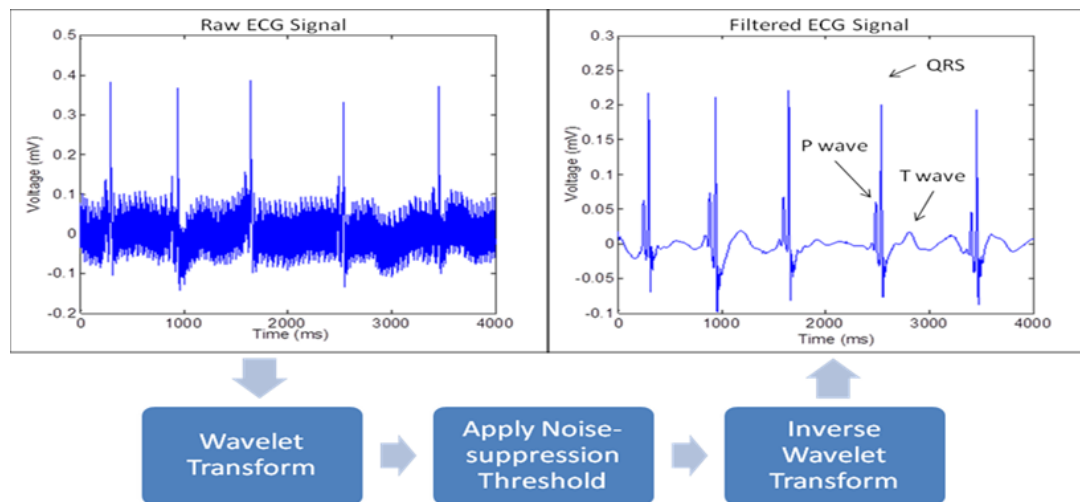


Figure 3.12 Data processing of recorded ECG signals.

3.2.5 Results and Discussion

3.2.5.1 Reproducible ECG Signals Recorded via the Microelectrode Membrane

The feasibility of the flexible microelectrode membrane in the freely swimming zebrafish has been demonstrated. The membrane is water-resistant. Despite the rapid movement of zebrafish during normal swimming, the head portion of the microelectrode membrane remained anchored in the epicardium, allowing for recording reproducible P wave, QRS complex and T waves on day 3 (Fig. 3.10). Currently, application of the surgical glue to the incision site of the fish promotes inflammatory responses, precluding further monitoring after day 3.

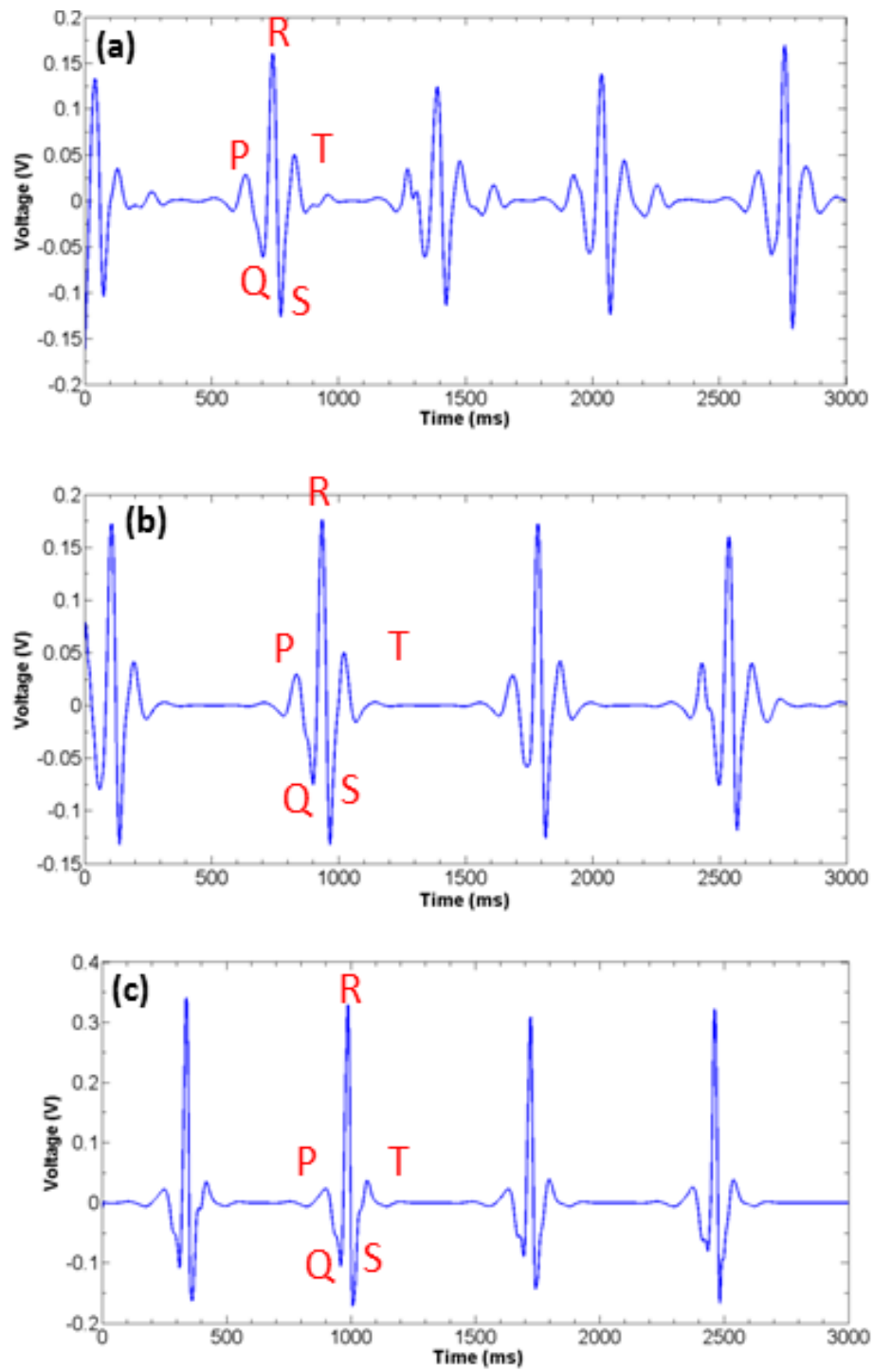


Figure 3.13. Zebrafish ECG signals acquired via an implanted MEA membrane over 3 days. Electrical signal acquisition revealed P wave, QRS complexes and T waves from the same animal on (a) Day 1, (b) Day 2, and (c) Day 3, respectively.

3.2.5.2 Cryo-Injury-Induced Aberrant Electrical Phenotypes in Zebrafish

In response to cryo-injury, there was a significant change in ECG signals, revealing abnormal electrical repolarization in the cryo-injured heart. To investigate the injury-related aberrant electrical currents, ECG signals were recorded prior to cryo-injury and repeated on day 3 with the wearable microelectrode membrane percutaneously implanted. No significant drifts in ECG signals in terms of P waves and QRS complexes were observed. Injury currents, namely ST-depression, were observed and persisted on day 3 (Fig. 3.11). Unlike human ECGs, the T wave became more distinct in response to cryo-injury in zebrafish. Thus, the use of microelectrode membrane highlighted the feasibility of applying high-density microelectrodes to uncover small regions of myocardial ischemia with a minimally invasive approach.

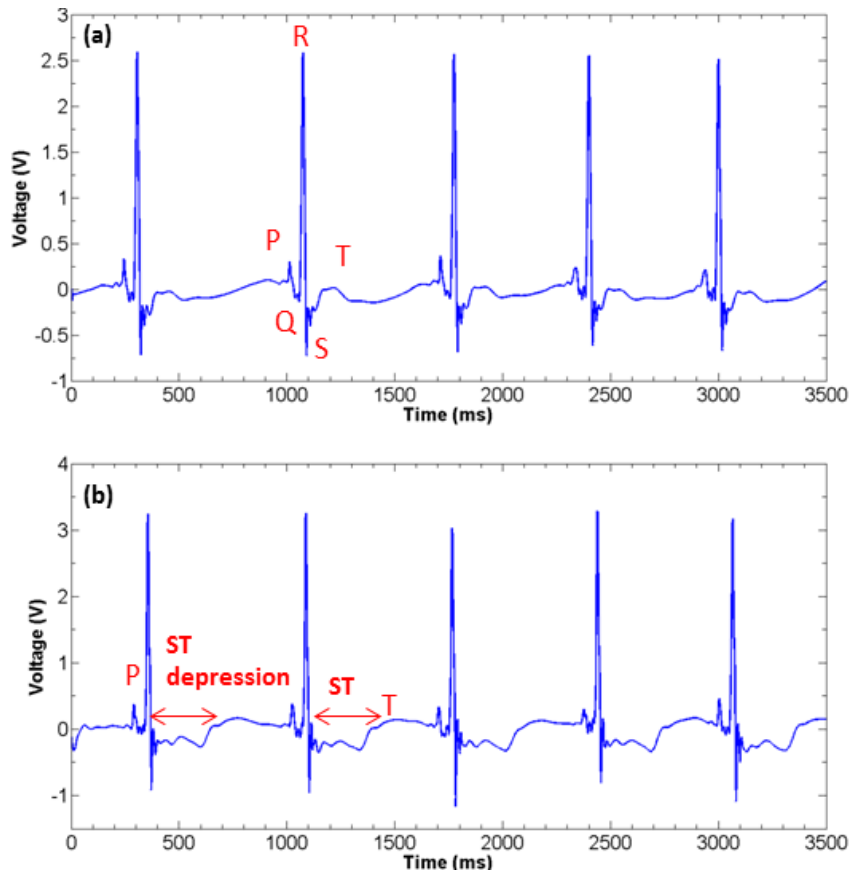


Figure 3.14. ST depression in response to cryo-injury. ECG signals acquired from the flexible microelectrode membrane percutaneously implanted in the same zebrafish (a) prior to, and (b) post cryo-injury on day 3. Myocardial ischemia remained on Day 3 as evidenced by ST depression.

3.2.5.3 Multi-Channels to Acquire Injury Currents

In 4-chamber human hearts, 12-lead surface ECG has routinely been used to identify the specific regions of myocardial injury [18]. In the 2-chamber zebrafish heart, 4-lead surface ECG has made the detection of region-specific cryo-induced injury possible. The ECG signals recorded from all four working electrodes (A, B, C and D) show P waves, QRS complexes and T waves, reflecting atrial contraction, ventricular contraction and ventricular repolarization, respectively. Four working electrodes allowed for 4-lead ECG signal acquisition with improved spatial and temporal resolutions. Variations in the voltage amplitude among the four ECG signals reflected the different points of reference in electrode placement with respect to the cardiac conduction vector. As illustrated in Fig. 3.12, P-wave signals were more prominent in electrodes B, C and D than that of A because P wave reflects the electrical signals from the atrium and electrode A was connected to the atrium through the relative high-resistance myocardium. In the analysis of the ST segment, the placement of electrode D proximal to the injury region resulted in a notable ST depression. The electrodes distal to the injury region did not detect the injury current, and thus, did not exhibit ST-depression. Similar to the 12-lead ECG in humans, our 4-channel signal acquisition enabled detection of the specific regions where myocardial injury occurred for small animal models. In corollary, histology corroborated the region-specific injury currents.

Simultaneous 4-channel recording uncovered specific regions of injury currents with high spatial and temporal resolution. Surface ECG data from all four electrodes revealed synchronization in ECG intervals (Fig. 3.12). The histology of injured myocardium (Fig. 3.12(a)) corroborated the region-specific ECG signals. In this context, the SNR of our surface MEA is dependent on the placement of individual electrodes. In reference to detecting region-specific injury currents with high spatial resolution, the placement of an electrode proximal to the injury region results in detecting ST depression. The electrodes distal to the injury region will not exhibit ST-depression. This electrophysiological phenomenon is in line with that of human surface ECG.

3.2.6 Conclusion

The multi-channel microelectrode membrane detected the region-specific ECG signals with high spatial and temporal resolution in the cryo-injured zebrafish hearts. The wearable microelectrode membrane remained functional in aquatic conditions, achieving a technical advance for long-term signal acquisition.

Engineering challenges have been addressed, including the use of high-density small-dimension microelectrodes to match the Young's modulus between the flexible membrane and the fish for long-term compatibility, and to obtain high SNR from the dynamic hearts. An optimal electrode dimension of 300 μm in diameter has been developed for optimal SNR with the current electrodes placement configuration.

The microelectrode membrane also demonstrated the feasibility of long-term electrophysiological monitoring. The minimally invasive approach enables epicardial ECG acquisition over a prolonged period.

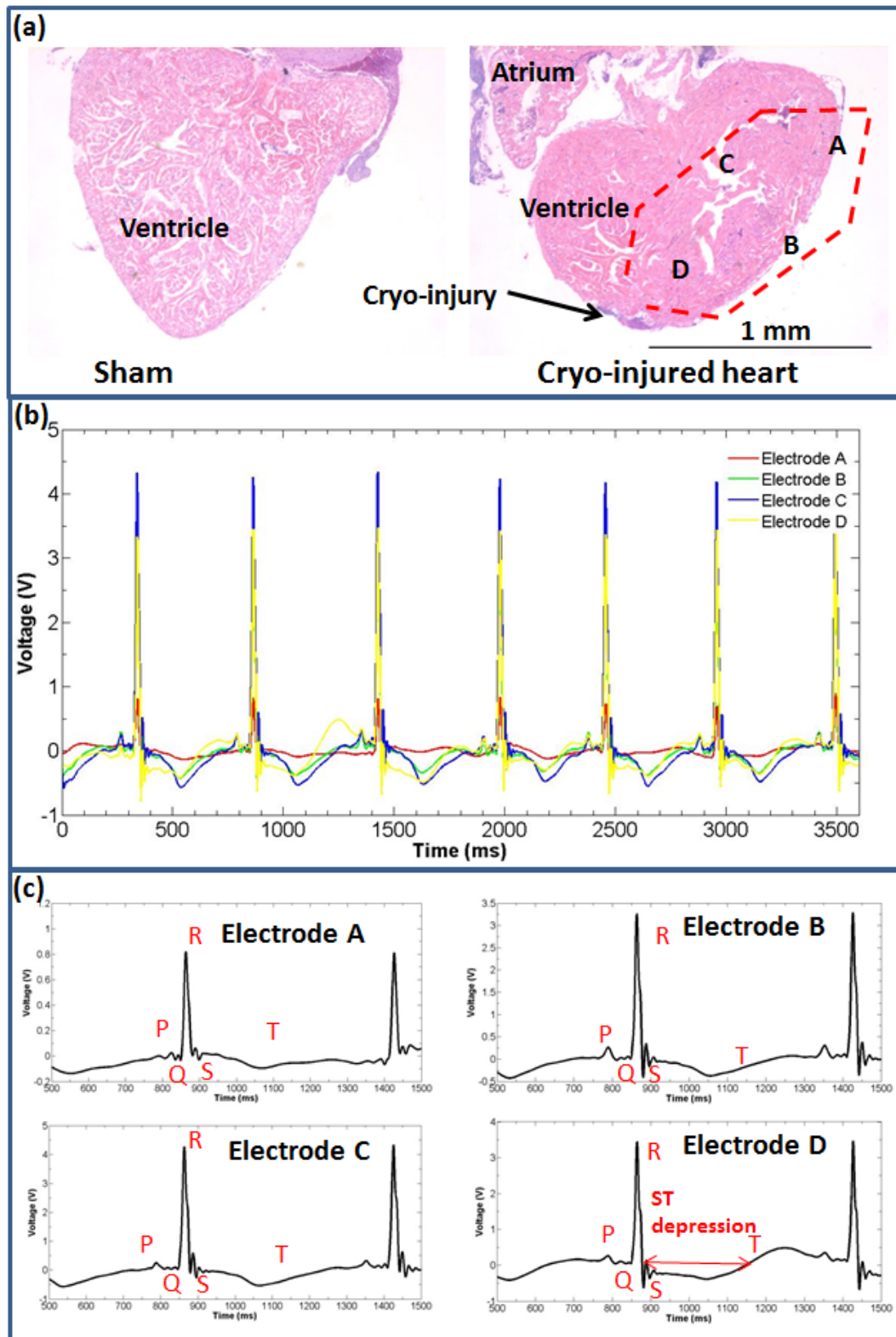


Figure 3.15. Simultaneous four-channel ECG recordings. (a) Histological slides showing the evidence of cryo-injury. Simultaneous four-channel ECG signals were acquired. The implanted MEA membrane captured a region of myocardial injury otherwise undetected via the single electrode lead. (b) 4 channels were recorded simultaneously showing the synchronization in ECG intervals. (c) Electrode A revealed P, QRS, and T morphology without evidence of myocardial injury currents. Electrodes B, C and D (most obvious) uncovered a region of myocardium where cryo-injury induced ST depression.

3.3 Wireless ECG Recording Backpack

The previous microelectrode membrane is long-term wearable, but electrical connections need to be made for every measurement. Accordingly, animals need to be pharmacologically sedated. However, this approach influenced the intrinsic cardiac pacemaker cells resulting in atrial arrhythmia and heart rate reduction. In this section, a wireless ECG recording system to process the ECG signals sensed by the microelectrodes was designed and prototyped on a printed circuit board. The completed system includes modules for (i) wireless power supply through resonant inductive coupling, (ii) low-noise amplification and filtering of ECG signals, and (iii) amplitude-modulated infrared light emitting diode (IRLED) transmission of measured data.

Through genetic fate mapping, Porrello *et al.* recently discovered the transient regenerating capacity of 1-day-old neonatal mice after birth, but this capacity is lost by 7 days of age [19]. Thus, the wireless and continuous operation of the microelectrode membrane was demonstrated on the non-sedated 1-day-old neonatal mouse model of heart regeneration.

3.3.1 Design

3.3.1.1 The wireless ECG Recording Microelectrodes: Linearly-Arranged Dry-Contact Chest Microelectrodes

In a 12-lead human ECG, six pads are linearly placed against the chest with conductive gel. By analogy to that, four recording microelectrodes are linearly arranged and placed on the neonatal mouse chest surface, but without any gel or adhesive. The titanium/gold microelectrodes are embedded in parylene-C membrane and selectively exposed at recording sites. An anchor is monolithically microfabricated adjacent to the recording microelectrodes for fixing the membrane against recording sites with surgical glue. The membranes are thermally annealed in a high-temperature vacuum oven to better match the chest curvature. The meandrous parylene C stripes were pre-coated with silicone to further secure the membrane to the chest surface with adequate accommodation for neonatal mouse size increase during heart regeneration.

Dry-contact electrodes provide convenience and animal comfort for long-term continuous recording, but they are more prone to electrical noise and mechanical movement [20]. Here, strategies to enhance the signal-to-noise ratios (SNR) were developed at three different levels: sensor, system and algorithm. (i) At the sensor level, mechanical anchors and fixations were incorporated for positioning the electrodes on the anatomic regions. In response to the neonatal growth during heart generation, the expandability of the fixation was capable of adapting to the increase in size. (ii) At the system level, the post-processing circuitry was implemented with high input-impedance and low input-noise to compensate for the high interface impedance and noise level associated with the dry-contact electrodes. (iii) At the algorithm level, wavelet analysis

and noise-reduction techniques previously described further increased the SNR at the receiver side.

3.3.1.2 The Wireless ECG Recording System: Amplification, Filtering and Optical Data Transmission

The purpose of amplification and filtering is to measure the small-amplitude ECG differential signal amidst the large common-mode and differential noise. The signal processing and wireless communication circuitry prototyped on the printed circuit board includes two-stage amplification, band-pass filtering, inductive power transfer, and optical data transmission (Fig. 3.13).

3.3.1.3 Solenoid Resonant Inductive Coupling

Resonant inductive coupling instead of use of a battery is implemented to support the prolonged recording as described in Chapter 1. Typically, resonant inductive coupling is manifested in a planar configuration with the receiver implanted. For analysis of the size and swimming activity of zebrafish, a solenoid configuration is chosen.

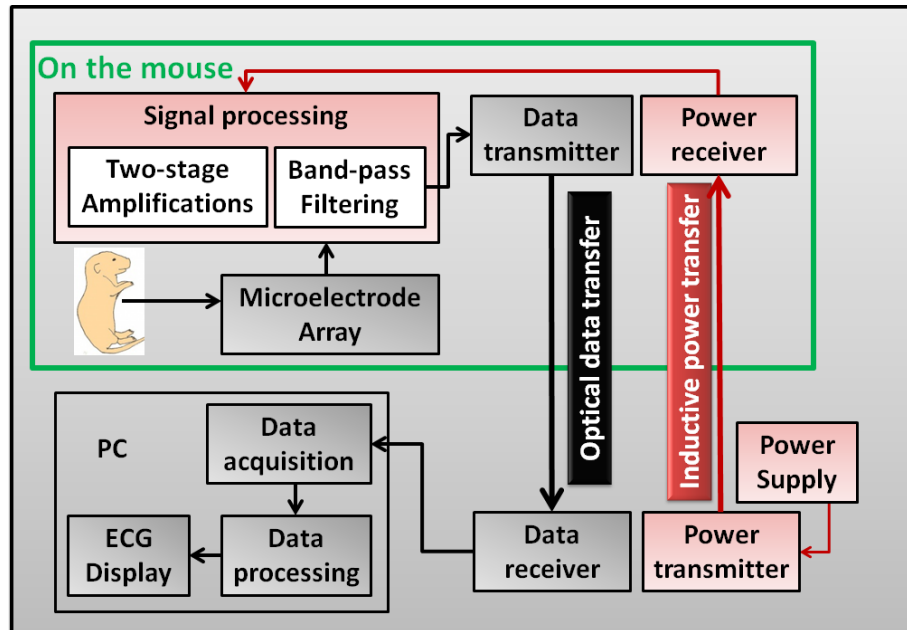


Figure 3.16. Block diagram of the wireless ECG system.

3.3.2 Implementation and Characterization

3.3.2.1 The Wireless ECG Recording Microelectrodes: Microfabrication

The microelectrode membrane was manufactured using micromachining techniques. Titanium/Gold electrodes sandwiched between two layers of parylene C were exposed to oxygen plasma etching at the recording sites and connecting pads. Four gold electrodes with a diameter of 200 μm were linearly arranged. The reference electrode was placed 5 mm away from the recording electrodes. There were four connecting pads assembled to a customized zero-insertion-force (ZIF) cable end by conductive epoxy and encapsulated by biocompatible silicone. The membrane measured $\sim 10 \mu\text{m}$ in thickness and the weight was less than 0.5 mg. After an annealing process in the vacuum oven at 200°C for two days, the membrane was curved to conform to the surface curvature of the neonate chests.

For long-term safety and comfort to the neonates, the dry-contact electrodes operated in the absence of conductive gel. The impedance at the skin-electrode interface was modeled as a resistor in series with a combination of parallel resistor-capacitor as previously discussed. At a frequency range of 2 Hz to 125 Hz, which is the interested frequency range of interest for ECG characteristics, the model was simplified to an interface capacitor.

Low-power oxygen plasma was applied to roughen the microelectrode surface, allowing for an increase in the effective contact area and a decrease in the interface impedance while still maintaining a high spatial resolution. The introduction of a first-stage amplifier with high input impedance rendered the microelectrode interface impedance negligible. As a result of the thin layer of micro-fabricated metal cables ($0.2\text{ }\mu\text{m}$ in thickness) running in parallel and being connected to the input-stage amplifier, the shunt capacitance was also negligible

The central portion of the microelectrode membrane was designed for securing to the abdomen along with the stretchable parylene C strips. The strips and sharp edges of the entire membrane were coated with a biocompatible silicone to match the Young's modulus of the animal skin. A mechanical mismatch would result in cell and tissue damage and possibly infection. In addition, a meshed parylene C pad adjacent to the microelectrodes served as an anchor (Fig. 3.14(b)). The applied surgical glue permeated throughout the distributed holes, providing contact between the parylene C embedded microelectrodes and the animal chest. This unique design minimized electrical signal fluctuations due to respiration-induced mechanical noise, and reduced the interface impedance of dry-contact electrodes.

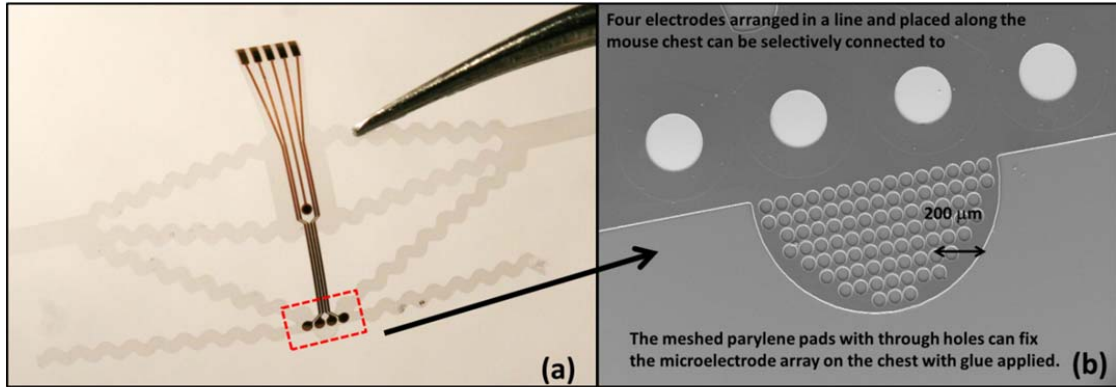


Figure 3.17. Fabricated device. (a) The manufactured microelectrode membrane with meshed parylene-C pad and meandrous strips. (b) The Scanning Electron Microscope (SEM) photo with four gold microelectrodes and the meshed parylene-C pad.

3.3.2.2 The Wireless ECG Recoding System: Printed Circuit Board

The signal amplification and filtering were critical to address the small chest-surface ECG signal strength ($< 150 \mu\text{V}$) and frequency range (2-125 Hz). The signal processing circuitry required two-stage amplifiers and a band-pass filter prior to transmitting the signals to the data receiver. The ECG signals were first passed through a first-stage instrumental amplifier (INA333 from Texas Instrument) to provide high input impedance, and then to an operational amplifier (OPA333 from Texas Instrument) to allow for a band-pass filter and secondary amplification. Signals with frequency below 2 Hz and above 125 Hz were filtered out by the high-pass and low-pass filters. The circuit communicated with the external data acquisition and process units via an Infrared Light Emitting Diode (IRLED). The circuit design highlighted the high-pass and low-pass filters in relation to the two-stage amplifiers (Fig. 3.15).

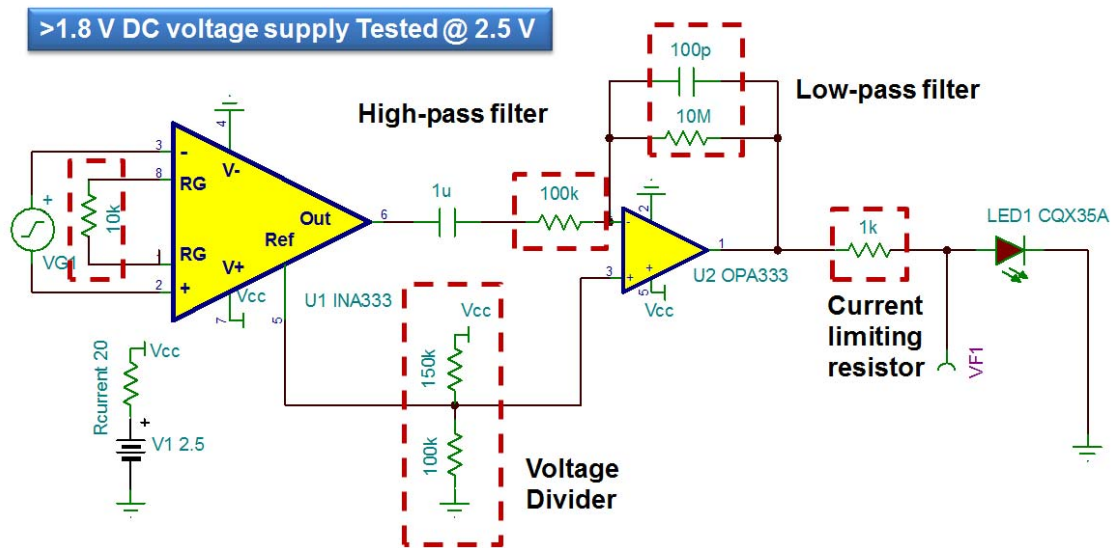


Figure 3.18. Circuit schematic of amplification, filtering and data transmission.

The frequency response up to 1 KHz was characterized (Fig. 3.16). Sinusoidal signals with frequencies ranging from 1Hz to 1KHz was applied to the input stage of the wireless ECG recording circuitry. The output was measured from the voltage on IRLED.

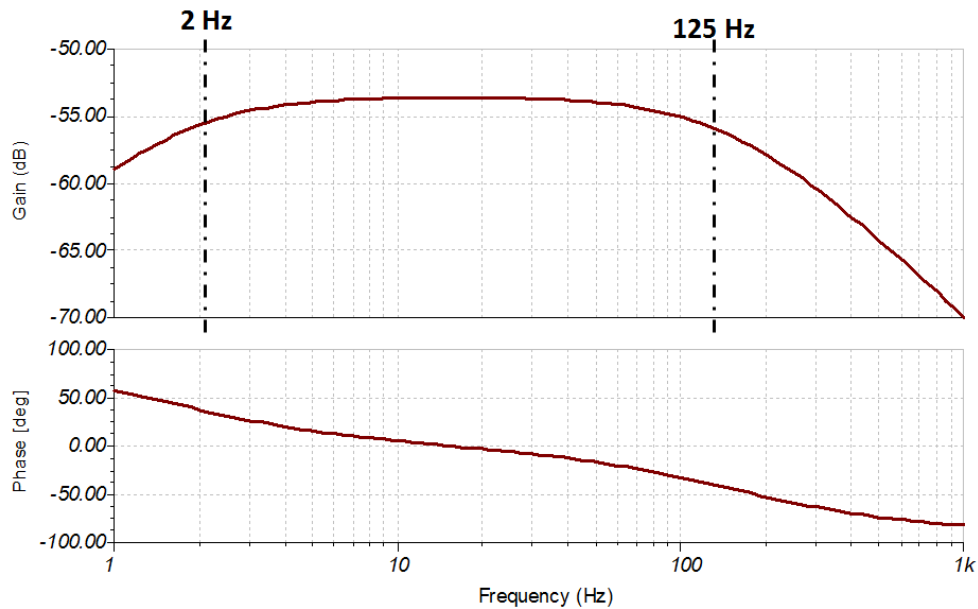


Figure 3.19. Frequency response of the wireless ECG system

3.3.2.3 Inductive Power Transfer: Hand-wound Coil

During operation of the system and the load, a DC voltage of 1.8 V or above and an average power of 300 μW was required. In this case, the equivalent load was calculated to be 20 k Ω . A two-coil inductive link coupled in a solenoid configuration was designed to provide power continuously (Fig. 3.17). A miniaturized and high-quality-factor receiver power coil was constructed by wrapping 30/48 Litz wires around a Ni/Zn ferrite core to establish high magnetic permeability and low electrical loss. The secondary coil had 8 turns, resulting in an outer diameter of 1.2 mm, an inner diameter of 0.7 mm, and a length of 4 mm. For the target frequency range, an inductance of 143 nH and a quality factor of 23.6 around 10 MHz were achieved.

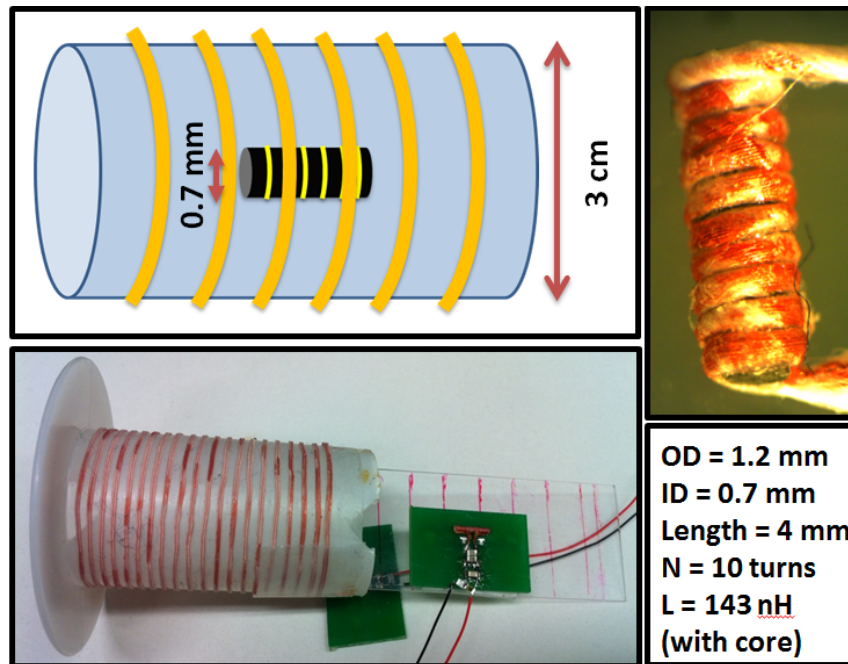


Figure 3.20. Inductive power transfer with hand-wound primary coil and secondary coil.

The overall power transfer efficiency was measured. A constant efficiency of 1.2% from 9-15 MHz was achieved (Fig. 3.18). In this context, the optimal operating frequency of 11.1 MHz was chosen.

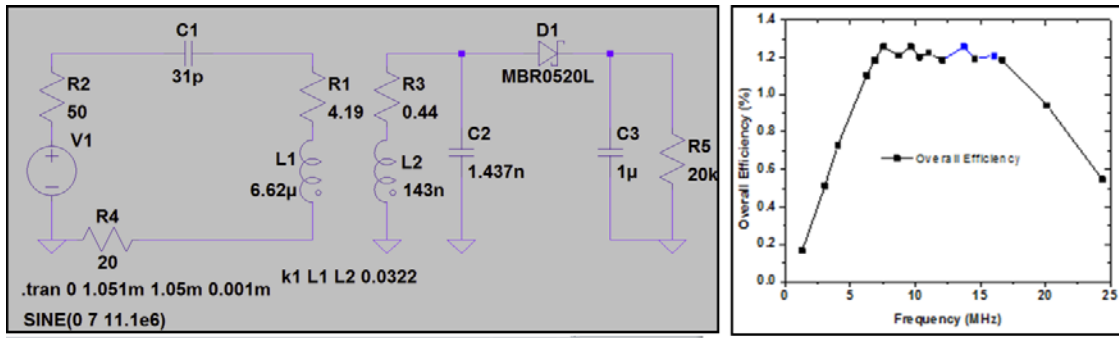


Figure 3.21. Overall power transfer efficiency of inductive coupling link.

The microelectrode membrane was inserted into the zero-insertion-force (ZIF) connector on the board (Fig. 3.19). Single-channel wireless ECG signal recording was established between one of the four front electrodes and the reference electrode.

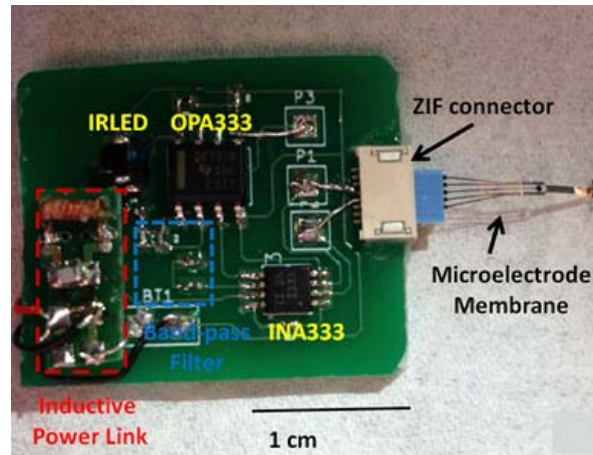


Figure 3.22. Wireless ECG recording system including the insertable microelectrode membrane and printed circuit board prototype.

3.3.3 ECG Recording from Neonatal Mouse

The wireless studies on the neonatal mice were performed in accordance with the Institutional Animal Care and Use Committees (IACUC) at Children Hospital Los Angeles, Los Angeles, CA, USA. The animal experiments were performed in compliance with the Guide for the Care and Use of Laboratory Animals of the National Institutes of Health.

For wireless ECG recording, neonatal mice aged between one to seven days old were positioned on a baseplate without sedation. The wireless ECG recording system was first gently fixed on the abdomen by thin strips of medical tape, followed by adhering the microelectrode membrane to the chest. Surgical glue (Dermabond Advanced™) was applied to the anchoring meshed pad and permeated through the holes. The mouse lying on baseplate was then placed inside the power-transmitting coil with a diameter of 2.8 cm. When the power was activated to the transmitting coil, real-time ECG signals were acquired (Fig. 3.20).

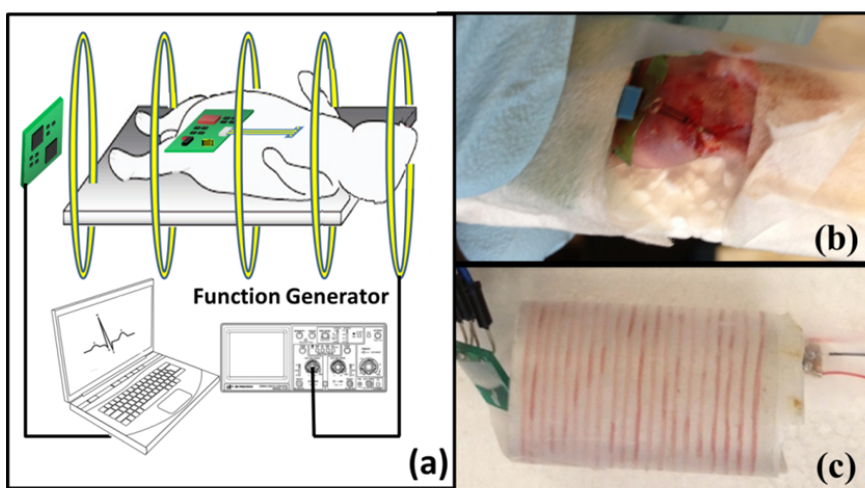


Figure 3.23. Wireless ECG recording from neonatal mouse. (a) The experiment setup of the wireless ECG recording. The neonatal mouse was positioned on the baseplate in enclosed by the transmitting coil. (b) The mouse with device on a baseplate (c) after insertion into the transmitter coil.

3.3.4 Results and Discussion

Reproducible trials on neonatal mice were performed to reveal distinct ECG signals in the presence and absence of pharmacological sedation. A comparison in ECG signals between the non-sedated and sedated conditions highlighted the distinct heart rates and ECG repolarization patterns (Fig. 3.21(a)). A reduction in the heart rates by 50% was noted in the presence of sedation (80 $\mu\text{g}/\text{gr}$ body weight Ketamine/xylazine). With the mechanical interference during recording and the signal attenuation during transmission, the P waves, QRS complexes and T waves remained distinct despite a reduction in SNR without sedation (Fig. 3.21(b)).

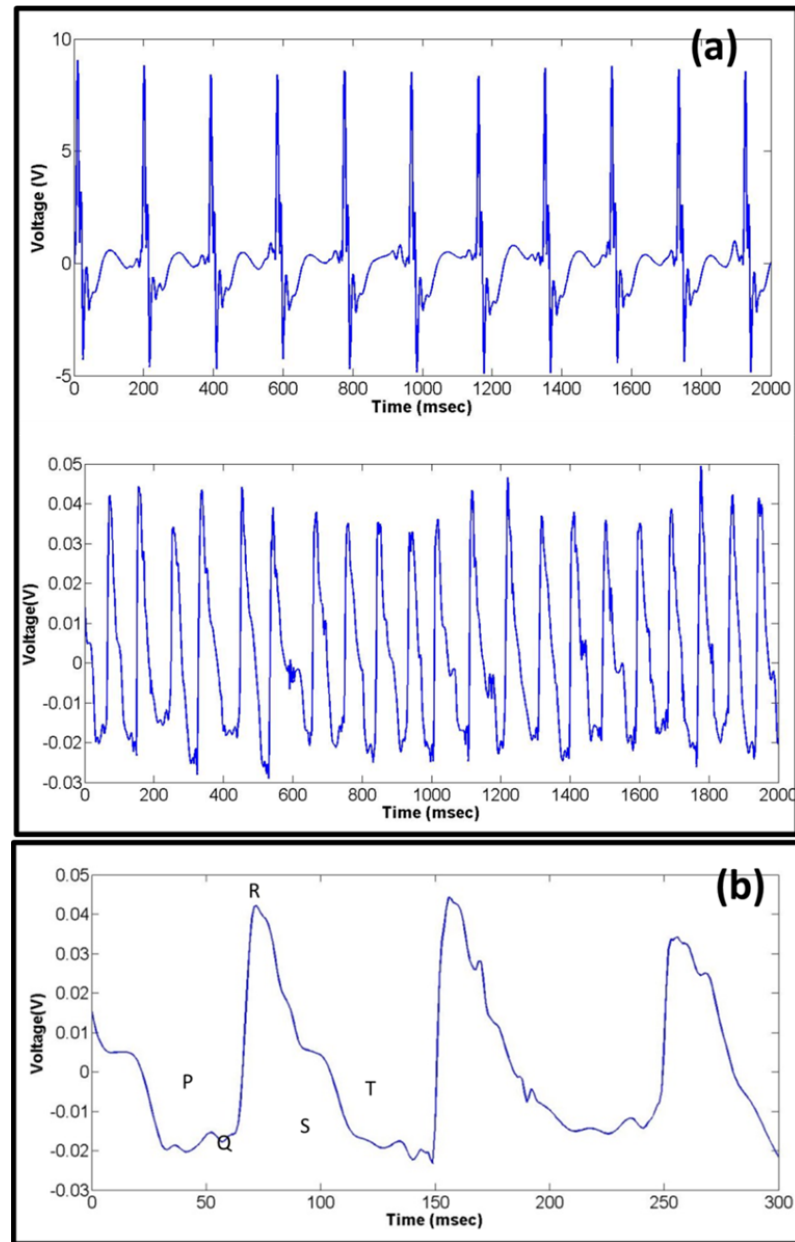


Figure 3.24. (a) A comparison of ECG signals between the sedated and non-sedated conditions. Heart rates are ~300 rpm and ~600 rpm for the sedated and non-sedated mice, respectively. (b) A representative signal-processed ECG tracing revealing the P wave, QRS complex and T wave.

3.3.5 Conclusion

For the first time, ECG signals have been continuously obtained from a one-day-old mouse model of heart regeneration, in the absence of pharmacological interference, with the intrinsic heart rates. The wearable and wireless-operated microelectrode membrane has been designed and demonstrated to enable continuous monitoring of cardiac rhythms for prolonged intervals. The membrane's conformity to the non-planar recording surface and the long-term expandability to the increase in size of the animals provided numerous translational implications for long-term *in-situ* detection of aberrant electrical activities for cardiac and neurological drug screening, disease and trauma modeling, and toxicity studies.

3.4 Flexible ECG Printed Circuit Membrane

In this section, the parylene C-based flexible printed circuit membrane was developed as a flexible and miniaturized counterpart of the printed circuit board (PCB). The strategies of circuit design and component assembly were formulated. The same wireless ECG recording system was implemented on the parylene C-based printed circuit membrane with integrated circuit bare dies and discrete components assembled. The sensing electrodes were monolithically fabricated with printed circuit membrane. The size and weight have been tremendously reduced with the circuit presenting the same functionality and performance

3.4.1 Design

3.4.1.1 Size and Weight Constraints




Zebrafish measure 3-4 cm in length. A wearable parylene C jacket has been previously demonstrated which provided a reference size for the implant design. Ideally, all the components should be within the domain of the jacket which is roughly 2 mm in width and 15 mm in length.

A zebrafish load test was carried out to identify the upper-limit weight that an adult zebrafish can carry during normal swimming. 50 mg was found to be a maximal comfortable load weight.

The wireless ECG recording circuit was previously prototyped on the printed circuit board with functional modules of signal processing, wireless data transmission and wireless power transfer. To substantially reduce the size and weight, two strategies were adopted: (i) The rigid printed circuit board was replaced by a thin-film parylene-C printed circuit membrane with embedded thin-film metal routings. (ii) All the chips were replaced by bare dies that are the same chips without packages. In addition, small packages of the discrete components were chosen.

Table 3.2 summarizes all the components with individual length, width, height and weight. Components add up to 25 mg. Taking into consideration the weight of the printed circuit membrane and necessary packaging coatings for underwater functioning, the total weight will probably be close to the weight upper limit.

Table 3.2. Component list with length, width, height and weight.

		Length (mm)	Width (mm)	Height (mm)	Weight (mg)
INA333		1.75	1.44	0.74	4.3
OPA333		0.98	0.81	0.27	0.2
IR LED		1.6	0.8	0.75	1.5
DIODE SHOTTKY		1.04	0.62	0.54	0.8
4 CAP (0201)		0.64	0.32	0.34	0
6 RES (0201)		0.61	0.31	0.23	0
PAC PCB		10	2	0.015	0.3
Unshielded coil		2	1.6	1.6	18.4
Total					25 mg

It is worth mentioning that the original hand-wound power receiver coil was replaced by an off-the-shelf wire-wound unshielded coil (Fig. 3.22). According to the datasheet, the coil has an inductance of 1 μH and a quality factor of 30 minimum at 7.96 MHz, and is therefore qualified for the inductive power transmission. Compared to previous hand-wound coil, this one has similar performance, but its package provides convenience for integration.

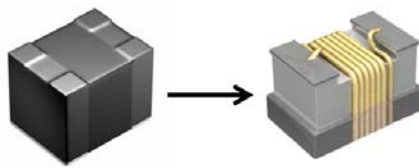


Figure 3.25. Off-the-shelf wirewound unshielded coil for general use in inductive coupling.

3.4.1.2 The Design of the Parylene C-Based Printed Circuit Membrane

The printed circuit membrane is constructed of a patterned thin metal layer embedded in between two parylene C layers and selectively exposed where electrical connections need to be made. The metal layer pattern is equivalent to the interconnecting layout design of the printed circuit board (PCB). In the first parylene C printed circuit membrane layout (Fig. 3.23), the four modules of signal sensing, signal processing, wireless data transmission and wireless power transfer are linearly arranged from left to right. The thin strip measures 2 mm in width. The head with signal sensing microelectrodes are percutaneously implanted into the heart as described previously. The Vcc and GND are distributed on the two sides of the layout.

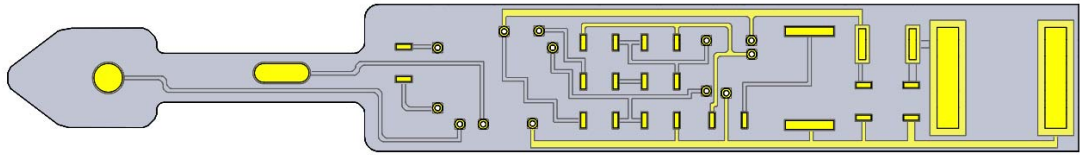


Figure 3.26. Circuit routing with all the necessary interconnections and pads.

The first layout design includes all the necessary interconnections and pads. While in the prototyping stage, additional debugging routings and pads are usually added to facilitate debugging. For the parylene printed circuit membrane, debugging pads and routings are even more necessary for two reasons: (i). Metal layers are embedded under the top parylene C layer and exposed pads are covered after being connected with

components. Thus probing cannot access to all the nets. (ii). The circuit membrane with components assembled is very delicate and tends to not take a lot of mechanical stretching during probing. Debugging pads and routings can take up extra space, which is not acceptable with the extreme size constraint. Therefore, tear-off debugging pads are added to the original circuit design (Fig. 3.24). After the debugging, those pads can be detached from the central circuit membrane. The schematic diagram of the print circuit membrane with all the components assembled is shown (Fig. 3.25).

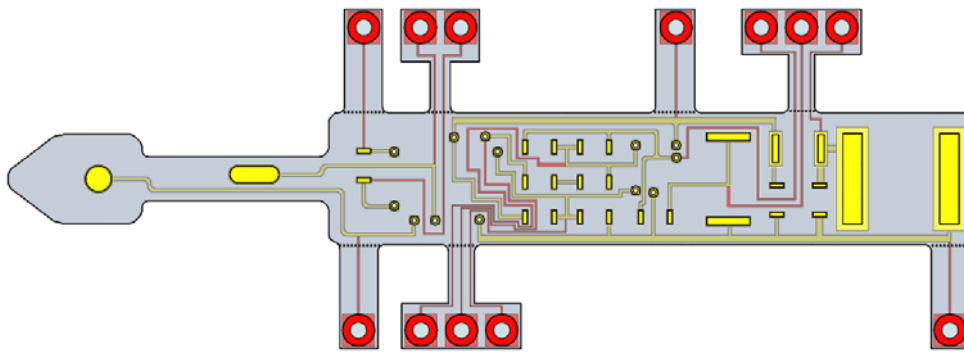


Figure 3.27. Printed circuit membrane design with debugging routings and tear-off debugging pads highlighted in red.

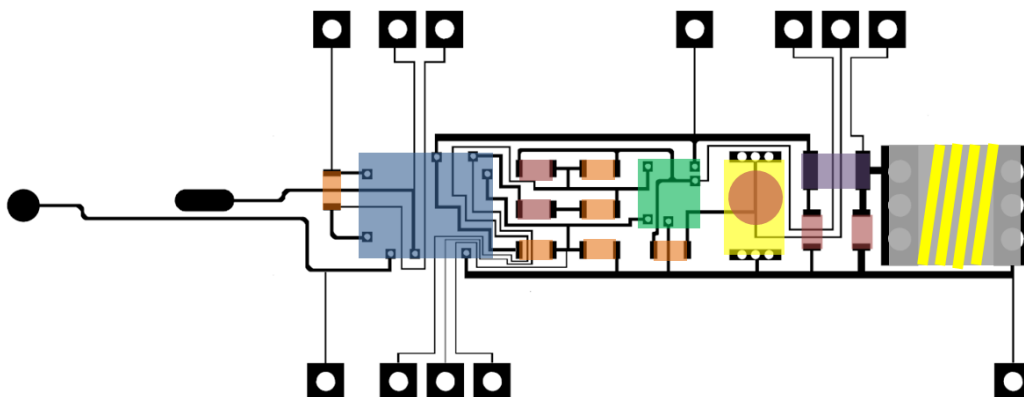


Figure 3.28. Schematic diagram of the print circuit membrane with all the components assembled.

Parylene does not withstand high temperature soldering. All the connections need to be made manually by conductive epoxy. The connections made through conductive epoxy, once fully cured, cannot be changed or removed. Therefore, in order to increase the overall yield, the one-piece circuit design is divided into three pieces (Fig. 3.26). Every individual sub-circuit has its own debugging routings and pads. These are called primary debugging pads (Fig. 3.27). Working sub-circuits can be combined through the connecting pads. The combined circuit can be debugged further more with secondary debugging pads and so on. There are non-conductive parylene pads on both sides designed to facilitate handling and alignment during combining.

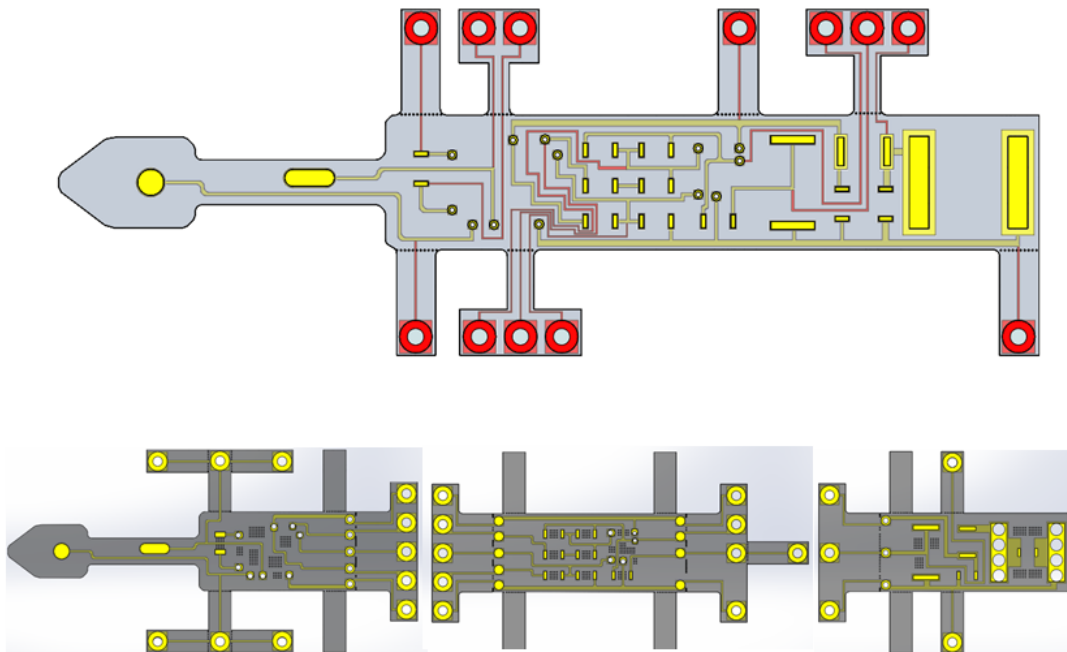


Figure 3.29. Comparison of one-piece circuit and three pieces of sub-circuits.

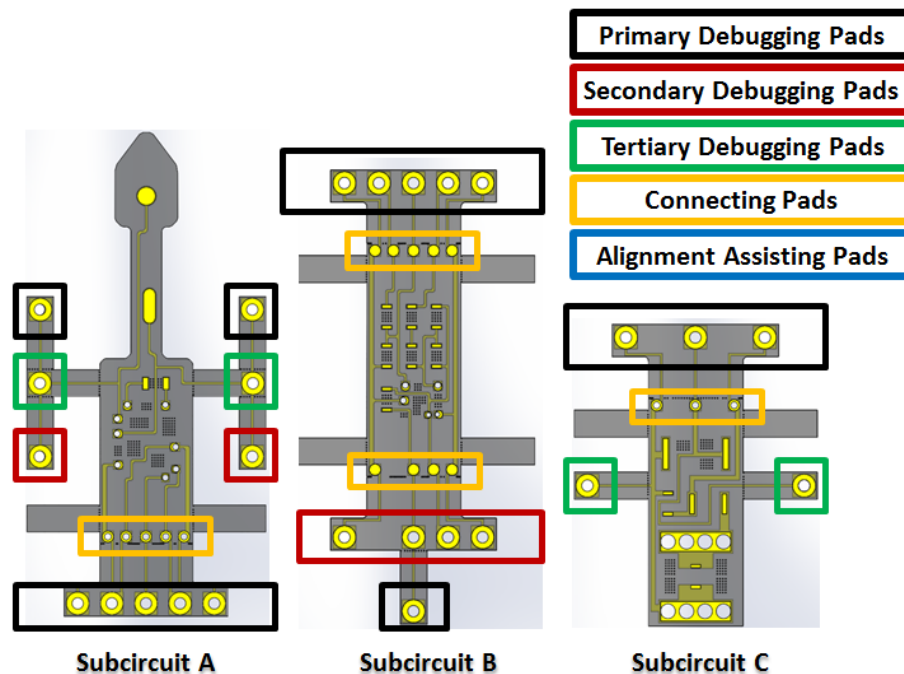


Figure 3.30. Design of three-level debugging pads, the connecting pads and the alignment assisting pads.

3.4.1.3 The Assembly Techniques of Discrete Components and IC Bare Dies

As mentioned before, parylene C doesn't stand up to high-temperature soldering. Wire bonding is not suitable either because the thin-metal layer on top of thin parylene film doesn't withstand the pressure during bonding. Therefore, conductive epoxy is used for connecting all the components.

For the discrete components with two pads on the sides, the assembly procedure is straightforward. Apply small drops of conductive epoxy right on top of the exposed metal pads on printed circuit membrane, align components with the pads, place them on top and

gently press down. To enhance the yield, the pads of the discrete components should be refreshed by heating with a soldering iron.

For the IC bare dies, a combined assembly technique is used (Fig. 3.28). The pads on bare dies are measured $75\text{ }\mu\text{m}$ by $75\text{ }\mu\text{m}$. Through holes are made on printed circuit membrane in accordance with the dimensions and arrangements of the bare die pads. Regarding the through holes, they should have larger openings on the top parylene than that on the metal and bottom parylene. To make the connections, the bare die is first placed underneath the printed circuit membrane. There are non-conductive through-holes around the connecting through-holes to mechanically hold the bare dies with the membrane. After aligning the connecting through-holes with the pads on bare die, silicone is first applied around the non-conductive through holes. After curing the silicone, the assembly of the membrane and bare die is fixed onto a substrate printed circuit board with water-soluble wax. Electrical connections can be made directly by applying conductive epoxy and connecting the ring-like embedded metal with bare die pads. However, the bare dies utilized have aluminum pads and there generally exists a thin-layer of oxide. To build a reliable electrical connection, the pads are first wire bonded to peripheral pads on the substrate printed circuit board. The gold bonding wires are electrically connected to the pads. Because the gold doesn't get oxidized, conductive epoxy is applied around the gold bonding wire to connect the bonding wire with the embedded metal in the membrane. With the conductive epoxy fully cured, the bonding wire not buried inside the conductive epoxy drop can be cut off. Thus, this assembly procedure provides both electrical and mechanical reliability.

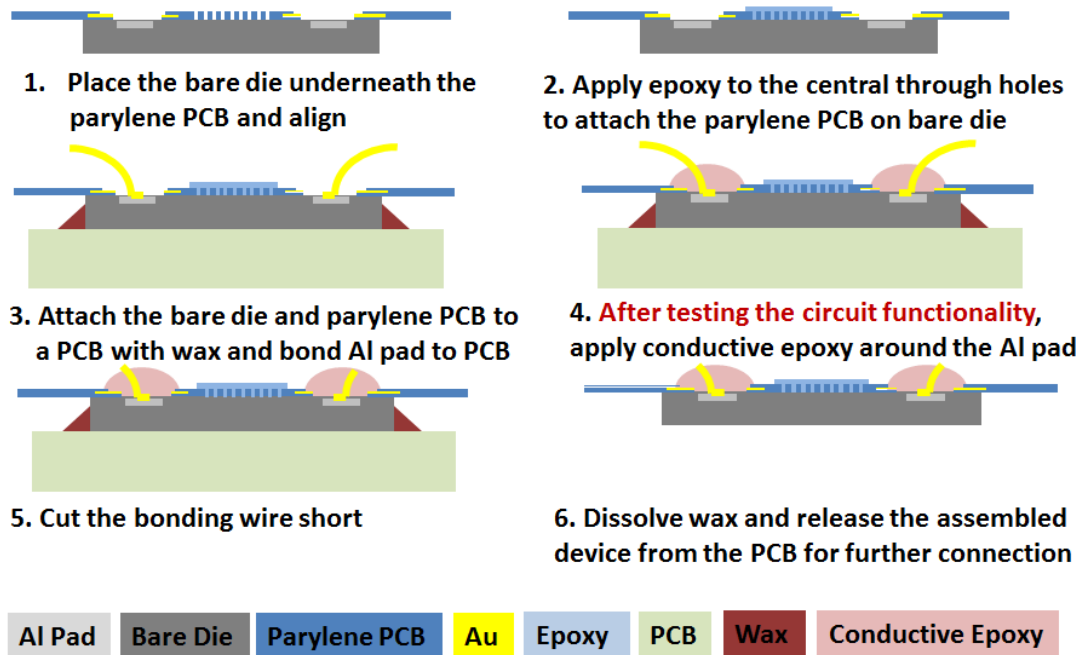


Figure 3.31. Cross-sectional view of the bare die assemble.

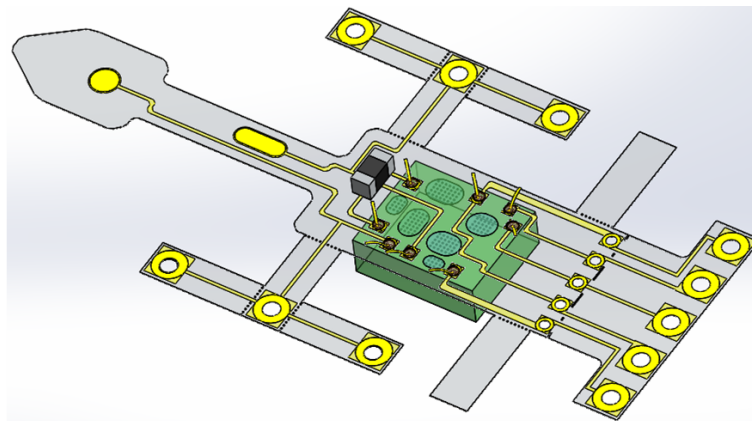


Figure 3.32. 3D drawing of the assembled bare die and discrete resistor.

3.4.1.4 The Assembly and Debugging Procedure

The step-by-step assembly and debugging procedure is illustrated here in detail.

- (1) The printed circuit membrane and the sensing microelectrodes are microfabricated in the same process. The process is same as the previously described parylene-metal-parylene sandwich structure with metal exposed at where electrical connections need to be made.

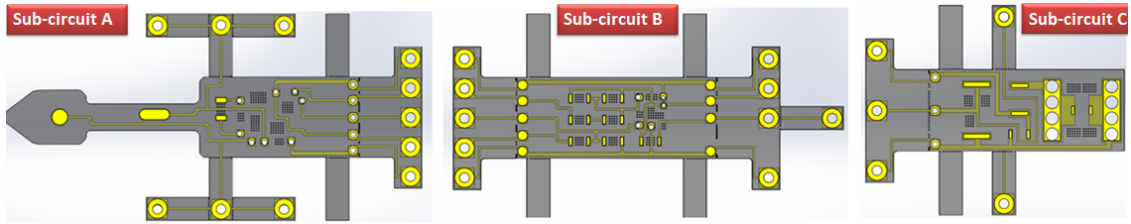


Figure 3.33. Printed circuit membranes of three sub-circuits.

- (2) The discrete components are assembled onto sub-circuits. The connections are checked by probing.

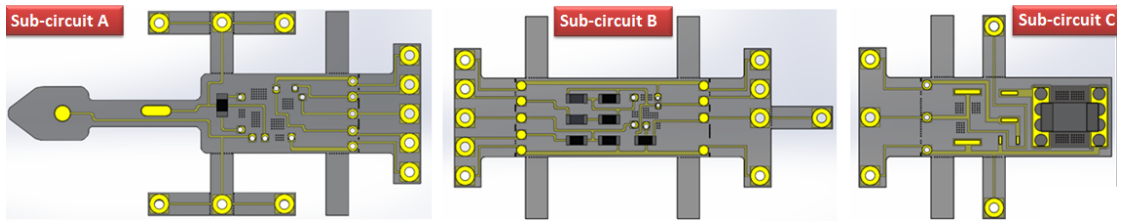


Figure 3.34. Three sub-circuits with discrete components assembled.

The sub-circuit C has an inductor and a capacitor connected in parallel. The quality factor of the resonator is tested to ensure low contact resistances between the resistor and capacitor.

- (3) The bare dies are assembled onto sub-circuit A and sub-circuit B respectively.

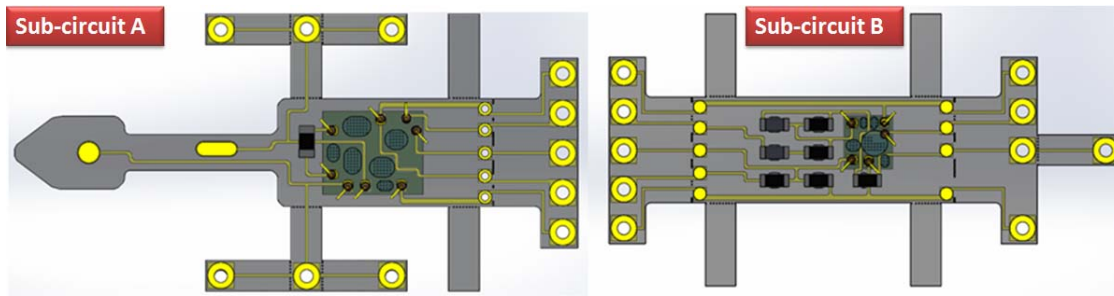


Figure 3.35. Sub-circuit A and sub-circuit B with bare dies assembled.

- (4) Assembled sub-circuit A and sub-circuit B are connected to debugging printed circuit boards with the primary debugging pads. The functionalities of the two sub-circuits are tested with the assistance of the external circuitry. Then the tear-off primary debugging pads can be removed from the working sub-circuits.

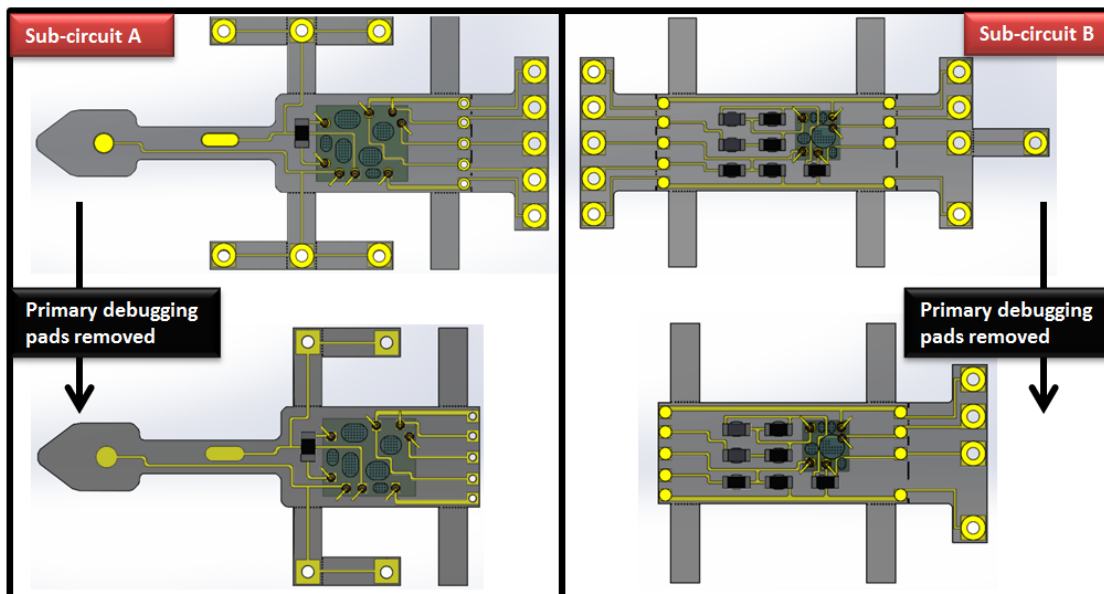


Figure 3.36. Sub-circuit A and sub-circuit B before and after removing primary debugging pads.

- (5) After debugging and removing the debugging pads of sub-circuit A and sub-circuit B, they are connected together.
- (6) Assembled sub-circuit A+B is connected to a debugging printed circuit board with the secondary debugging pads. The functionality of the sub-circuit A+B is tested with the assistance of the external circuitry. The tear-off secondary debugging pads can be removed from the working sub-circuits.

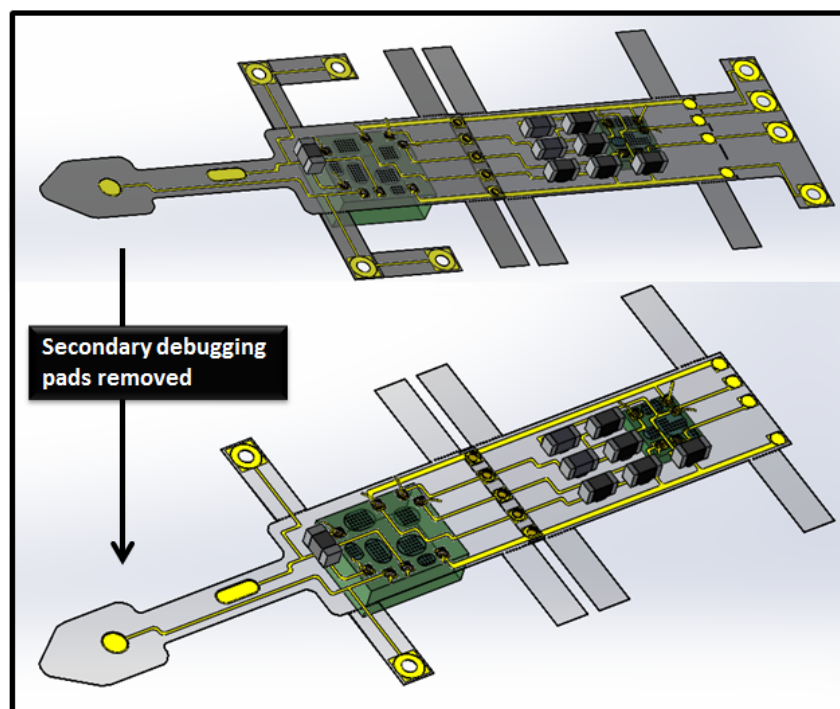


Figure 3.37. Sub-circuit A+B before and after secondary debugging pads are removed.

- (7) The rest of the discrete components are assembled on sub-circuit C. The functionalities of sub-circuit C is tested with the assistance of the external circuitry. The tear-off primary debugging pads can be removed from the working sub-circuit C.

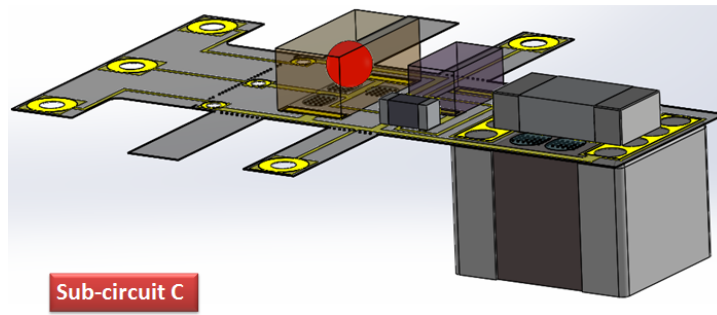


Figure 3.38. Sub-circuit C with all the discrete components assembled.

- (8) After debugging and detaching the debugging pads from sub-circuit C, sub-circuit A+B and sub-circuit C are connected together. The functionality of the sub-circuit A+B+C is tested with the assistance of the external circuitry. The tear-off tertiary debugging pads can be removed from the working circuit. Finally, the align assisting pads are finally removed as well.

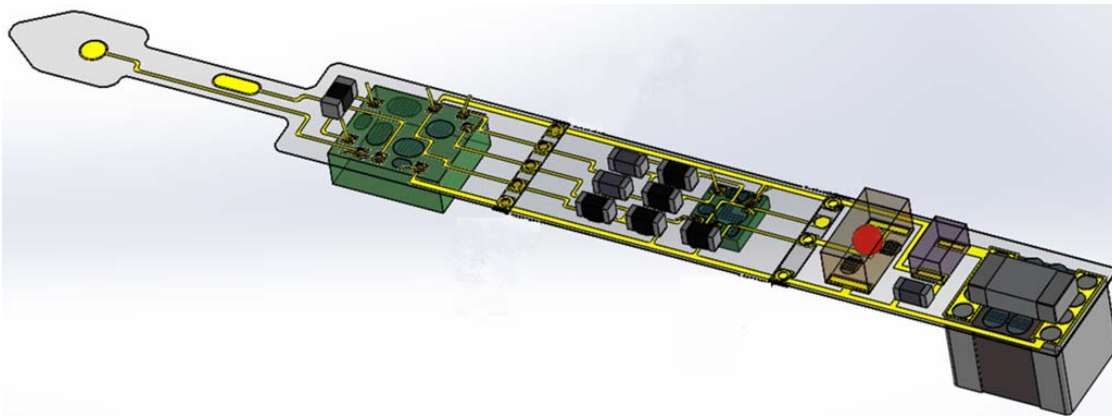


Figure 3.39. Final look of the complete wireless ECG system with sensing electrodes and all the electronic modules.

3.4.2 Fabrication and Characterization

3.4.2.1 The Microfabrication and Assembly of Three Sub-circuits

The microelectrodes and the printed circuit membranes were monolithically microfabricated in the same parylene-metal-parylene process. Before assembling the discrete components onto the sub-circuit membranes, the membranes were cleaned by a low-power oxygen plasma etching. Then discrete components and bared dies were assembled and checked following the order described in the design section (Fig. 3.37).

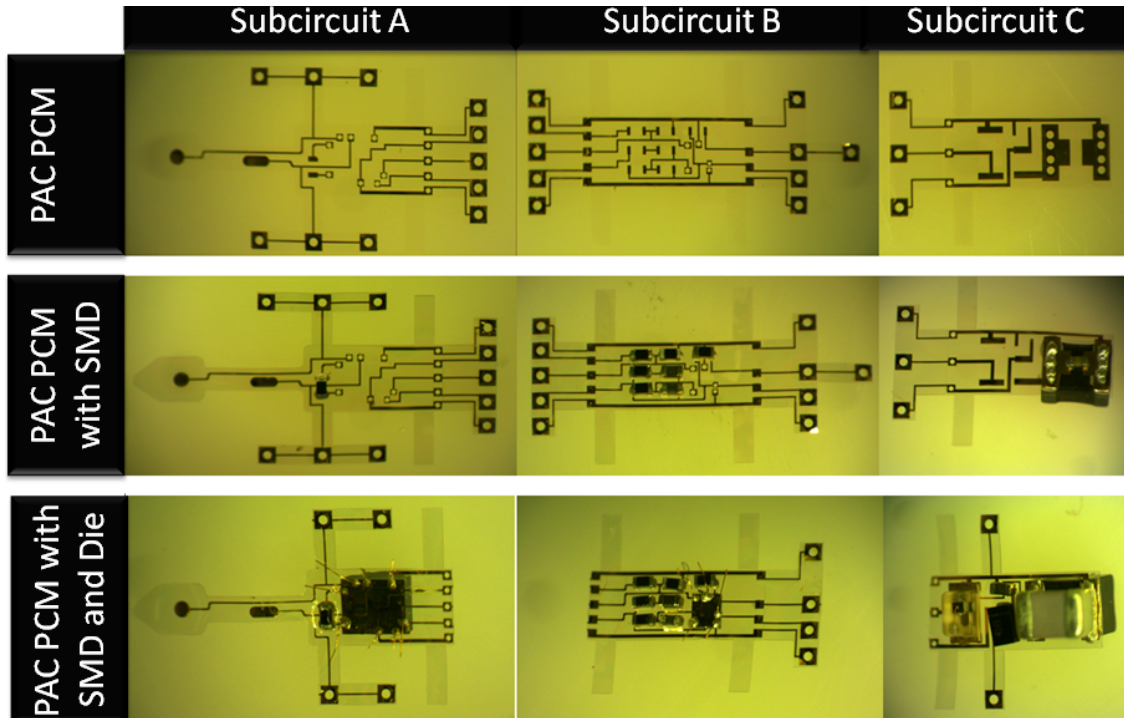


Figure 3.40. Microfabrication and assembly flow of the three sub-circuits.

3.4.2.2 The Characterization of Sub-circuits

The previous hand-wound power receiver coil has been replaced by off-the-shelf wire-wound unshielded coil. Therefore, the inductive coupling link was re-characterized

(Fig. 3.38). At an operation frequency of 10.8 MHz, the link provided power of 670 μW with a DC supply of 2.6 V, satisfying the power and voltage requirements of the signal processing and data transmission electronics.

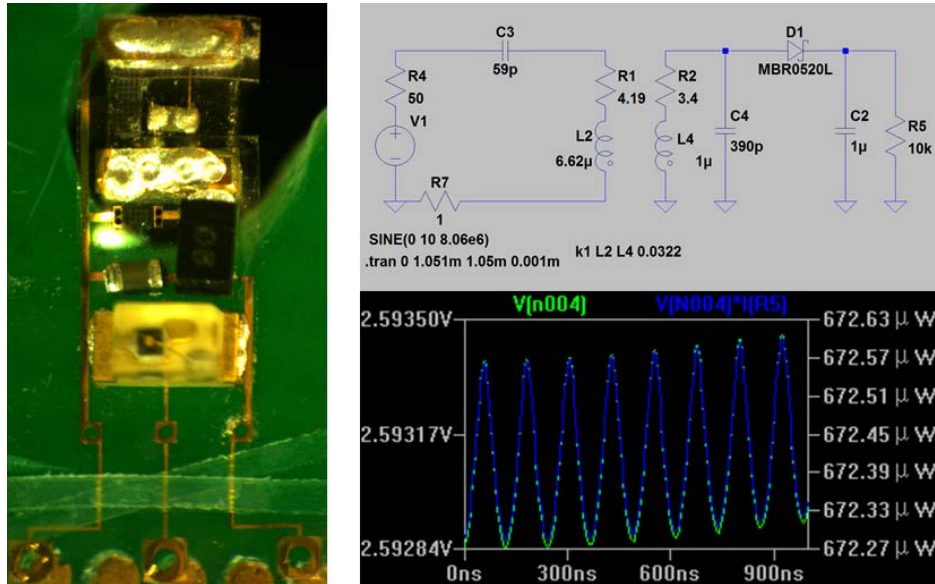


Figure 3.41. Assembled sub-circuit C and the power transfer efficiency testing.

Sub-circuit A and sub-circuit B were connected to debugging printed circuit boards with primary debugging pads. They were tested with external assisting circuitry.

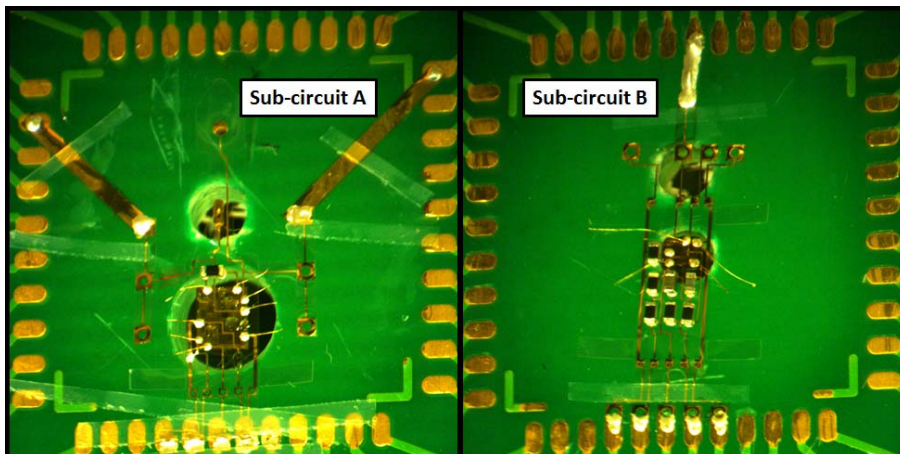


Figure 3.42. Sub-circuit A and sub-circuit B connected to debugging printed circuit boards with primary debugging pads.

Before removing the primary debugging pads and taking the sub-circuits from the debugging printed circuit boards, debugging printed circuit boards, with sub-circuit A and sub-circuit B, respectively, were connected using bread board. The recorded ECG signals from a bench-top ECG simulator were shown on the oscilloscope.

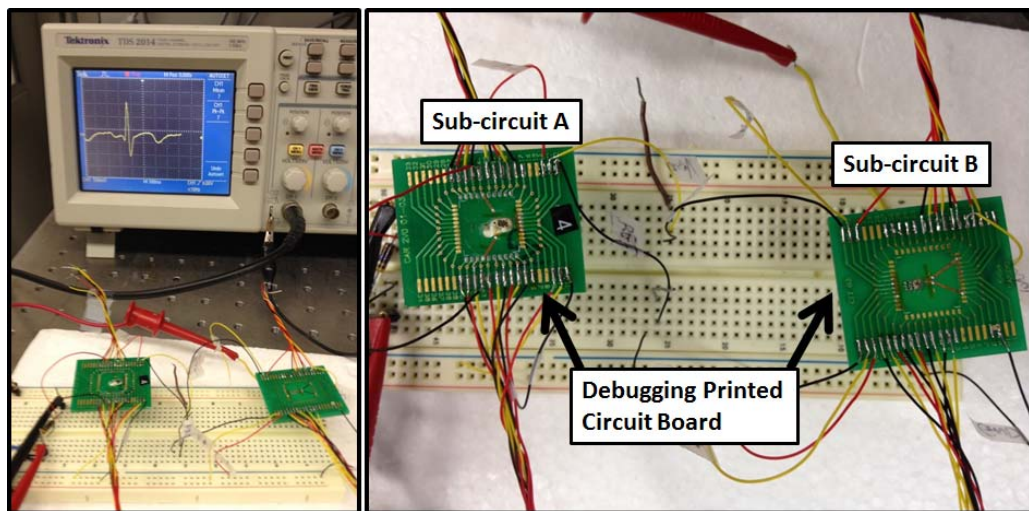


Figure 3.43. Sub-circuit A and sub-circuit B connected through bread board for testing.

After removing the primary debugging pads on sub-circuit A and sub-circuit B, these two sub-circuits were removed from the debugging printed circuit boards and connected using conductive epoxy.

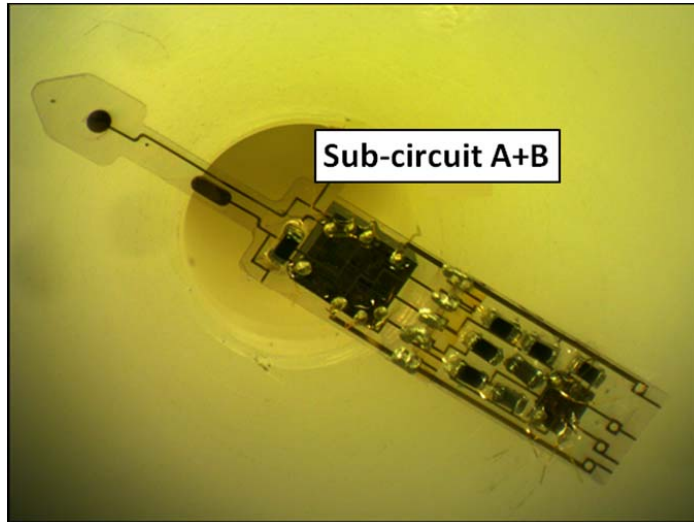


Figure 3.44. Assembled sub-circuit A+B.

After sub-circuit A+B was debugged, sub-circuit A+B was connected to sub-circuit C to form the sub-circuit A+B+C.

3.4.2.3 The Characterization of the Final Device

Sub-circuit A+B+C was connected onto the debugging printed circuit board with tertiary debugging pads. The inputs were from the bench-top ECG simulator. ECG signals were repeatedly recorded and the P waves, QRS complexes and T waves were all detected.

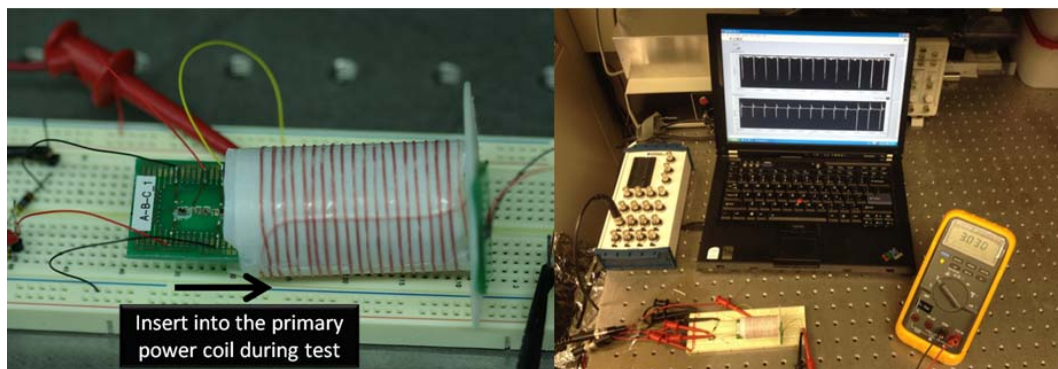


Figure 3.45. Testing platform of the wireless ECG recording system prototyped on parylene printed circuit membrane.

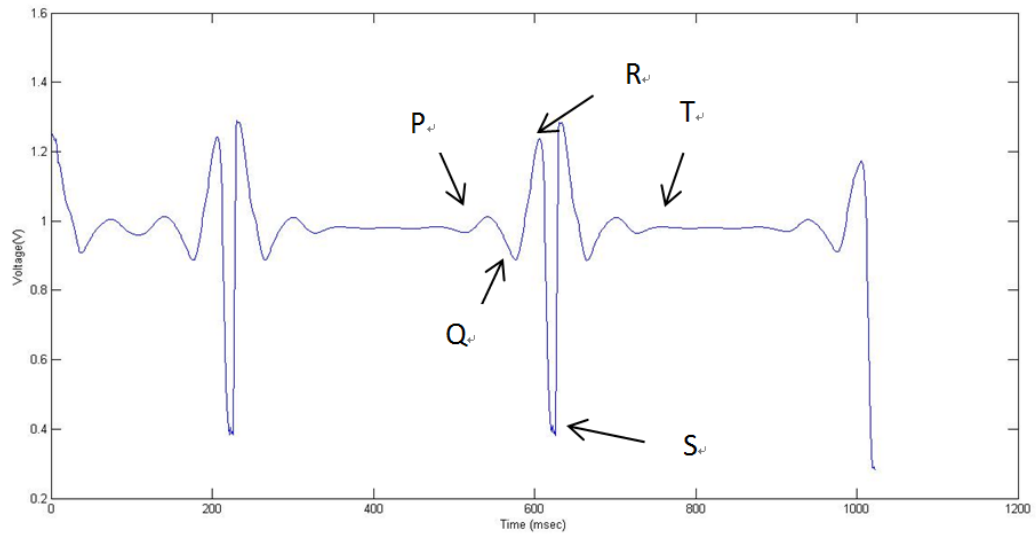


Figure 3.46. Recorded ECG signals from simulator on bench top

The final device measures 2 mm in width, about 16 mm in length and weighs about 35 mg. Compared to its counterpart prototyped on printed circuit board, the final device is flexible, light and compact.

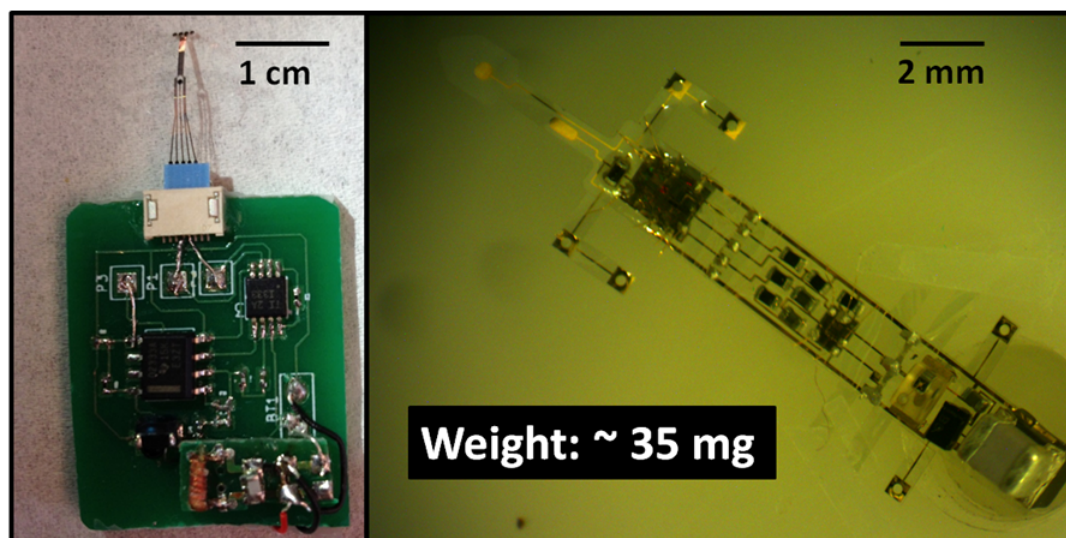


Figure 3.47. Comparison of the ECG wireless recording system prototyped on printed circuit board and on printed circuit membrane.

3.4.3 Discussion and Conclusion

The parylene C-based printed circuit membrane has achieved flexible, light-weight and compact integration of the wireless ECG recording system. The design of sub-circuits not only enhanced the overall yield, but also provided the possibility of 3D integration.

As in the zebrafish application, a 3D integration is needed. Based on our load test (Fig. 3.45), when the implant mockup aligned with the center of gravity of the zebrafish, the fish could carry the heaviest load (50 mg). This provided a reference for the special integration of the implant, which preferably spans 1.5-2.5 mm in width and 8.5 mm in length. Therefore, a design with three sub-circuits stacked and connected is superior to the current long strip with three sub-circuits lined up and connected.

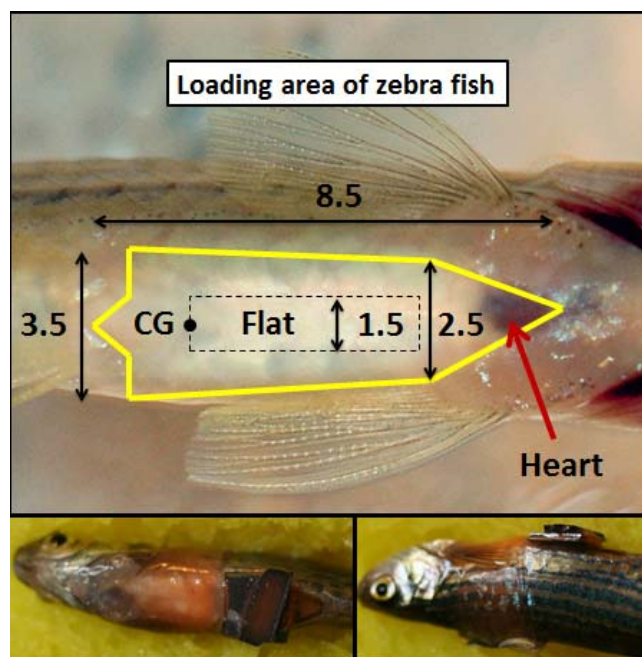


Figure 3.48. Loading area of zebrafish.

In addition, the second major challenge for zebrafish ECG monitoring is the long-term underwater packaging. A combination of parylene C, silicone and other polymers can potentially maintain the flexibility of the packaging, but may not be adequate for two-month underwater application. So a novel packing technique that can be long-term water resistant and mechanically match the Young's modulus of fish skin is needed.

3.5 Conclusion

The work in this chapter developed a long-term *in vivo* monitoring system. In the beginning, a passive microelectrode sensor carried by a long-term parylene C-based membrane was designed and fabricated. Multiple microelectrodes were percutaneously implanted onto the zebrafish heart surface. Region-specific aberrant cardiac currents of injured and regenerating hearts were recorded simultaneously in a prolonged interval,

which proved the feasibility and significance of applying ECG monitoring during heart regeneration. To enable continuous recording from non-sedated and non-restricted animals, the passive microelectrode sensor was demonstrated to operate wirelessly with a wireless ECG recording system prototyped on printed circuit board. ECG signals from non-sedated one-day-old neonatal mouse were wirelessly recorded. To further achieve zebrafish wireless ECG recording, a novel integration platform was developed to miniaturize the wireless ECG system. Parylene C-based printed circuit membranes provided a flexible, light weight and compact substrate for electrically interconnecting and mechanically carrying all the electronic parts.

3.6 References

- [1] J. L. Reeve, A. M. Duffy, T. O'Brien, and A. Samali, "Don't lose heart - therapeutic value of apoptosis prevention in the treatment of cardiovascular disease," *Journal of cellular and molecular medicine*, vol. 9, pp. 609-622, 2005.
- [2] C. Hahn and M. A. Schwartz, "The role of cellular adaptation to mechanical forces in atherosclerosis," *Arteriosclerosis, thrombosis, and vascular biology*, vol. 28, pp. 2101-2107, 2008.
- [3] K. D. Poss, L. G. Wilson, and M. T. Keating, "Heart regeneration in zebrafish," *Science*, vol. 298, pp. 2188-2190, 2002.
- [4] Á. Raya, A. Consiglio, Y. Kawakami, C. Rodriguez-Esteban, and J. C. Izpisua-Belmonte, "The zebrafish as a model of heart regeneration," *Cloning and stem cells*, vol. 6, pp. 345-351, 2004.
- [5] K. D. Poss, "Getting to the heart of regeneration in zebrafish," *Seminars in Cell & Developmental Biology*, vol. 18, pp. 36-45, Feb 2007.

- [6] A. M. Cobo, F. Yu, Y. Zhao, J. Gu, H. Cao, Y. C. Tai, *et al.*, "Implantable micro-Electrode Array for Long-term ECG Recording in Zebrafish," *Faseb Journal*, vol. 27, p. 1, Apr 2013.
- [7] A. S. Forouhar, J. R. Hove, C. Calvert, J. Flores, H. Jadvar, and M. Gharib, "Electrocardiographic characterization of embryonic zebrafish," *Conf Proc IEEE Eng Med Biol Soc*, vol. 5, pp. 3615-7, 2004.
- [8] D. Sedmera, M. Reckova, A. deAlmeida, M. Sedmerova, M. Biermann, J. Volejnik, *et al.*, "Functional and morphological evidence for a ventricular conduction system in zebrafish and *Xenopus* hearts," *Am J Physiol Heart Circ Physiol*, vol. 284, pp. H1152-60, Apr 2003.
- [9] A. Raya, A. Consiglio, Y. Kawakami, C. Rodriguez-Esteban, and J. C. Izpisua-Belmonte, "The zebrafish as a model of heart regeneration," *Cloning and Stem Cells*, vol. 6, pp. 345-351, Win 2004.
- [10] A. G. Kleber and Y. Rudy, "Basic mechanisms of cardiac impulse propagation and associated arrhythmias," *Physiological Reviews*, vol. 84, pp. 431-488, Apr 2004.
- [11] M. Ortiz-Catalan, R. Branemark, B. Hakansson, and J. Delbeke, "On the viability of implantable electrodes for the natural control of artificial limbs: Review and discussion," *Biomedical Engineering Online*, vol. 11, p. 24, Jun 2012.
- [12] M. Williams, J. Nurmi, and Ieee, *MULTIPURPOSE CHIP FOR PHYSIOLOGICAL MEASUREMENTS*. New York: I E E E, 1994.

- [13] Y.-T. Zhang, C. K. C. Lui, and B. L. Luk, "Wireless Biomedical Sensing," in *Wiley Encyclopedia of Biomedical Engineering*, ed: John Wiley & Sons, Inc., 2006.
- [14] T. Handa, S. Shoji, S. Ike, S. Takeda, and T. Sekiguchi, "A very low-power consumption wireless ECG monitoring system using body as a signal transmission medium," in *Solid State Sensors and Actuators, 1997. TRANSDUCERS '97 Chicago., 1997 International Conference on*, 1997, pp. 1003-1006 vol.2.
- [15] E. Monnet and J. C. Chachques, "Animal Models of Heart Failure: What Is New?," *The Annals of Thoracic Surgery*, vol. 79, pp. 1445-1453, 4// 2005.
- [16] F. Yu, R. Li, E. Parks, W. Takabe, and T. K. Hsiai, "Electrocardiogram signals to assess zebrafish heart regeneration: implication of long QT intervals," *Ann Biomed Eng*, vol. 38, pp. 2346-57, Jul 2010.
- [17] H. Pearson, "The regeneration gap," *Nature*, vol. 414, pp. 388-390, Nov 2001.
- [18] D. L. Mann, "Management of Heart Failure Patient with reduced ejection fraction in Bonow, Mann, Ziper, Libby, Braunwald's Heart Disease A Textbook of Cardiovascular Medicine," ed: Elsevier Saunders, 2012.
- [19] E. R. Porrello, A. I. Mahmoud, E. Simpson, J. A. Hill, J. A. Richardson, E. N. Olson, *et al.*, "Transient regenerative potential of the neonatal mouse heart," *Science*, vol. 331, pp. 1078-1080, 2011.
- [20] Y. M. Chi, J. Tzyy-Ping, and G. Cauwenberghs, "Dry-Contact and Noncontact Biopotential Electrodes: Methodological Review," *Biomedical Engineering, IEEE Reviews in*, vol. 3, pp. 106-119, 2010.

Chapter 4 Conclusion

The development of innovative microimplants for *in vivo* sensing usually starts with a biomedical or clinical challenge identified in clinical practice. A crucial step afterwards is how to design the implant by breaking down the sensing requirements into the function modules of hardware implementation as discussed in Chapter 1. After designing, implementing and characterizing each individual function module, the modules need to be put together and configured collectively to build up a system. Then, the system is tested on the bench top, with animals, and then later in clinical trials.

Despite the advances in diagnosis and therapy, atherosclerotic cardiovascular diseases still remain the leading causes of morbidity and mortality in developed countries. Predicting metabolically active atherosclerotic plaques has remained an unmet clinical need. The catheter-based impedance sensor with an inflatable balloon was developed to characterize the inflammatory states of high-risk unstable atherosclerotic plaques. The novel quasi-concentric microelectrode impedance sensor detected distinct electrochemical impedance spectroscopy (EIS) measurements for unstable atherosclerotic plaques that harbored active lipids and inflammatory cells. The inflatable balloon provided a well-controlled *in vivo* contact securing a proper contact with the plaques under test.

This study presents the use of a robust and innovative balloon catheter-based concentric EIS sensor for the detection of endoluminal electrochemical properties. The demonstrations with explants from fat-fed NZW rabbit aortas and carotid arteries, respectively, further corroborated the link between endoluminal properties and lipid-rich

plaques. While EIS is a sensitive approach to assess lipid-rich plaques, its specificity would be strengthened by integrating with ultrasound (IVUS). While the high-frequency IVUS (20-60 MHz) will enable us to resolve spatial resolution from 400 μm to 30 μm , the concentric bipolar microelectrode sensor will detect distinct endoluminal impedance spectra in the presence of high-fat versus normal diets [1, 2]. An integrated IUVS-EIS strategy will likely enhance the possibility of co-registration of ultrasound with the EIS measurements, and will detect an increase in EIS magnitude in non-obstructive plaques that occupy less than 20% of the luminal diameter, but harbor oxLDL and foam cells. Hence, integrating EIS with IVUS would improve both the sensitivity and specificity in identifying the metabolically active, but non-obstructive plaques [2].

On the other hand, a flexible microelectrode membrane was developed to monitor zebrafish electrocardiogram (ECG) during heart regeneration. In humans, myocardial infarction results in the irreversible loss of cardiomyocytes. Zebrafish hearts fully regenerate after resection or cryo-injury, without either scarring or arrhythmias. To study the cardiac regeneration, a passive long-term wearable membrane with multiple microelectrodes was first demonstrated to measure region-specific ECG signals from zebrafish in a prolonged period. Following that, the wireless and continuous operation of the microelectrode membrane was presented in order to allow recording from non-sedated animal models. Further miniaturization has even explored to achieve a flexible, light-weight and compact wireless ECG recording system prototyped on a parylene printed circuit membrane.

The wearable MEA membranes provide electrophysiological insights into the aberrant conduction phenotypes of regenerating tissues, otherwise difficult with the

micro-needle approach. The integration-enabled design paves the way for long-term water-proof electrical signal acquisition via wireless technology. As such, the polymer-based multi-channel MEA membranes hold promise for translational medicine, from assessing ECG in cardiac repair to monitoring electroencephalography (EEG) in seizure or brain injury.

References

- [1] I. Streitner, M. Goldhofer, S. Cho, H. Thielecke, R. Kinscherf, F. Streitner, *et al.*, "Electric impedance spectroscopy of human atherosclerotic lesions," *Atherosclerosis*, vol. 206, pp. 464-468, 2009.
- [2] T. Süselbeck, H. Thielecke, J. Köchlin, S. Cho, I. Weinschenk, J. Metz, *et al.*, "Intravascular electric impedance spectroscopy of atherosclerotic lesions using a new impedance catheter system," *Basic Research in Cardiology*, vol. 100, pp. 446-452, 2005/09/01 2005.